Numerical Investigation of the Unsteady Aerodynamics of

Blade Tip Leakage Flow Inside Gas Turbine Engines

Patricia Phutthavong

A Thesis

in

The Department

of

Mechanical and Industrial Engineering

Presented in Partial Fulfillment of the Requirements

for the Degree of Master of Applied Science (Mechanical Engineering) at

Concordia University

Montreal, Quebec, Canada

August 2006

Canada

ABSTRACT

Numerical Investigation of the Unsteady Aerodynamics of Blade Tip Leakage Flow Inside Gas Turbine Engines

Patricia Phutthavong

In today's modern gas turbine engines, the region between the rotor and the stationary shroud has the most extreme fluid-thermal conditions in the entire turbine, and is characterized by a periodically unsteady three-dimensional flow field. Due to the pressure difference across the blade tip, leakage flow enters the gap region from the pressure side and exits from the suction side. Tip leakage flow consists of hot mainstream gas and is highly undesirable since it does not turn, and so does not produce any work. Also, high heat transfer rates in the tip gap region occur as a result of leakage flow due to the formation of very thin boundary layers, which may lead to over-heating of the stationary shrouds. The purpose of the present work is to conduct an unsteady study of the tip leakage flow adjacent to the shroud in real gas turbine engines using an in-house industrial computational fluid dynamics (CFD) code. A turbine stage consisting of the nozzle guide vane (NGV) and rotor was modeled. The effect of tip clearance height, inlet turbulence intensity, inlet total temperature, and rotor angular velocity on the tip leakage aerodynamics will be investigated. To the best of the author's knowledge, time-accurate simulations have not been performed in order to study the effects of flow parameters on tip leakage flow aerodynamics. In addition, the trials of using a commercial CFD

package to obtain heat transfer calculations on the shroud will be presented. It was found that the size of the separation bubble on the pressure side of the blade tip is dependent on the inlet total temperature and rotor angular velocity. Also, when the relative height of the separation bubble is large, a small re-circulation zone was found at the suction side of the blade tip. In all cases, flow re-circulation was found near the trailing edge and was due to the combined effect of the shroud relative motion with the secondary cross-flow from the adjacent blade passage.

Acknowledgements

This work is dedicated to François,

who has been by side from the very beginning of this journey.

Table of Contents

List of Figures

List of Tables

Nomenclature

b	Blade span, *(m)*
C_x	Blade axial chord, *(m)*
c	Speed of sound, $c = \sqrt{\gamma RT}$, $\left(\dfrac{m}{s}\right)$
c_p	Specific heat at constant pressure, $\left(\dfrac{J}{kg \cdot K}\right)$
c_v	Specific heat at constant volume, $\left(\dfrac{J}{kg \cdot K}\right)$
D_ω	Cross diffusion term, $\left(\dfrac{kg}{m^3 \cdot s^2}\right)$
E	Total Energy, $E = H + \dfrac{V^2}{2} - \dfrac{p}{\rho}$, *(J)*
G_k	Production of turbulence energy, $\left(\dfrac{kg}{m \cdot s^3}\right)$
G_ω	Production of specific dissipation rate, $\left(\dfrac{kg}{m^3 \cdot s^2}\right)$
H	Enthalpy, $\left(\dfrac{J}{kg}\right)$
h	Tip clearance height, *(m)*
I	Turbulence Intensity, $I = u'/U_\infty$
k	Turbulent kinetic energy, $\left(\dfrac{m^2}{s^2}\right)$

k_f	Thermal conductivity, $\left(\dfrac{W}{m \cdot K}\right)$
k_{eff}	Effective conductivity, $\left(\dfrac{W}{m \cdot K}\right)$
M	Mach number, $M = \dfrac{V}{c}$
M_t	Turbulent Mach number, $M_t = \sqrt{\dfrac{k}{c^2}}$
p	Pressure, (Pa)
Pr_t	Turbulent Prandtl number
PS	Pressure side of the airfoil
q	Heat flux, $\left(\dfrac{W}{m^2}\right)$
R	Gas constant, $\left(\dfrac{N \cdot m}{kg \cdot K}\right)$
r	Radial coordinate, (m)
$\vec{r}$	Position vector, (m)
S	Modulus of the mean rate-of-strain tensor, $S = \sqrt{2S_{ij}S_{ij}}$, $\left(\dfrac{1}{s}\right)$
S_{ij}	Strain rate tensor, $\left(\dfrac{1}{s}\right)$
SS	Suction side of the airfoil
T	Temperature, (K)
t	Time, (s)
t^*	Non-dimensional time, $t^* = t/\Theta$

Δt Time step, *(s)*

u_i Ensemble-averaged velocity component, $\left(\dfrac{m}{s}\right)$

$u_i^{'}$ Fluctuation of velocity from the ensemble-averaged value, $\left(\dfrac{m}{s}\right)$

u_τ Wall friction velocity, $\left(\dfrac{m}{s}\right)$

U, V Velocity, $\left(\dfrac{m}{s}\right)$

$\bar{v}$ Velocity vector $\langle u, v, w \rangle$, $\left(\dfrac{m}{s}\right)$

W Mass flow rate, $\left(\dfrac{kg}{s}\right)$

x Axial coordinate, *(m)*

Y_k Dissipation of turbulent kinetic energy, $\left(\dfrac{kg}{m \cdot s^3}\right)$

Y_ω Dissipation of specific dissipation rate, $\left(\dfrac{kg}{m^3 \cdot s^2}\right)$

Y_M Dilatation dissipation, $\left(\dfrac{kg}{m \cdot s^3}\right)$

y Circumferential coordinate, *(m)*

Greek symbols

Θ Airfoil passing period, *(s)*

θ Angular pitch, *(radians)*

ε	Turbulent dissipation rate, $\left(\dfrac{m^2}{s^3}\right)$
Γ_k	Effective diffusivity of turbulent kinetic energy, $\left(\dfrac{kg}{m \cdot s}\right)$
Γ_ω	Effective diffusivity of specific dissipation rate, $\left(\dfrac{kg}{m \cdot s}\right)$
γ	Ratio of specific heats, $\gamma = c_p / c_v$
ν	Kinematic viscosity, $\left(\dfrac{m^2}{s}\right)$
μ	Dynamic viscosity, $\left(\dfrac{kg}{m \cdot s}\right)$
μ_{eff}	Effective viscosity, $\left(\dfrac{m^2}{s}\right)$
μ_t	Turbulent viscosity, $\left(\dfrac{m^2}{s}\right)$
ρ	Density, $\left(\dfrac{kg}{m^3}\right)$
σ_k	Turbulent Prandtl number for turbulent kinetic energy
σ_ε	Turbulent Prandtl number for turbulent dissipation rate
$\overline{\overline{\tau}}, \tau_{ij}$	Stress tensor, *(Pa)*
τ	Shear stress, *(Pa)*
Ω	Rotor angular velocity, *(rpm)*
ω	Specific dissipation rate, $\left(\dfrac{1}{s}\right)$

Subscripts

∞	freestream conditions
aw	adiabatic wall
c	core flow
o	stagnation properties
rel	relative
w	wall

Chapter 1

Introduction

In modern gas turbine engines, tip clearances between rotating turbine blades and stationary shrouds are very small, and in some cases are even smaller than 1 mm in height. The shroud over a turbine rotor is exposed to intense heat conditions, and it is important to be able to predict heat transfer coefficients in the tip gap region in order to optimize the amount of shroud cooling so that the performance does not suffer too great a loss. A schematic of a typical turbine in an aero engine and the location of the shroud are shown in Figure 1.1. The rapid development of high-temperature turbines has vastly surpassed the fundamental research of the thermal field in the tip clearance region between the shroud and the rotor. The transitional region between the rotor and the stationary shroud, in the first turbine stage, has the most extreme fluid-thermal conditions in the entire turbine, and is characterized by a periodically unsteady three-dimensional flow field. Therefore, it is very difficult to accurately represent the flow phenomena analytically.

The heat transfer in the blade tip gap region of modern gas turbine engines is driven by the extremely complex tip gap flow field. Tip leakage flow consists of hot mainstream gas and is highly undesirable since it does not rotate, and so does not produce any work. Also, high heat transfer rates in the tip gap region occur as a result of leakage flow due to the formation of very thin boundary layers. In a gas turbine engine, the shroud is
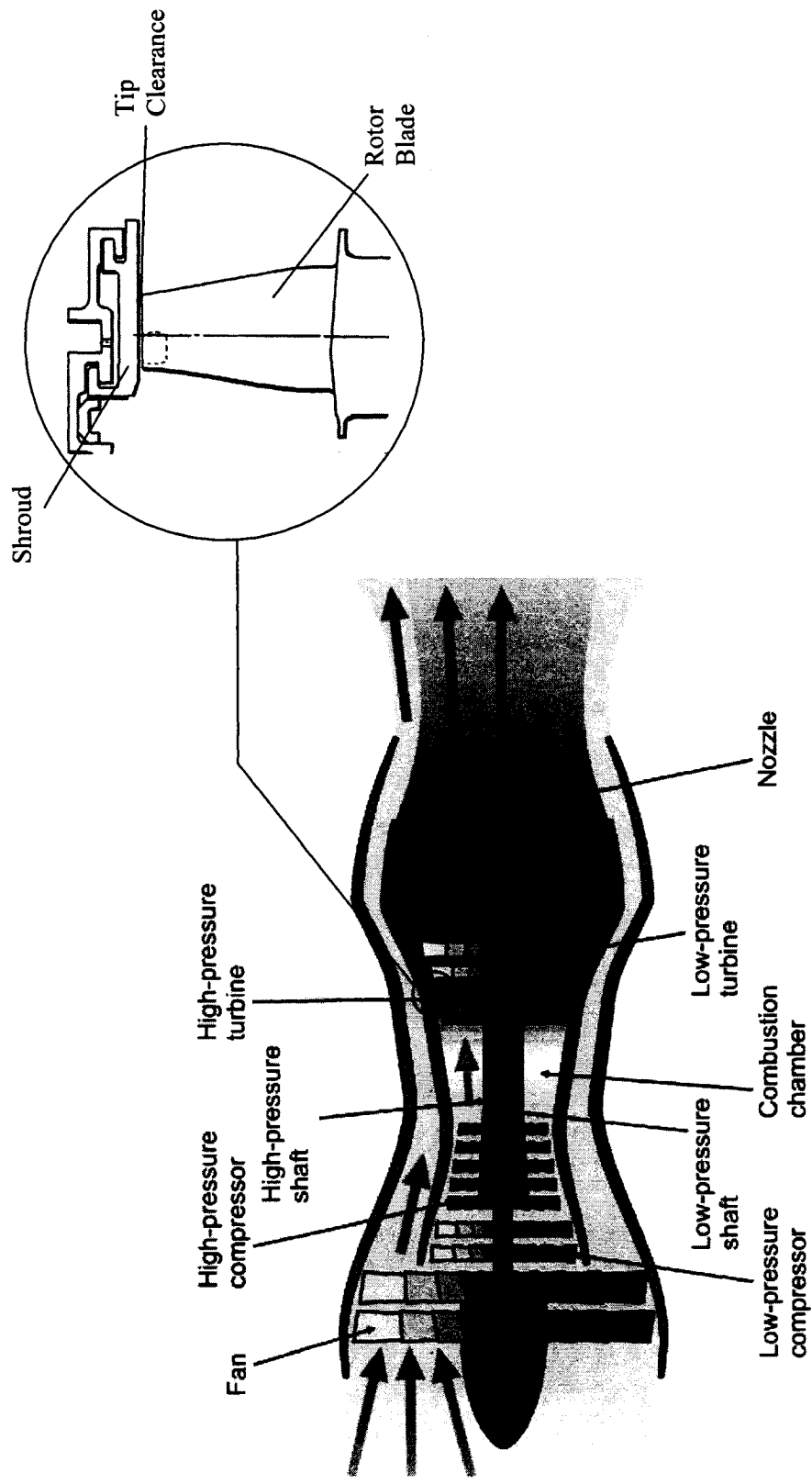
Figure 1.1 Two-stage turbine inside a typical gas turbine engine (Wikipedia, 2006) with an up-close view of the shroud segment and rotor blade in turbine rotor (Moustapha, 2005).

stationary while the rotor rotates beneath it, as seen from the absolute reference frame. Therefore, in the relative reference frame of the rotor, the shroud appears to be traveling above from suction side to pressure, as shown in Figure 1.2. Due to the pressure difference across the blade tip, leakage flow enters the gap region from the pressure side and exits from the suction side. The shroud's relative motion is opposite to the direction of the tip leakage flow, and so there exists a stagnation line (line A1-A2) where the flow velocity is zero in the tip gap region. Also, Figure 1.2 shows that a separation bubble, represented by b1, develops on the pressure side of the blade tip as the leakage flow enters the tip gap region. The leakage flow leaves the suction side of the blade tip in the form of a vortex as it comes in contact with cross flow. The subsequent mixing of the leakage flow with the main flow causes the momentum of main passage flow to decrease, further decreasing the efficiency of the engine.

Unfortunately, it is not realistic to completely eliminate the gap between the rotor and shroud, since it is required in order to accommodate the centrifugal growth and thermal expansion of the blade within this gap. In other words, the tip clearance gap may significantly vary in size due to the different thermal expansion rates of the shroud and blade, which may occur during take-off or cruise. In some instances, the shroud may actually cool faster than the blade, causing rubbing to occur. Using recessed tips have allowed tip clearance gaps to be quite small, while reducing the possibility of severe damage due to rubbing.

The best data that can be used for designing turbines is obtained from field experience
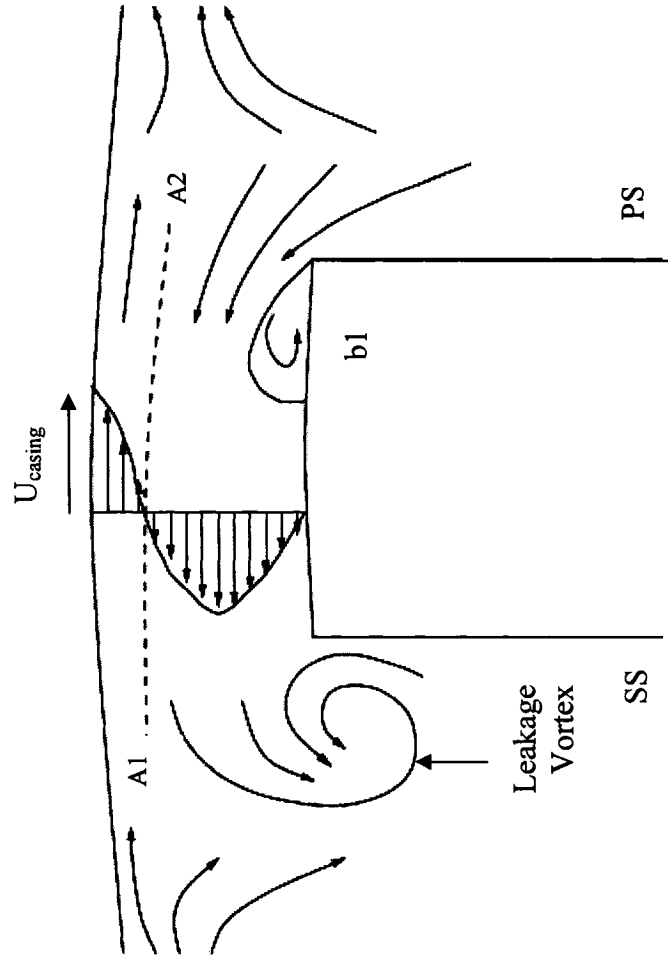
Figure 1.2 Velocity profile in the tip gap region as seen from the rotating reference frame (Dey, 2001).

4

under different operating conditions. Unfortunately, experimental data in the tip clearance region is very expensive, since the tip gap region is so small rendering it very difficult to obtain accurate measurements in the gap. Stationary cascades allow researchers to obtain detailed heat transfer data in this highly three-dimensional flow area between the rotor and shroud with relative ease. However, caution should be taken when applying these results to rotating turbines. Thus, the best alternative to field data is data from rotating turbine rigs, though it is important to note that these rigs operate with no combustion, which is somewhat unrealistic.

Representative analytical equations for such complex flow systems often have to be solved using numerical techniques. Computers have become an invaluable tool in engineering design, especially in the field of fluid mechanics and heat transfer. As a result, computational fluid dynamics (CFD) is becoming more attractive in the research community since it is much more cost-effective. CFD simulations simultaneously solve the continuity, Navier-Stokes, and energy equations for both two- and three-dimensional systems with complex geometries and boundary conditions, which would otherwise take years to solve without the aid of today's modern computers. As a result, there has been a drastic increase in interest in the field of CFD especially in the aerospace industry, more particularly with regards to the turbine shroud.

The purpose of the present study was to conduct an unsteady study of the tip leakage flow adjacent to the shroud in gas turbine engines using computational fluid dynamics (CFD) under typical engine conditions. A turbine stage consisting of the nozzle guide vane

5

(NGV) and rotor was modeled, whereby the rotation of the rotor was taken into account. Sectors of the NGV and rotor were considered, whereby the lowest number of vanes and blades were modeled, while ensuring that the periodic angles of both domains were identical. Two separate computational domains, one for the NGV and one for the rotor, were generated which were later merged into the CFD solver. Here, the nozzle guide vane was considered to be the stationary in the absolute reference frame, while the rotor domain was set as a moving mesh with an angular velocity. It is important to note that although the shroud exists in the rotor domain, it was given an angular velocity of zero in the absolute reference frame.

The present work will be presented in the following manner. First, a chronological review of the studies focusing on tip gap flow and heat transfer for both stationary cascades and rotating blades will be presented in Chapter 2. Next, all governing equations, boundary conditions, and method of solution for the CFD modeling will be given in Chapter 3. In Chapter 4, time-averaged results will be presented in order to show grid independence tests and to prove that the industrial in-house code used in the present study is reliable and capable of predicting tip clearance data from an experimental study. Chapter 5 will show the time-accurate results obtained from the unsteady parametric study of tip leakage flow in an actual gas turbine stage. Finally, conclusions from the present study will be given in Chapter 6, as well as the challenges and future directions that are required to study heat transfer mechanisms of the shroud in gas turbine stages.

Chapter 2

Literature Review

In the following chapter, a chronological review of the studies on the blade tip flow field and corresponding heat transfer on the shroud will be presented. To date, the flow field in the tip gap region has received much more attention than the heat transfer in this region. The first section summarizes studies which considered the rotation of the blades, while the second section covers studies involving stationary cascades where the blades remain stationary. While most studies focus on tip gap flow patterns, some more recent studies have investigated shroud heat transfer in particular. A summary of the literature review as well as the motivation for the present study will be given in the final section of this chapter.

2.1 Rotating Blades

Allen and Kofskey (1955) performed one of the earliest flow visualization studies of the tip flow field in a low-speed rotating turbine test rig using smoke. Cross-channel flow was found on the shroud moving towards the suction surface of the blade, and the formation of the tip leakage vortex was observed when the tip leakage flow moving from the pressure side to suction side of the blade tip encountered the cross-channel flow in the adjacent passage. When the two oppositely moving streams meet, they both turn away from the shroud and begin rotating in the counterclockwise direction forming the leakage

vortex. In addition, they determined that there was a range of rotor speeds where no vortices were observed, which they called a transition region. It was found that the rotor speed at which transition occurs increases with increasing mainstream flow and tip clearance. For turbine engines typically above this transition region, and at these higher speeds, an additional vortex called the scraping vortex was observed, which rotated in the clockwise direction. Its formation was attributed to the movement of the pressure field in the tip gap region, which may cause the shroud boundary layer to roll up and turn away from the casing.

A two-part study of rotor tip leakage was conducted by Booth et al. (1982) and Wadia and Booth (1982) in order to develop an appropriate numerical model for predicting leakage flow patterns in the tip gap region. In Part I, Booth et al. conducted experiments on water flow rigs with stationary blades, and the results were used to develop a simple two-dimensional tip leakage model where the rotor tip is treated as an orifice and by only considering the flow normal to the camberline of the blade. The model considered that the flow was incompressible and laminar, and that the streamwise momentum is preserved across the gap. In the second part, Wadia and Booth used the model to obtain flow patterns over moving blades with and without tip injection. The size of the mesh was 61×41 nodes and minimum values of Δx and Δy were 0.5 and 0.1, respectively. Radial potential flow solutions were applied at the inlet and outlet surfaces. They found that relative motion of the shroud causes a reduction in leakage flow.

Dunn et al. (1984) studied the heat flux distribution of various components in the full-

stage rotating turbine of the Garrett TFE 731-2 engine including the nozzle guide vane, rotor, and shroud. Three different ratios of wall temperature to gas total temperature were studied. Data reduction of the surface temperature distributions was used to obtain heat transfer rates. Numerical predictions from two different numerical codes, Wright-Patterson AFB Turbine Design System (TDS) code and a modified STAN5 code, were obtained for the nozzle guide vane and rotor, but not for the shroud. The Stanton numbers on the shroud, based on inlet conditions, were determined, where the total gas enthalpy was assumed constant. This postulation is erroneous however since work extraction by the rotor will cause this value to decrease. The Stanton numbers were shown to decrease in the axial direction for all temperature ratios. The authors noted that the trend of the Stanton number distribution on the shroud would differ significantly if the local values of the total gas enthalpy were used instead. Local values of the total enthalpy were not available in this study.

Guenette et al. (1985) focused specifically on shroud heat transfer by obtaining time resolved measurements of the heat transfer rate and the static pressure on the shroud of a high pressure turbine rotor in the MIT Blowdown Turbine Facility. All non-dimensional parameters were identical to actual values used in full-scale gas turbines. The time-resolved measurements were taken at three different rotor speeds and two different Reynolds numbers. It was found that the Reynolds number did not affect the flow field nor the axial heat flux distributions. A sudden decrease in pressure was observed along the pressure side of the blade, where the overall pressure ratio from the pressure side of the blade to the suction side was more than a factor of two. The heat flux on the shroud

above the blade tip was five to six times greater than that in the midpassage at the same chordwise location, and the maximum heat flux occurs where there was a large static pressure gradient. In the chordwise direction, the time-averaged heat flux decreased by a factor of four to five, and this was attributed to the decrease in the total temperature due to enthalpy extraction by the rotor and the blade thickness distribution.

Metzger et al. (1991) presented a simple model for estimating tip flow and heat transfer to the shroud. The model may be used as long as the clearance gap size and clearance leakage flow can be appropriately estimated. The relative reference frame of the rotating turbine blade is used, thus the shroud is represented by a locus of points with a velocity equal to the blade tip velocity (relative to the shroud) due to no-slip conditions. The leakage flow through the gap appears to move at a velocity opposite to the shroud velocity. As a result, the flow at the blade tip is represented as a stationary channel entrance flow, and the blade tip heat transfer can be subsequently obtained once the magnitude of the leakage flow is known. When considering the heat transfer to the stationary shroud, the resultant velocity at a given point on the shroud is the result of the clearance gap velocity and blade passage velocity. In this study, Metzger et al. (1991) predicted the amount of leakage flow across the blade tip through the use of a Navier-Stokes numerical code. The results predicted by the model were compared to experimental data obtained from a Garrett 731-2 full-stage rotating turbine. The heat transfer data on the shroud was in good agreement with the predicted results from the model.

Kumada et al. (1994) experimentally obtained the local heat transfer coefficient on the shroud under uniform heat flux boundary conditions. The effect of the inlet flow angle, rotor velocity, and tip clearance on the heat transfer coefficient was investigated. As the rotor velocity increased, the heat transfer coefficient increased for all tip clearances. In the region just opposite from the rotor, regardless of inlet flow angle, rotor velocity, and tip clearance, the heat transfer coefficient distribution in the axial direction was shown to fluctuate, and was attributed to the development of the boundary layer combined with the acceleration of the flow near the wall. The maximum heat transfer coefficient on the shroud occurred above the downstream corner of the rotor in the axial direction.

Yamamoto et al. (1994) obtained time-averaged and time-dependent pressure measurements to quantify losses due to tip clearance flows. Data was obtained over a first-stage rotor and second-stage stator in a low-speed axial flow turbine. They found that the rotor-stator interaction is very significant such that the losses due to leakage flow are very unsteady and random. Also, there is a large pressure drop on the blade pressure surface in the region where leakage flow enters the tip gap region. At low rotor speeds with high loading on the blade, the pressure difference across the blade's pressure side and suction side increases, thus increasing the mass flow rate of the leakage flow. At high rotor speeds with low loading, leakage flow was observed which originated from the suction side of the blade due to the increase in the pressure gradient normal to the blade suction surface.

Nikolos et al. (1995) developed a theoretical model for predicting the mass flow rate

through the tip gap region, which takes into account the relative motion of the shroud. The model is an extension of the author's previous model for stationary blades. The strength of leakage vortex was found to be dependant on the mass flow rate inside the tip gap region. It was found that the motion of the shroud causes a decrease in the strength of the leakage vortex, and also affects the location of the vortex by moving the vortex center in the direction of its motion. The predicted results were in good agreement with existing experimental data.

Ameri and Steinthorsson (1996) used a Reynolds Averaged Navier-Stokes (RANS) computer code called TRAF3D in order to calculate the heat transfer coefficient on a simulated blade tip and shroud. C-grids, O-grids, as well as H-grids were used in their study. The C-grids wrapped around the turbine blade; O-grids were utilized for the clearance gap between the tip and shroud; and H-grids were used in the upstream region of the vane. Grid dimensions were listed as 192 x 48 x 64 for the C-grids, and 128 x 16 x 20/32/40 for the O-grids, in the circumferential, transverse, and spanwise directions, respectively. The latter dimensions for the O-grid represent the three different spanwise dimensions of the tip clearance gap tested in the study. They compared their results to the experimental work of Dunn et al. (1984). They found that the predicted heat transfer coefficient on the shroud was much lower than that given by experimental results. In addition, the effect of rotation rate of the blade on shroud heat transfer was observed to be negligible since shroud heat transfer depends on absolute flow velocity, which was a constant in the present study. The average heat transfer coefficient decreases with increasing axial chord, while the local heat transfer coefficient distribution revealed that

the heat transfer coefficient was quite large in the mid-chord region on the pressure side. This region of large heat transfer rate coincides with the region of large favorable pressure gradients. In a later study, Ameri et al. (1998) used the same computer code to simulate the tip flow and heat transfer on the GE-E^3 turbine blade with and without a squealer tip. The results for the heat transfer coefficient on the shroud obtained showed similar trends as described above.

Ristic et al. (1998) used a three-dimensional laser Doppler velocimetry system to measure the flow field at the exit plane of a rotor in an axial flow turbine facility equipped with nozzle guide vanes and rotor blades. The flow near the casing was the most complex with interaction between the passage vortex and tip leakage vortex. As a result, the passage vortex restricts the leakage vortex near the suction surface. Near the pressure side of the blade tip, strong radially outward flow was observed, while at the suction side, the flow was directed radially inward due to the presence of the tip leakage vortex and passage vortex.

Tallman and Lakshminarayana (2001b) conducted a numerical study of the effect of the shroud's relative motion on the tip leakage flow in a linear cascade. The same CFD code used in their previous study (2001a) was applied here. They found that the presence of the moving wall's shear layer greatly affects the leakage flow in the tip gap region. The shear layer causes the leakage flow to travel more in the axial direction, and also reduces the leakage flow inside the gap. Also, it obstructs the leakage flow, especially near the blade leading edge, and forces the leakage to leave the gap further downstream. In

addition, the leakage vortex was found to be one third the size of that in fixed wall cases, since much of the leakage flow traveled around and underneath the vortex causing significant secondary flow in the spanwise direction. The roll-up of the leakage vortex occurred further downstream than in the fixed wall cases, and it consisted entirely of leakage flow. Losses in the moving wall cases were attributed equally to the additional secondary flow losses as well as leakage flow losses.

Xiao et al. (2001) captured the pressure field, velocity fields, turbulence fields, as well as the losses in the tip gap region of an axial turbine rotor using laser Doppler velocimetry. They observed that the tip leakage vortex begins to develop at the midchord of the blade, and continues to grow as it moves downstream with diffusion effects dominating the vortex development at about 0.9 of the axial chord. Beyond 0.9 of the axial chord the passage vortex and the leakage vortex merge together generating significant losses. The flow was observed to be inviscid at about 0.1 of the span from the blade tip where only the passage vortex is present. Also, the core of the tip leakage vortex moves radially inward with an inclination of 21 degrees from the blade tip surface, which is significantly higher than that observed in stationary cascades. This was attributed to the relative motion of the shroud in the rotating reference frame. In addition, the shroud's boundary layer as well as its relative motion opposes the tip leakage flow, forming a low-pressure region which may increase the flow velocity of the leakage flow. This was not observed in stationary cascade studies.

McCarter et al. (2001) provides physical explanation for the data obtained by Xiao et al.

(2001). They observed that the leakage flow leaves the gap after an axial chord position of about 0.7. Beyond an axial position of about 0.8 axial chord, the leakage flow strengthens and moves further into the passage in both the tangential and radial directions. The interaction of the leakage flow with the main passage flow forms the tip leakage vortex, and the shroud's relative motion confines it to the region near the suction side of the blade tip. As the leakage vortex moves downstream beyond 0.9 axial chord, the vorticity and turbulence increases significantly, and begins interacting with the passage vortex. Overall, the tip leakage flow dominates the losses in the tip region, where the shear stress from the tip vortex is much higher than those from the passage vortex and blade boundary layer.

Chana and Jones (2003) conducted an experimental study of the heat flux on the turbine tip and shroud on a full-sized rotating turbine high pressure facility. The authors ensured that the generated radial and circumferential non-dimensional temperature profiles matched those of an actual gas turbine engine. Three different inlet temperature profiles were tested. The contour plots of the Nusselt number on the shroud for the three different inlet temperature profiles were generated. For the uniform inlet temperature profile case, three different regions of high heat transfer were observed, two of which were associated with the trajectory of the predicted wake path from the vane. The existence of the third region of high heat transfer, which appeared at the halfway point of the vane pitch, was explained by the presence of passage shocks originating from the vane. Nusselt number contour plots for the other two inlet temperature profiles did not reveal three distinct high heat transfer regions as described above for the uniform inlet temperature case. The

15

variation of the circumferentially averaged Nusselt number with axial position on the shroud showed that the Nusselt number increased rapidly to a peak value near the leading edge, after which it gradually decreased. Time-resolved heat transfer measurements showed that the heat transfer increased rapidly as the pressure side approached, and subsequently dropped as the tip passed over the shroud attaining a minimum as the suction side approached. The heat transfer increased once again as the pressure side of the following blade passed over the shroud.

Polanka et al. (2003a) experimentally studied the pressure and heat transfer in the turbine tip-gap region. Measurements for the pressure and heat transfer were obtained simultaneously from a full-scale, single-stage rotating high pressure turbine. The effects of Reynolds number, inlet temperature, and turbine pressure ratio on the pressure and heat transfer loading of a single turbine blade were investigated in Polanka et al. (2003a), and the results were compared to existing two-dimensional correlations. The test facility used by Polanka et al. (2003a) is equipped with a full-scale turbine rotor and is able to operate for several seconds under actual engine conditions. Nitrogen gas was used with a specific heat ratio $\gamma = 1.4$ and Prandtl number, Pr, equal to 0.71, which is nearly identical to that of high temperature air. The measurements were obtained in a time span between 740 and 980 ms after the supply tank valve was opened, since measurements were relatively steady during this interval. The effects of the gas to metal temperature ratio, exit Reynolds number, pressure ratio, and inlet total temperature profile (i.e., percentage of core mass flow rate) were studied. High heat transfer was observed in the blade tip/shroud region, with rates as high as that in the stagnation region of the airfoil of the

blade. The heat flux on the shroud was similar to that of the blade tip near the leading edge, while in the aft portion of the airfoil, it was significantly lower than that for the blade tip. High Nusselt numbers were also observed at low pressure ratios in the aft portion of the airfoil, and this was attributed to flow separation in this region. However, no significant difference for the Nusselt number could be detected near the leading edge of the airfoil when the pressure ratio was varied. Also, the Nusselt number on the shroud increased with increasing Reynolds number. In general, as the gas to metal temperature ratio decreases, the Nusselt number increases, while no significant change was observed when the inlet temperature profile was varied. It was noted, however, that the shroud heat flux data in the downstream region is erroneous since the Nusselt numbers were obtained using measured heat fluxes based on a driving temperature equal to the inlet relative total temperature. In reality, this driving temperature should be the local relative temperature, since the inlet temperature will change due to the work performed in the rotor passage. Unfortunately, this local temperature was experimentally unattainable, which renders it difficult to comprehend the true heat transfer phenomena in this region.

Polanka et al. (2003b) conducted a numerical study in order to predict the results obtained in their experimental study reported in Polanka et al. (2003a), focusing strictly on the baseline experimental conditions only. The 3-D, Reynolds Averaged Navier-Stokes (RANS) code used was able to capture the extremely complex flow field and associated heat transfer behavior, which could not be attained experimentally. OH meshes were used, where the O-mesh grid count was 113 x 33 x 57, while the H-mesh count was 169/185 x 33 x 57 in the axial, radial, and circumferential directions,

respectively. Fifteen grid points were located in the boundary layer of each vane surface, while 30 grid points resided in the near wake region. The code used finite volume method and was accurate up to the second order for space and time. Forty-four vanes and fifty-eight blades were modeled in order to simulate the experimental facility. Isothermal walls were used as boundary conditions and numerical closure was attained by use of the high Reynolds number k-ω turbulence model. Predicted results for the heat flux on the shroud exceeded the experimental data by a factor of two. Errors in experimental measurements were attributed to this discrepancy. The predicted heat flux was greatest when the pressure side of the blade tip was directly over the shroud due to the presence of tip clearance flow originating from the pressure side of the blade tip. As a result, the boundary layer at the shroud becomes thinner, thus the shear stress and heat flux become very high. The effect of tip clearance on shroud heat transfer was significant near the leading edge only. The streamlines of the tip clearance flow over the blade tip itself moved from the pressure side to the suction side, when the rotor reference frame was considered. Thus, when the tip clearance gap increased, more flow was induced, and as a result, maximum heat transfer occurred in this region, where the maximum value depended on the amount of tip gap flow or tip clearance such that larger tip clearances yielded higher heat fluxes on the shroud.

Haldeman and Dunn (2004) obtained heat flux measurements on the shroud of a rotating turbine rig at two different Reynolds numbers based on vane inlet conditions: 4.26×10^6 and 8.32×10^6. Flat-tip blades were used in the experiments. The time-averaged heat flux measurements showed that there were higher heat fluxes on the shroud at higher

Reynolds numbers. Also, the shroud heat flux was lower than that on the blade tip, and was observed to decrease rapidly after approximately 60% of the blade axial chord. However, when the heat transfer data was non-dimensionalized to obtain the Stanton number, the opposite trend was observed, such that lower Stanton numbers corresponded to high Reynolds numbers. The authors stated that this was due to the difficulty in knowing how to non-dimensionalize the shroud heat flux data.

Thorpe et al. (2004) obtained time-mean and time-resolved results for the heat transfer on the shroud of a short duration turbine facility. In generating the time-mean results, they found that the heat transfer decreased by a factor or 6 in the axial direction due the decrease in the total temperature through the blade row. However, the heat transfer did not vary significantly in the circumferential direction indicating that the stator did not have a strong effect on the shroud boundary layer properties. The time-resolved results revealed that the heat transfer to the shroud is highly time-dependent, corresponding to blade passing events. At any given point on the casing, the heat transfer to the shroud was found to originate from two sources: the leakage flow over the blade tip as well as the blade passage flow. In addition, it was found that the absolute total temperature in the tip gap region increased above that at the turbine inlet due to a work distribution throughout the rotor.

Hassanvand et al. (2004) conducted a three-dimensional unsteady simulation of a high pressure steam turbine stage consisting of 48 stator blades and 106 rotor blades, using the commercial Navier-Stokes solver called NUMECA. Their study focused on the viscous

dissipation inside the tip gap region. The simulation was performed using a reduced computational domain consisting of one stator and two rotor blade passages. The grid was generated in seven blocks. The stator was modeled as one block consisting of $129 \times 33 \times 65$ nodes in the streamwise, pitchwise, and spanwise directions respectively, while two blocks were used for the two blades with each having $145 \times 49 \times 65$ nodes. The tip gap region was modeled in two blocks with the internal block measuring $65 \times 9 \times 9$ nodes, while the external block measured $145 \times 9 \times 9$ nodes. Water vapor was considered as the working fluid, and the Baldwin-Lomax turbulence model was used in their calculations. It was found that the high viscous regions were located near the shroud as well as the suction surface of the blades. The mass-averaged viscous dissipation near the shroud was observed to be more than one order of magnitude greater than that for the blade tip. Near the shroud, the highest amounts of viscous dissipation were located near the suction side of the blade tip between 0.25 and 0.75 axial chord, while the lowest amount of viscous dissipation resided near the leading and trailing edges, as well as in the main blade passage. In addition, a pair of source and sink points were observed near the shroud located near the pressure and suction sides, respectively. Thus, it was concluded that the tip leakage flow could be represented by a simple model using a pair of source and sink points.

Lampart et al. (2004) numerically investigated the interactions between tip leakage flow and the main rotor flow in a two-stage turbine. A CFD RANS-based code called FlowER was used for the calculations, and the SST k-ω model was chosen to model the

turbulence. The simulation was steady, and utilized the mixing plane approach between the stationary and rotating domains. The stator measured $86 \times 76 \times 72$ nodes in the axial, spanwise, and pitchwise directions respectively, while the rotor consisted of $96 \times 76 \times 72$ nodes. Sink boundary conditions were applied downstream of the stator airfoils, while source boundary conditions were applied in locations downstream of all rotor airfoils. In the first stage rotor, it was observed that the tip leakage flow causes a reduction in the mean axial velocity, which may cause a local increase in the incidence angle. Thus, the size of the separation zone increases as the leakage flow rate rises, thus increasing the separation losses. As a result, the second stage stator and rotor are also affected due to the increased re-circulating originating from the first stage rotor.

Camci et al. (2005) obtained leakage flow mechanisms in the tip gap region using the same rotating turbine research facility as Ristic et al. (1998). Blades with squealer rims on the suction side only (partial squealers) were used, as well as blades with both a suction side squealer and a pressure side squealer of varying length (squealer channel). Results showed that partial squealer configuration was best at reducing tip leakage flow. The leakage mechanism for the partial squealer is as follows as seen from the relative reference frame. When the flow enters the gap region from the pressure side, flow separation occurs. The flow then encounters the suction side rim and separation occurs again as the corner of the blade tip and squealer as the flow moves radially upwards in order to negotiate the squealer rim. However, due the motion of the wall, moving from the suction side to the pressure side, large turbulent shear stress is induced causing some of the radially moving flow to roll into a vortex, while the rest escapes over the squealer

21

tip. Subsequently, the leakage flow encounters the main passage causing it to roll up to form a tip leakage vortex. Camci et al. also reported the significant differences between blade leakage flow data from stationary cascades and rotating rigs. The relative motion of the shroud tends to confine the tip leakage vortex near the suction side of the blade, while stationary cascades show that the secondary flow moves away from the shroud and away from the suction surface.

Green et al. (2005) conducted unsteady simulations of their own experimental work on a rotating turbine rig. Pressure measurements were obtained on the platform, blade tip, and shroud of the rotor, while the CFD code, MSU-TURBO, was used to predict the pressure distributions in the turbine rig. Their results showed that the variations of the pressure in the tip gap region with time were due to the passing of the upstream vane shock through the rotor passage. As the shock moves across the leading edge from the suction to the pressure surface of the blade, the blade tip pressure increases to its maximum value, and afterwards drops as the shock departs from the leading edge. Also, there is some effect of the vane wakes on the flow field in the tip gap region, but is small compared to that from the vane shock. For the stationary shroud, peaks in the pressure distribution of the shroud were attributed to the passing of the pressure side of the blade over the shroud at any instant.

Palafox et al. (2005) obtained two-dimensional PIV flow maps of tip leakage on a very large scale linear cascade with a blade chords measuring 1 meter. The relative motion of the casing was emulated by using a motor driven moving belt system, and it was found

that the separation bubble was half the height than its stationary wall counterpart. This was attributed to the influence of the shroud's movement causing the tip leakage vortex to shift towards the gap exit. Also, the moving shroud causes the tip leakage vortex to distort in shape, and also moves both the passage vortex and leakage vortex closer to the suction side. Finally, a third vortex called the scraping vortex was observed, which is generated by the tip leakage flow and the movement of the shroud.

Rhee and Cho (2005) investigated local heat and mass transfer on the blade tip and shroud of a low-speed rotating annular turbine cascade. A naphthalene sublimation technique was used to obtain time-averaged mass transfer coefficients on the blade tip and shroud. Both stationary and rotating blades cases were studied. The Sherwood number was used to obtain the associated heat transfer from the mass transfer measurements. The heat/mass transfer coefficients on the blade tip were found to be 1.5 to 1.7 times greater than those on the shroud due to flow reattachment on the blade tip. The time-averaged heat/mass transfer coefficients on the shroud were similar for both the stationary and rotating blades cases with the stationary cases showing levels in the coefficients that were slightly lower (less than 10%).

Although, results from studies that consider rotating blades are more realistic, obtaining data either experimentally or numerically can be complicated. In real gas turbine engines, flow speeds are typically transonic in high-pressure turbines, and gap sizes are typically usually on the order of millimeters. Thus, most experiments have used low-speed and/or large-scale test facilities in order to facilitate data acquisition. Numerical

23

simulations also become more difficult when the rotation of the rotor is taken into account since unsteady simulations are much more time consuming, requiring a huge amount of computational resources. Therefore, as an alternative, many researchers have conducted investigations of tip leakage flows on stationary blades with no relative motion of the shroud.

2.2 Stationary Blades

Today's general understanding of the tip gap flow field was proposed by Bindon (1989). The airfoils in the linear cascade were large-scale with chords measuring 152 mm, and measurements were obtained using a 1 mm diameter single-hole cylindrical probe. Bindon observed that a narrow separation bubble, or re-circulatory flow zone, develops along the pressure side of the blade tip, and that within the bubble a significant chordwise flow is formed due to a negative pressure gradient near the leading edge of the blade. Eventually, however, the pressure gradient inside the separation bubble becomes positive further downstream, which causes the chordwise flow to separate from the blade surface. The separated flow eventually accumulates and becomes entrained into the main leakage flow, forming a high loss vortex, which leaves the gap region over the latter half of the blade on the suction side.

Yaras et al. (1989) obtained flow field measurements in a linear cascade under idealized conditions whereby the flow was incompressible with low free-stream turbulence. Tip clearance sizes ranging from 5 mm to 7.9 mm were studied, and measurements were

obtained using a three-hole pressure probe. The pressure drop which drives the leakage flow through the gap was found to be equal to the undisturbed blade pressure differences. Also, the flow was observed to be already completely accelerated even before entering the tip gap region. Their observations were consistent with the assumptions used in elementary tip clearance flow models, and so a simple model was developed in order to represent the complex three-dimensional flow field in the tip gap region. The results from their model proved to be in good agreement with their experimental results.

Yamamoto (1989) conducted an experimental study in a low-speed linear cascade in which the three-dimensional flow in the tip gap region was captured using a micro five-hole pitot tube. It was determined that the tip leakage vortex is comprised mainly of leakage flow residing in the downstream portion of the gap region, which lead to the conclusion that the formation of the leakage vortex is independent of the incident angle of the flow. In addition, it was observed that there was some tip leakage flow entering the gap from the leading edge and passing over to the suction side of the blade. Also, the strength of the leakage vortex was found to increase with tip clearance size.

Moore et al. (1989) performed a two-dimensional simulation of flow and heat transfer in a turbine tip gap. Laminar flow calculations were performed using a steady-state code called the Moore Elliptic Flow Program in order to study the effect of Reynolds number on incompressible low Mach number flows. Here, only the blade tip and blade pressure side surface, and shroud were modeled, and the grid measured $31 \times 21 \times 2$ cells. Uniform pressure was applied at both the inlet and outlet of the domain. At low Reynolds

numbers, no flow separation was observed in the tip corner region and the flow becomes fully developed laminar flow inside the tip gap. At higher Reynolds numbers, turbulence was observed, and flow separation was found at the tip corner forming a vena contracta in the tip gap region. In addition, two-dimensional turbulent calculations were performed in order to study the heat transfer to blade tips, and their results agreed well with existing analytical models for blade tip heat transfer. Finally, a high Mach number simulation was conducted, which used a hydraulic analogy between free-surface liquid flow and two-dimensional compressible flow in order to obtain velocity profiles and shock patterns inside the tip gap region. An oblique shock wave was found extending from the inlet corner of the shroud, which then reflects on the blade tip.

Sjolander and Cao (1995) conducted an experimental investigation on a single large scale idealized tip gap. Surface oil visualization was used to obtain flow patterns in the test facility. It was found that the separated flow in the gap is comprised of a primary vortex as well as a secondary counter-rotating vortex. The secondary vortex forms beneath the primary vortex near the pressure corner of the blade tip. It was proposed that the presence of this secondary vortex accounts for the burnout of blades at their pressure corner due to the high convective coefficients that develop in that area. Results were compared with the simple tip leakage models for Heyes and Hodson (1993) and were found to be in good agreement.

Cho et al. (2001) obtained the mass transfer coefficient on the shroud of a linear cascade, which was then converted to a Nusselt number using a heat and mass transfer analogy

given by Eckert (1976). The shroud was coated with naphthalene, and then scanned by an automated surface measuring system. The tip clearance was varied between 0.66% and 2.85% of the blade chord length. High heat transfer on the shroud was found above the pressure side, which was attributed to the acceleration of the tip leakage flow through the gap. A strong leakage vortex was observed as the leakage flow exited the gap, which enhanced the heat transfer along its path. As the tip clearance increased, the amount of leakage flow increased, and so the affected region of high heat transfer increased.

Tallman and Lakshminarayana (2001a) numerically investigated the effect of tip clearance on the tip leakage flow of a linear cascade. The three dimensional Navier-Stokes code used applies the k-ε turbulence model, and y^+ values were maintained in the single digit range. Here, the outer casing wall was considered to be stationary. They found that the core of the tip leakage vortex is comprised entirely of flow that has passed through the tip gap region, and so is not caused by main flow and leakage flow interaction. Instead, it was proposed that the development of the tip leakage vortex is due to vorticity convection from the tip gap region and the adverse pressure gradient experienced by the leakage flow. However, at larger tip clearance leakage flow and passage flow mixing could be possible. In addition, vortex roll-up was observed at a position between 30% and 40% of the axial distance from the blade leading edge. Three secondary flows were also identified. The first is the gap entrainment secondary flow (GESF) directs the main passage flow towards the pressure side of the tip gap region. Once the GESF enters the tip gap region it becomes the tip leakage flow. The second is termed blockage secondary flow (BSF), which is the result of the blocking of the passage

27

flow near the suction side to be blocked by the leakage vortex. The third is the near-casing secondary flow (NCSF), which directs flow from the pressure side to the suction side of the passage and is attributed to the presence of the passage flow's boundary layer. For larger tip clearances, the tip leakage vortex was larger, and the mass flow rate through the gap is higher as well. Finally, GSEF and BSF were stronger at larger tip clearances, while NCSF was stronger at smaller tip clearances.

Yang et al. (2002a) numerically predicted the tip leakage flow and subsequent heat transfer over a flat-tip GE-E[3] High-Pressure Turbine rotor blade, and compared their blade tip heat transfer results to Azad et al. (2000) for a stationary linear cascade. It is important to note that Azad et al. (2000) did not provide any experimental shroud heat transfer data. The commercial software FLUENT was used as the CFD solver, and the flow field was modeled with an unstructured grid with more than 800 000 nodes. Periodic boundary conditions were applied in the circumferential direction. The blade tip heat flux data for a 1.5% blade span tip gap and a turbulence intensity of 6.1% was used to determine the performance of three different turbulence models: the standard high Reynolds k-ε model, the renormalization group (RNG) k-ε model, and the Reynolds Stress Model (RSM). When considering the peak heat transfer coefficients, the standard k-ε model overpredicted the experimental results by less than 10%, while the RSM model underpredicted the results by approximately 15%. The RNG model showed the best agreement with the measurements for peak heat transfer values by correctly predicting the peak heat transfer coefficient at approximately 1300 W/m^2 K. When predicting the

low heat transfer coefficients on the tip, the RNG model proved to be the best. Overall, the authors concluded there was no significant difference in the results from the different models, and used the high Re k-ε model to generate results. Low heat transfer coefficients were observed on the shroud when compared to those on the blade tip. The highest heat transfer coefficient exists in the vicinity of the pressure side of the blade. Also, high heat transfer coefficients were observed in the downstream portion of the pressure side of the blade, which coincided with the region where passage flows were accelerating. On the other hand, low heat transfer coefficients were found on the suction side, which corresponded to the low-velocity flow between the leakage vortex and the suction side passage flow. Yang et al. (2002b) extended the work of Yang et al. (2002a), by generating the same results for a turbine blade with a squealer tip, and comparing them with the flat tip case. The numerical modeling in this study was identical to that in Yang et al. (2002a). High heat transfer coefficients on the shroud were found on the pressure side for both the flat tip and squealer tip blades, though this region was larger for the flat tip blade. For the squealer tip blade, the high heat transfer coefficient region was observed to be limited to an area coinciding with the thickness of the squealer rim, and was explained by the flow separation past the rim.

Kwak and Han (2003) used the transient liquid crystals technique to obtain detailed heat transfer coefficient distributions on the shroud surface of a stationary blow down facility at different tip gap sizes, which were 1.0%, 1.5%, and 2.5% of the blade span. They obtained the heat transfer coefficients on the shroud surface over a blade with a squealer tip, and compared it with that on the shroud surface over a plane tip blade without a

29

squealer tip. The squealer tip serves to reduce the leakage flow across the blade tip in the gap region. The heat transfer coefficient on the shroud of the squealer tip blade was lower than that for the plane tip blade. For the squealer tip, the heat transfer coefficient on the pressure side of the shroud was relatively low, while that on the shroud over the blade tip and on the suction side was higher due to the leakage flow through the tip gap.

In a similar study, Kwak et al. (2003) utilized the transient liquid crystals technique to obtain the heat transfer coefficient on the blade tip and shroud surface in a linear cascade test facility for different types of squealer tips. The results showed that the presence of a squealer tip aided in significantly lowering the heat transfer coefficient on the shroud. In all cases, the heat transfer coefficient on the shroud above the pressure side of the blade was lower than that above the suction side, as was observed by Kwak and Han (2003). High local heat transfer coefficients on the shroud have been observed downstream of the squealer rim, which is due to the leakage flow between the rim and shroud. When the squealer was located along the suction side of the blade tip, the overall heat transfer coefficient on the shroud was generally the lowest. In addition, the overall heat transfer coefficient increased with increasing tip gap clearance.

Azad et al. (2003) studied the effect of squealer tip arrangements in a five blade linear cascade using a transient liquid crystal technique. Results for the blade tip with a typical squealer showed that the heat transfer coefficient at the cavity bottom was higher in the upstream region. This was attributed to the presence of a re-circulating dead-flow zone in which the leakage flow is entrapped, thus causing lower heat transfer coefficients.

Another explanation was that the leakage flow becomes separated at the pressure side rim and then reattaches itself inside the cavity surface, thus high transfer is observed in the upstream central region of the cavity bottom. In addition, high heat transfer was observed on the suction side rim and trailing edge, which is probably caused by the leakage flow exiting out of the cavity and mixing with the main flow. The other two squealer geometries were called open squealer, which had a squealer rim positioned at the mid camber line and one on the pressure side and suction side, respectively. The open squealers showed low heat transfer coefficients in the trailing edge region. The mid squealer rim causes the flow to separate on the pressure side, causing lower heat transfer on the pressure side than on the suction side. Overall, the squealer with a mid rim and suction side rim showed the greatest amount of leakage flow reduction, and thus the lowest amount of heat transfer.

Jin and Goldstein (2003) obtained local mass transfer measurements on near-tip blade surfaces in a five blade linear cascade using a napththalene sublimation technique. The blade Reynolds numbers were similar to those found in a typical gas turbine engine, and the effects of the tip clearance, Reynolds number, and turbine intensity were studied. High mass transfer rates were observed at large tip clearances due to the strong acceleration of the flow in the large tip gap region. In general, there were higher mass transfer rates in the downstream region, which were caused by the presence of the tip leakage vortex. It was also observed that as Reynolds number increases, the local mass transfer rates also increase on both the pressure and suction sides of the blade. Likewise, high turbulent intensities generate higher local mass transfer rates, but on the pressure

surfaces only.

Acharya et al. (2003) used the same methodology as Yang et al. (2002a, 2002b) to numerically investigate the effects of different tip geometries on the flow and heat transfer of the same GE-E^3 turbine blade. These geometries are the flat tip, the winglet tip, the ribbed tip, and the S-Side squealer tip. Other tip geometries were investigated in order to compare the results to the experimental data of Azad et al. (2000), however only the geometries mentioned above were used in investigating the heat transfer on the shroud, and no experimental data was used for comparison of these results. The winglet tip was designed to be thickest at the position where the pressure difference is greatest across the blade. The ribbed tips had a series of ribs running across the blade tip placed at a slant from the normal of the mainstream flow direction. The S-side squealer tip had a squealer on the suction side of the blade. The winglet and ribbed tips were expected to reduce the tip leakage flow, and the numerical results showed that this was the case since the heat transfer to the shroud was reduced when compared to the flat tip and S-side squealer tip.

Willinger and Haselbacher (2004) presented a tip leakage loss model which accounted for off-design inlet flow angles or incidences. They obtained experimental data from a low-pressure blade cascade with exit Mach numbers of only 0.15. Thus, the flow was deemed incompressible. Their results showed that strength of the tip leakage vortex was increased slightly with the flow inlet angle. In addition, a vortex near the endwall was observed which rotated in the opposite direction of the tip leakage vortex, and was

associated with the passage vortex.

Mumic et al. (2004) also numerically predicted the heat transfer coefficients on the shroud, and compared their results to the experimental data for shroud heat transfer from Kwak and Han (2002, 2003) for a stationary linear cascade. FLUENT was used as the CFD solver, where the low Re k-ω shear stress transport (SST) was used model to account for the turbulence. Both flat tip blades and squealer tip blades were modeled, and their grids consisted of 1.6 million and 2 million cells, respectively. For the flat tip case, the results for the shroud heat transfer coefficient were generally in good agreement. Maximum heat transfer on the shroud occurred directly over the pressure side of the blade. However, contradictory results were observed when considering the effect of tip clearance size. As the tip clearance size increased, the experimental results showed reduced heat transfer on the shroud, while the computational results indicated an increase in heat transfer. In addition, the simulation failed to capture the region of high transfer downstream of the blade suction side that was present in the experiments. This high heat transfer region was due to the interaction of the leakage vortex and mainstream flow. For the squealer tip case, the shroud heat transfer results were in good agreement with the measured values, and the simulations captured the correct trends as well. Both experimental and computational results showed that the highest heat transfer occurred above the pressure side of the blade, and was attributed to the mainstream flow moving through the tip clearance gap from the pressure side to the suction side and subsequently impinging on the shroud. Low heat transfer was observed in the vicinity of the leading edge near the suction side.

In general, the tip leakage flow field above stationary blades is similar to that over rotating blades, with the development of the leakage vortex and separation bubble apparent in both cases. Thus, studies with stationary blades serve as a good starting point for understanding the tip gap flow field over rotating blades.

2.3 Summary

The review of the literature indicates that the flow field and corresponding heat transfer in the blade tip gap region are highly three-dimensional and complex. Today's advanced experimental and numerical techniques have allowed researchers to gain further insight into the loss mechanisms arising in the tip gap region. However, it is still quite difficult to visualize tip gap flow in actual clearance gaps of real turbines, which can be smaller than 1 mm in height. In addition, most studies have been conducted at low speeds which are not typical of the actual speeds found in gas turbine engines. Likewise, obtaining experimental measurements for heat transfer on the turbine shroud is extremely costly and difficult due to the high temperature gradients as well as the size of the gap, as mentioned before.

2.3.1 Tip Clearance Flow Field

Blade tip leakage flow, with no heat transfer, has been studied over rotating blades (Allen and Kofskey, 1955, Booth et al., 1982, Wadia and Booth, 1982, Yamamoto et al., 1994, Nikolos et al., 1995, Ristic et al., 1998, Xiao et al., 2001, McCarter et al., 2001, Tallman

and Lakshminarayana, 2001b, Hassavand et al., 2004, Lampart et al., 2004, Camci et al., 2005, Green et al., 2005, Palafox et al., 2005, Rhee and Cho, 2005). In addition, tip leakage flow has been investigated over stationary airfoils (Yaras et al., 2003, Yamamoto, 1994, Moore et al., 1989, Sjolander and Cao, 1995, Tallman and Lakshminarayana, 2001a, Azad et al., 2003, Jin and Goldstein, 2003, Willinger and Haselbacher, 2004). Simple models have been developed in order to describe the complex flow field (Yaras et al., 1989, Metzger et al. 1991, Nikolos et al., 1995, Hassanvand et al., 2004).

Also, it has been observed by numerous studies that tip leakage flow inside cascades is much more significant than that in rotating rotors.

- Data from stationary cascades studies varies significantly from rotating studies since the shroud's relative motion greatly affects the flow field in the tip gap region. Leakage flow and thus the leakage vortex strength tend to be less in rotating blade studies since much of the leakage flow leaves the gap region due to the obstruction caused by the shroud's boundary layer. Also, the opposing motion of the shroud on the tip leakage flow aids in reducing the tip leakage mass flow rate and momentum.

- While the leakage flow moves from the pressure side to the suction side of the blade tip, the shroud's relative motion moves from suction side to the pressure side, and this causes the leakage vortex to remain near the suction side.

- The development of the tip leakage vortex is dependent on the size of the tip

35

clearance where larger tip clearances allowed for higher mass transfer rates and thus larger vortices.

- Tip leakage flow is strongly dependent on secondary flows that are developed upstream of the rotor. The propagation of vane shock waves in the blade passage has more of a significant impact on the blade tip pressure than vane wakes. The blade tip pressure increases to a maximum value as the shock moves across the tip.

- Although, there are various simple models that have been generated over the years, a universal model of the complex flow field in the blade tip gap has not yet been developed.

2.3.1 Shroud Heat Transfer

Experimental and computational studies of the turbine shroud heat transfer have been conducted by considering either stationary blade cascades (Cho et al., 2001, Yang et al. 2002a, 2002b, Kwak and Han, 2003, Kwak et al., 2003, Acharya et al., 2003, Mumic et al., 2004) or rotational rates of the turbine blade (Dunn et al., 1984, Guenette et al., 1985, Kumada et al., 1994, Ameri Steinthorsson, 1996, Ameri et al., 1998, Chana and Jones, 2003, Polanka et al., 2003a, 2003b, Thorpe et al., 2004). The research regarding turbine shroud heat transfer has focused on the effects of flow conditions (Dunn et al., 1984, Guenette et al., 1985, Kumada et al., 1994, Cho et al., 2001, Chana and Jones, 2003, Polanka et al., 2003a, 2003b), tip clearance size (Kumada et al., 1994, Ameri and Steinthorsson, 1996, Kwak and Han, 2003, Kwak et al., 2003, Polanka et al., 2003a, 2003b, Mumic et al., 2004), and blade tip geometry (Ameri et al., 1998, Yang et al.,

2002a, 2002b, Acharya et al., 2003, Kwak et al., 2003, Mumic et al., 2004). It is extremely difficult to obtain heat transfer measurements on the shroud due to the intense aerothermal conditions in this area. The following points summarize the findings from the above references for shroud heat transfer.

- The rotation of the turbine rotor causes the heat transfer in the tip gap region to be unsteady and oscillatory as the blades pass over the shroud.

- The effect of flow conditions has been studied primarily through experiments, and it was observed that as the rotor velocity increases, the heat flux on the shroud also increases. However the effects of some other parameters still remain inconclusive. Recent studies have shown that the exit Reynolds number increases the heat transfer to the shroud, while past studies have shown no effect on Reynolds number. Also, contradictory reports exist for the effect of the inlet temperature profile, where some studies show a significant impact, while others do not.

- As the tip clearance gap increases, the region of high heat transfer increases due to the increase in leakage flow, which originates from the pressure side and moves towards the suction side. The maximum heat transfer, regardless of tip clearance size occurs on the pressure side. As the flow exits the gap, a leakage vortex is formed and its strength is increased, generating a high heat transfer region downstream of the blade suction surface.

- Comparisons between shroud heat transfer levels for flat-tip blade tips and squealer tips show that squealer tips lowered the heat transfer levels on the

shroud. Regions of high heat transfer occurred on the pressure side, and were much larger in magnitude for the flat-tip blade, while for the squealer tip blade, the region was confined within the thickness of the squealer tip.

2.4 Objectives and Contributions

The ability to fully comprehend the mechanics behind the flow and heat transfer will enable engineers to design effective cooling schemes in these turbine components, since they are characterized by extreme thermal conditions that may lead to premature failure. Three-dimensional numerical simulations of the flow and heat transfer in the tip gap region are a less costly alternative to experiments, and can potentially capture some flow or heat transfer behavior in areas where measurement instrumentation cannot. Shroud heat transfer data for stationary cascades may not necessarily be useful in the design of gas turbine engines, where rotating rotors exist. The rotation of the rotor causes the heat transfer on the shroud to be highly unsteady, and should therefore be modeled in computational work. The rotation of the rotor must be considered in order to correctly capture flow and thermal fields along the shroud. From the review of the literature, no unsteady simulations have been conducted, which focus on the flow structure and behaviour inside the tip clearance region.

This study has the following objectives:

1. Develop an appropriate numerical model combining the stator and rotor of a gas turbine engine, which can be utilized to capture the transient development of the

flow fields in the tip gap region.

2. Conduct a parametric investigation in order to study the effect of tip clearance height, inlet turbulence intensity, inlet stagnation temperature, and rotor angular velocity on the aerodynamics in the tip clearance region.

Chapter 3

Mathematical Modeling

The purpose of the present study is to conduct a parametric investigation of the various flow parameters on the tip leakage flow between the blade tip and shroud inside a gas turbine rotor. The flow inside gas turbine engines is turbulent and compressible, and it is imperative that the correct turbulence model be chosen for this investigation. The k-ω turbulence models were developed in order to predict the flow characteristics in wall-bounded turbulent flows whereby the near wall region is modeled all the way to the wall (near-wall modeling).

An industrially owned CFD code called Nistar was used in order to conduct the unsteady parametric investigation. Since the region of interest is the tip gap region, the shear-stress transport (SST) k-ω turbulence model was chosen since it is appropriate for wall-bounded flows, utilizing near wall modeling capabilities of the k-ω model while implementing a high Reynolds number turbulence model in bulk flow region away from the walls. Also, in order to obtain an appropriate initial solution for the unsteady cases, steady-state mixing plane simulations were first performed. Once the mixing plane case properly converged, time dependence was then implemented, and the unsteady simulation was initiated.

The commercial CFD software called FLUENT was also used in the present study in order to obtain time-dependent heat transfer data on the shroud. Steady-state mixing plane simulations were first performed in order to determine the appropriate setup for the unsteady cases. For the mixing plane simulations, the two domains meet at a mixing plane and not an interface. As a result, the flow information across the two domains is averaged out. Once the mixing plane results were deemed reasonable, a steady-state frozen rotor case was run using the identical set up variables in the solver as the mixing plane case, and was used as an initial solution for the time-varying unsteady case. In the frozen rotor case, the grid interface was defined but once again the rotor domain was considered as a moving reference frame, and not a moving mesh. After an appropriate number of iterations, time dependence was then applied by setting the rotor domain as a moving mesh. Unsteady heat transfer data was recorded on the shroud as a function of time.

In the present study, the shear stress transport (SST) k-ω turbulence model was selected in order to capture the flow characteristics in the tip gap region, since it combines both the k-ε model in the free-stream region, and the k-ω model in the near wall region. The following chapter provides all the relevant modeling equations as well as an overview of the modeling setup used in the CFD solver for the present study.

3.1 Governing Equations

3.1.1 Conservation Equations

For the present study, the flow through the gas turbine stage was considered to be three-dimensional, unsteady, compressible, and turbulent. Single-phase air was used as the working fluid. Other assumptions include no external fluid or heat sources as well as negligible gravitational forces. Consequently, the resulting governing flow and heat transfer equations are reduced to:

Conservation of Mass:

$$\frac{\partial \rho}{\partial t} + \nabla \cdot (\rho \vec{v}) = 0 \,. \tag{3.1}$$

Conservation of Momentum:

$$\frac{\partial}{\partial t}(\rho \vec{v}) + \nabla \cdot (\rho \vec{v} \vec{v}) = -\nabla p + \nabla \cdot (\bar{\bar{\tau}}), \tag{3.2}$$

where $\bar{\bar{\tau}}$ is the stress tensor defined by

$$\bar{\bar{\tau}} = \mu\left[(\nabla \vec{v} + \nabla \vec{v}^T) - \frac{2}{3}\nabla \cdot \vec{v} I \Big|_{\Big|} \right], \tag{3.3}$$

with I being the unit tensor.

Conservation of Energy:

$$\frac{\partial}{\partial t}(\rho E) + \nabla \cdot [\vec{v}(\rho E + p)] = \nabla \cdot [k_{eff}\nabla T + (\bar{\bar{\tau}}_{eff} \cdot \vec{v})], \tag{3.4}$$

where k_{eff} is the sum of the fluid's thermal conductivity and the turbulent thermal conductivity.

3.1.2 Compressibility Effects

Transonic flows, with Mach number approaching unity, are typically found in gas turbine stage rendering compressibility effects significant. The Mach number is defined as

$$M = \frac{V}{c}, \tag{3.5}$$

where V is the gas velocity and c is the speed of sound in the gas. In the present study, compressibility of the gas was considered by assuming that the air is an ideal gas. Thus, the density is given by the ideal gas law as follows:

$$\rho = \frac{p}{RT}, \tag{3.6}$$

where p is the absolute static pressure, R is the gas constant, and T is the static temperature.

Stagnation or total properties of gases are used as reference states for studying compressible flows. The total pressure (p_o) and the total temperature (T_o) are related to their static counterparts through the following equations:

$$\frac{p_o}{p} = \left(1 + \frac{\gamma-1}{2}M^2\right)^{\frac{\gamma}{\gamma-1}}, \tag{3.7}$$

and

$$\frac{T_o}{T} = 1 + \frac{\gamma-1}{2}M^2. \tag{3.8}$$

where γ is the ratio of specific heats $\left(c_p/c_v\right)$.

3.2 Modeling Turbulence

3.2.1 Reynolds Averaging Method

The flow inside a gas turbine engine is turbulent associated with high Reynolds numbers, disorderly motion, and most importantly high frequency fluctuations in the velocity field. Time-averaging or Reynolds averaging has been used as a means of analyzing turbulence by separating fluctuating properties with their time-mean values. Thus, the true velocity is defined by

$$u_i = \overline{u}_i + u_i', \tag{3.9}$$

where $\overline{u}$ is the ensemble average value of the velocity obtained over several experiments at the same location and at the same time. In addition, u' represents the fluctuation of the velocity from $\overline{u}$, and is a function of time and space (Ghaly, 2004). The subscript $i = 1$, 2, 3 and represents x, y, and z components of the velocity vector, respectively.

When Equation 3.9 is inserted into Equations 3.1 and 3.2, the Reynolds-averaged Navier-Stokes (RANS) equations are obtained by considering only terms with the time averaged values. The RANS equations are given below and it should be noted that the overbar on the mean velocity has been removed:

$$\frac{\partial \rho}{\partial t} + \frac{\partial}{\partial x_i}(\rho u_i) = 0, \tag{3.10}$$

and

$$\frac{\partial}{\partial t}(\rho u_i) + \frac{\partial}{\partial x_i}(\rho u_i u_j) = -\frac{\partial p}{\partial x_i} + \frac{\partial}{\partial x_j}\left[\mu\left(\frac{\partial u_i}{\partial x_j} + \frac{\partial u_j}{\partial x_i} - \frac{2}{3}\delta_{ij}\frac{\partial u_l}{\partial x_l}\right)\right] + \frac{\partial}{\partial x_j}\left(-\rho\overline{u_i' u_j'}\right). \tag{3.11}$$

The RANS equations are similar to the instantaneous equations given in Section 3.1.1 with an extra term in the momentum equation which corresponds to turbulence effects. This extra term includes what is called the Reynolds stresses $(-\rho \overline{u_i' u_j'})$ and must be appropriately modeled so that the RANS equations may be solved. In other words, another equation is required in order to close the above system of equations.

One such equation is the Boussinesq hypothesis which relates the Reynolds stresses to the mean velocity gradients:

$$-\rho \overline{u_i' u_j'} = \mu_t \left(\frac{\partial u_i}{\partial x_j} + \frac{\partial u_j}{\partial x_i} \right) - \frac{2}{3} \left(\rho k + \mu_t \frac{\partial u_i}{\partial x_i} \right) \delta_{ij} \qquad (3.12)$$

The Boussinesq hypothesis has been employed in many turbulence models including the shear-stress transport (SST) k-ω model, which was used in the present study to investigate the flow interaction with the rotor shroud. The SST k-ω model was developed by Menter (1994), and implements both the standard k-ε and standard k-ω models, whereby the standard k-ω model is activated in the boundary layer region while the standard k-ε model is used in the free-stream region.

3.2.2 The Shear-Stress Transport (SST) k-ω Model

The shear-stress transport (SST) k-ω model is a variation of the standard k-ω model, which accounts for transport of the principal turbulent shear stress. The standard k-ε

model is activated in the free-stream, while the standard k-ω model is applied inside the boundary layer. This is achieved by implementing blending functions as well as adding a cross-diffusion term in the ω transport equation. Thus, the transport equations for the SST k-ω model are

$$\frac{\partial}{\partial t}(\rho k) + \frac{\partial}{\partial x_i}(\rho k u_i) = \frac{\partial}{\partial x_j}\left(\Gamma_k \frac{\partial k}{\partial x_j}\right) + \tilde{G}_k - Y_k \qquad (3.13)$$

and

$$\frac{\partial}{\partial t}(\rho \omega) + \frac{\partial}{\partial x_i}(\rho \omega u_i) = \frac{\partial}{\partial x_j}\left(\Gamma_\omega \frac{\partial \omega}{\partial x_j}\right) + G_\omega - Y_\omega + D_\omega. \qquad (3.14)$$

Here, $\tilde{G}_k$ is the production of the turbulent kinetic energy (k) due to the mean velocity gradients, while G_ω symbolizes the production of the specific dissipation rate (ω). In addition, Γ_k and Γ_ω are the effective diffusivities of k and ω, respectively, while Y_k and Y_ω are the turbulence dissipation of k and ω. The additional term in the ω transport equation D_ω is the cross diffusion term, which is defined in the Appendix.

Before defining terms in the equations above, it is important to present the turbulent viscosity in the SST k-ω model as well as the blending functions. The turbulent viscosity, μ_t, is given by

$$\mu_t = \frac{\rho k}{\omega} \times \frac{1}{\max\left[\frac{1}{\alpha^*}, \frac{SF_2}{a_1\omega}\right]}, \qquad (3.15)$$

46

where S is the magnitude of the strain rate defined by $S = \sqrt{2S_{ij}S_{ij}}$ and $a_1 = 0.31$. The

term α^* is found from $\alpha^* = \alpha_\infty^* \left(\dfrac{\alpha_0^* + \mathrm{Re}_t / R_k}{1 + \mathrm{Re}_t / R_k} \right)$ with $R_k = 6$ and $\alpha_\infty^* = 1$, while F_2 is one

of the blending functions defined in the Appendix.

Now, the effective diffusivities of k and ω are found from $\Gamma_k = \mu + \dfrac{\mu_t}{\sigma_k}$ and

$\Gamma_\omega = \mu + \dfrac{\mu_t}{\sigma_\omega}$, where σ_k and σ_ω are the turbulent Prandlt numbers for k and ω,

respectively, with $\sigma_k = \sigma_\omega = 2.0$. In this case, however, the turbulent viscosity defined

in Equation 3.15 is used instead. Thus, the definitions of the turbulent Prandtl numbers

for k and ω (σ_k and σ_ω) are different, and are as follows:

$$\sigma_k = \frac{1}{F_1 / \sigma_{k,1} + (1 - F_1) / \sigma_{k,2}} \tag{3.16}$$

and

$$\sigma_\omega = \frac{1}{F_1 / \sigma_{\omega,1} + (1 - F_1) / \sigma_{\omega,2}}. \tag{3.17}$$

The constants $\sigma_{k,1}$, $\sigma_{k,2}$, $\sigma_{w,1}$, and $\sigma_{w,2}$ are given by $\sigma_{k,1} = 1.176$, $\sigma_{k,2} = 1.0$, $\sigma_{\omega,1} = 2.0$,

and $\sigma_{\omega,2} = 1.168$, respectively. The blending functions F_1 and F_2 have been defined in

the Appendix.

47

3.3 Wall Treatment in k-ω Models

When turbulent flow moves over a wall, a region in which viscous effects are dominant is found adjacent to the wall due to the no-slip boundary condition. This region is divided into three sub-regions: the viscous sublayer, the buffer layer, and the fully turbulent region. In the viscous sublayer, viscous effects dominate and the flow is considered to be laminar. In the fully turbulent region, turbulence effects govern while in the buffer layer, both viscous and turbulent effects are equally significant. Turbulent flow interaction with walls can be treated using either wall functions or near-wall modeling. Wall functions are semi-empirical formulas applied to bridge the region between the wall and the fully turbulent flow, and are often used in order to save computational resources. They are usually implemented when wall interaction is of relatively little importance. In near-wall modeling, the mesh extends all the way to the wall and includes even the viscous sublayer. The SST k-ω model was developed for near wall modeling, and was chosen for the present study since the solution variable gradients are very high in the tip gap region of the gas turbine rotor and should be resolved as accurately as possible.

3.3.1 Enhanced Wall Treatment

In the k-ω turbulence models, the wall boundary conditions for the k equation are accounted for through enhanced wall treatment, which are used in k-ε models. In the enhanced wall treatment, a two-layer model is combined with enhanced wall functions in order to model the flow near the wall. The domain is subdivided into a viscosity affected

48

region and a fully turbulent region, and its location is determined by the following Reynolds number based on distance from the wall:

$$\mathrm{Re}_y \equiv \frac{\rho y \sqrt{k}}{\mu} , \qquad (3.18)$$

where y is the normal distance of the cell centers from the wall. This y could be considered as the distance to the nearest wall using the following formula:

$$y \equiv \min_{\vec{r}_w \in \Gamma_w} \left\| \vec{r} - \vec{r}_w \right\| , \qquad (3.19)$$

where $\vec{r}$ is the position vector of a point in the domain and $\vec{r}_w$ is the position vector on the wall boundary. The symbol Γ_w signifies the union over all wall boundaries involved. This definition allows y to be distinctively defined even in complex flow domains with multiple walls, and is independent of mesh topology.

It is important to provide some general definitions of some dimensionless terms. The symbol u_τ is called the wall friction velocity and is defined as

$$u_\tau = \sqrt{\frac{\tau_w}{\rho}} , \qquad (3.20)$$

where τ_w is the shear stress at the wall. In addition, when u_τ is used to normalize the velocity u, the following term is obtained:

$$u^+ = \frac{u}{u_\tau} . \qquad (3.21)$$

In the SST k-ω model, when $\mathrm{Re}_y > 200$, the flow is considered to be in the fully turbulent region, and so the standard k-ε model is activated. When $\mathrm{Re}_y < 200$, the flow is in the

49

viscosity-affected region, and so the one-equation model of Wolfstein (1969) is applied. Near the wall, the momentum and k transport equations as described above are retained, while the turbulent viscosity is obtained from the following two layer definition:

$$\mu_{t,2\text{layer}} = \rho C_\mu l_u \sqrt{k}. \tag{3.22}$$

Here, l_u is the length scale defined as

$$l_u = y c_l \left(1 - e^{-\text{Re}_y/A_\mu}\right) \tag{3.23}$$

with $c_l = \kappa C_\mu^{-3/4}$, and $A_\mu = 70$. The symbol κ is the von Karman constant $\kappa = 0.4187$, while the constant $C_\mu = 0.09$ (in the standard k-ε model). The high Reynolds number turbulent viscosity μ_t applies in the outer region, and is blended with the two layer definition as shown in the following equation:

$$\mu_{t,\text{enh}} = \lambda_\varepsilon \mu_t + (1 - \lambda_\varepsilon) \mu_{t,2\text{layer}}. \tag{3.24}$$

The blending function is given by

$$\lambda_\varepsilon = \frac{1}{2}\left[1 + \tanh\left(\frac{\text{Re}_y - \text{Re}_y^*}{A}\right)\right], \tag{3.25}$$

where $\text{Re}_y^* = 200$ and A is a constant which determines the width of the blending function. It is important to note that the blending function is equal to unity in regions far away from the walls, and equal to zero in the very near wall region. When the value of λ_ε is to be within 1% of its far field value, for a given variation ΔRe_y, A is computed as

$$A = \frac{|\Delta\text{Re}_y|}{\tanh(0.98)}. \tag{3.26}$$

The blending function allows the solution to continue to converge even when the k-ε

solution in the outer region does not match that of the two-layer formulation. The values

of ΔRe_y are typically set between 5% and 20% of Re_y^*.

The enhanced wall functions serve to blend the laminar (linear) and turbulent (logarithmic) regions by implementing a single wall law for the entire near wall region. This was done by Kader (1981) through the following equation:

$$u^+ = e^{\Gamma} u_{lam}^+ + e^{\frac{1}{\Gamma}} u_{turb}^+ ,$$

(3.27)

where Γ is the blending function defined as

$$\Gamma = -\frac{a\left(y^+\right)^4}{1 + by^+}$$

(3.28)

with $a = 0.01$ and $b = 5$. The term y^+ is defined as

$$y^+ \equiv \frac{\rho u_\tau y_p}{\mu_p} ,$$

(3.29)

where y_p is the distance from the point P to the wall, and μ_p is the viscosity at point P.

The enhanced wall function for compressible flow and heat transfer and pressure gradients combines the models presented by White and Christoph (1971) and Huang et al. (1993), and is as follows:

$$\frac{du_{turb}^+}{dy^+} = \frac{1}{\kappa y^+}\left[S'\left(1 - \beta' u^+ - \gamma'\left(u^+\right)^2\right)\right]^{1/2} ,$$

(3.30)

where

51

$$S' = \begin{cases} 1 + \alpha' y^+ & \text{for } y^+ < y_s^+ \\ 1 + \alpha' y_s^+ & \text{for } y^+ \geq y_s^+ \end{cases} \tag{3.31}$$

with

$$\alpha' \equiv \frac{\nu_w}{\tau_w u_\tau} \frac{dp}{dx} = \frac{\mu}{\rho^2 (u_\tau)^3} \frac{dp}{dx}, \tag{3.32}$$

$$\beta' \equiv \frac{\sigma_t q_w u_\tau}{c_p \tau_w T_w} = \frac{\sigma_t q_w}{\rho c_p u_\tau T_w}, \tag{3.33}$$

$$\gamma' \equiv \frac{\sigma_t (u_\tau)^2}{2 c_p T_w}. \tag{3.34}$$

Here, y_s^+ is the location where the log-law slope will remain constant, and has a default

value of $y_s^+ = 60$.

Now, the laminar law-of-the-wall is computed from

$$\frac{du_{lam}^+}{dy^+} = 1 + \alpha y^+, \tag{3.35}$$

which includes only pressure gradients effects since heat transfer and compressibility

effects are considered negligible near the wall. Thus, integrating Equation 3.35 yields

$$u_{lam}^+ = y^+ \left(1 + \frac{\alpha}{2} y^+ \right). \tag{3.36}$$

The enhanced thermal wall functions are determined using similar methods as those for

determining the u^+ profiles:

$$T^+ = e^{\Gamma} T_{lam}^+ + e^{\frac{1}{\Gamma}} T_{turb}^+ ,\qquad(3.37)$$

where

$$\Gamma = -\frac{a\left(\Pr y^+\right)^4}{1 + b\,\Pr^3 y^+}\qquad(3.38)$$

with $a = 0.01$ and $b = 5$.

Now, the wall boundary conditions for ω are as follows. The value of ω at the wall is given by

$$\omega_w = \frac{\rho u_\tau^2}{\mu}\,\omega^+ .\qquad(3.39)$$

In the laminar sublayer, the asymptotic value of ω^+ may be obtained from

$$\omega^+ = \min\left(\omega_w^+,\ \frac{6}{\beta_i\left(y^+\right)^2}\right),\qquad(3.40)$$

where

$$\omega_w^+ = \begin{cases} \left(\dfrac{50}{k_s^+}\right) & k_s^+ < 25 \\[4mm] \dfrac{100}{k_s^+} & k_s^+ \geq 25 \end{cases}\qquad(3.41)$$

with

$$k_s^+ = \max\left(1.0,\ \frac{\rho k_s u_\tau}{\mu}\right).\qquad(3.42)$$

Here, the term k_s represents the height of the roughness.

53

In the logarithmic (turbulent) region, ω^+ is defined by

$$\omega^+ = \frac{1}{\sqrt{\beta_\infty^*}} \frac{du_{turb}^+}{dy^+},$$
(3.43)

which yields the value of ω near the wall as

$$\omega = \frac{u_\tau}{\sqrt{\beta_\infty^*} \kappa y}$$

with $\beta_\infty^* = 0.09$ and $\kappa = 0.41$.

3.4 Flow Inside a Rotating Reference Frame

Flows in rotating reference frames can be modeled by including the acceleration of the reference frame in the equations of motion. Flows can be solved in the absolute reference frames using either the absolute velocity $\vec{v}$ or the relative velocity $\vec{v}_{rel}$, respectively. The two velocities are related by

$$\vec{v}_{rel} = \vec{v} - \left(\vec{\Omega} \times \vec{r}\right),$$
(3.44)

where $\vec{\Omega}$ is angular velocity vector of the rotating reference frame and $\vec{r}$ is the position vector measured in the rotating frame.

The equations for conservation of mass in both the absolute and rotating reference frames are identical:

$$\frac{\partial \rho}{\partial t} + \nabla \cdot \left(\rho \vec{v}\right) = 0.$$
(3.45)

54

The left hand side of the momentum equation which is applied in the absolute reference frame is given in Equation 3.2:

$$\frac{\partial}{\partial t}(\rho \vec{v}) + \nabla \cdot (\rho \vec{v} \vec{v}).$$

When the rotation of the reference frame is taken into account, the left hand side of the momentum equation in terms of the absolute velocity is

$$\frac{\partial}{\partial t}(\rho \vec{v}) + \nabla \cdot (\rho \vec{v}_r \vec{v}) + \rho(\vec{\Omega} \times \vec{v}). \tag{3.46}$$

In terms of the relative velocity, the left hand side of the momentum equation becomes

$$\frac{\partial}{\partial t}(\rho \vec{v}_r) + \nabla \cdot (\rho \vec{v}_r \vec{v}_r) + \rho(2\vec{\Omega} \times \vec{v}_r + \vec{\Omega} \times \vec{\Omega} \times \vec{r}) + \rho \frac{\partial \vec{\Omega}}{\partial t} \times \vec{r}, \tag{3.47}$$

where the term $\rho(2\vec{\Omega} \times \vec{v}_r)$ is called the Coriolis force.

3.5 Treatment of Multiple Reference Frames

The purpose of the present work is to study the effect of time variation on flow characteristics in the tip leakage region adjacent to gas turbine shrouds. Thus, unsteady simulations will be conducted with both the stator and rotor modeled. To do so, multiple reference frames must be defined since the stator flow domain is stationary, while the rotor flow domain rotates as time progresses. Also, a reliable steady-state solution is required as an initial solution for the unsteady simulations. For the unsteady simulations, sliding meshes were implemented where the rotor mesh changes position at each time step, thus allowing for time-accurate solutions to be obtained. The mixing plane approach was utilized to obtain the required steady-state solution for the unsteady

simulations.

3.5.1 Time-Averaged Solution

The main idea behind the mixing plane approach is that each flow domain is solved as a steady-state problem. Here, circumferentially averaged flow data from adjacent flow domains are passed as boundary conditions at the mixing plane interface. Thus, the spatially averaged profiles of flow data at the stator outlet will be the conditions for the rotor at its inlet. Any unsteadiness in the circumferential direction, such as wakes, shock waves, and separated flow, will be removed thus yielding a steady-state, time-averaged solution.

In summary, the solution algorithm for the mixing plane approach is as follows:

1. Update the solution within the stator and rotor flow domains

2. Compute the circumferentially-averaged flow properties at the stator outlet and rotor inlet in order to obtain appropriate profiles.

3. Pass the profiles as boundary conditions at the mixing plane.

4. Repeat Steps 1-3 until convergence.

3.5.2 Time-Accurate Solution

Sliding meshes are required in order to obtain time-accurate results for rotor-stator interaction, and is the most computationally demanding when simulating flows with multiple moving reference frames. Here, the stator flow domain and rotor flow domain are generated separately with an interface boundary condition defined as the plane where

the stator and rotor flow domains coincide. The two interface boundaries are then used to form a "grid interface", which allows the domains to move (or slide) relative to each other at this boundary. It is important to note that node alignment at the grid interface is not required.

In order to compute the flow data at the interface, the intersection between the interfaces is determined. If there are fluid zones on both sides of the interface, then an interior zone is created. If not, periodic zones are created. A two-dimensional example is shown in Figure 3.1. Interface Boundary 1 consists of Faces AB and BC and belongs to Flow Domain 1. Similarly, Interface Boundary 2 resides in Flow Domain 2, and contains Faces DE and EF. Here, the intersection of both flow domains yields faces ad, db, be, ec, and cf. If there is flow on both sides of the intersection, that is, where the two flow domains overlap (db, be, and ec) are grouped to form an interior zone, and the remaining faces (ad and cf) form periodic zones. Thus, the flux across the grid interface from Cells I and II to Cell IV is computed using faces db and be.
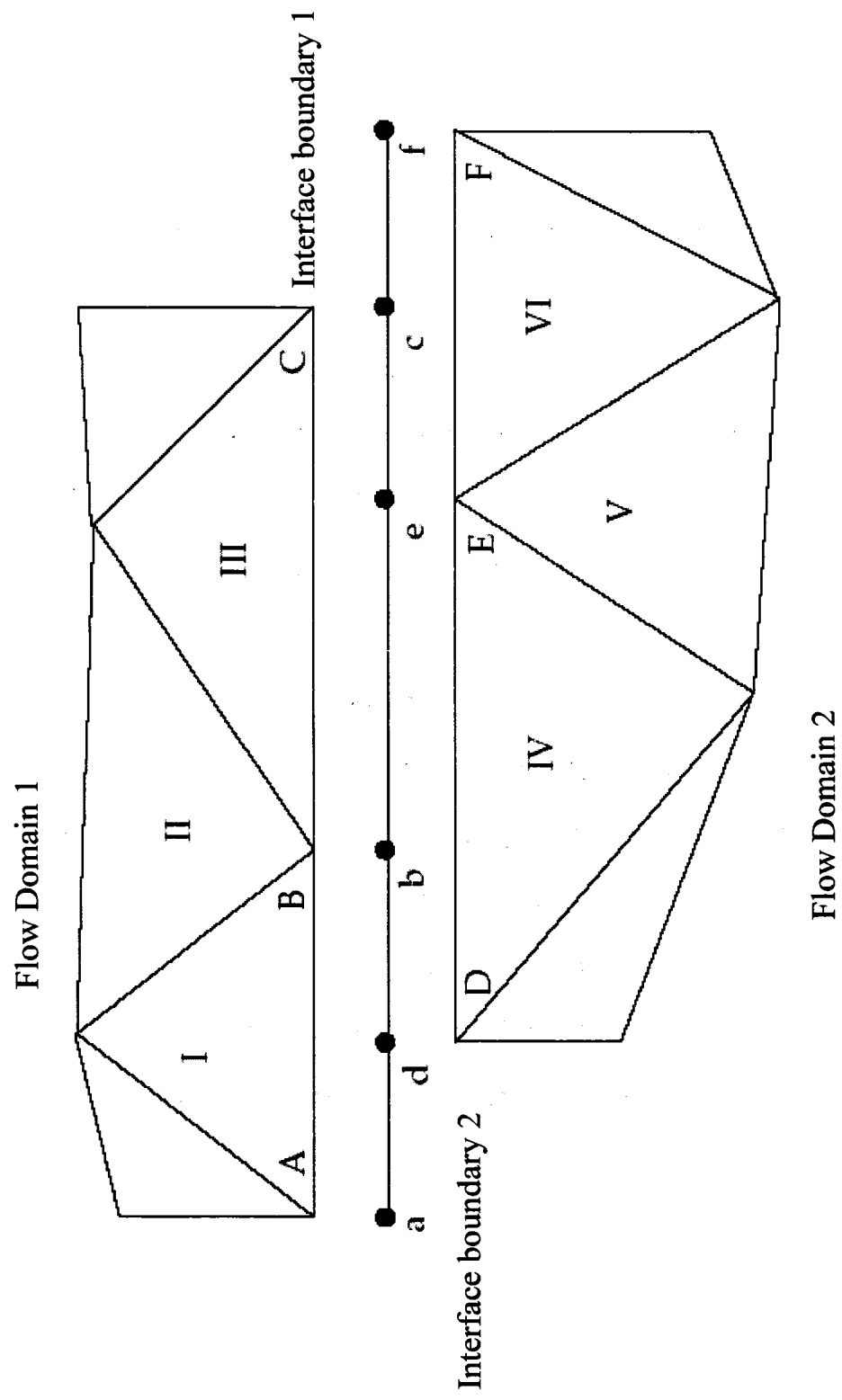
Figure 3.1 Grid interface in two-dimensions (FLUENT, 2005).

58

3.6 Method of Solution

3.6.1 Aerodynamic Calculations

In the present study, the turbine stage including the nozzle guide vane (NGV) as well as the rotor will be modeled and simulated using a 3D RANS finite volume code currently used in the aerospace industry. Description of the code may be found in Ni (1982), Ni and Bogoian (1989) and Davis et al. (1996). The viscous grids generated by the code are structured meshes and provide y^+ values less than 1 on all wall surfaces, which ensures that the SST k-ω turbulence model is being implemented correctly. The NGV is modeled in order to obtain a realistic pressure distribution at the inlet of the rotor, which includes the effects of wakes originating in the NGV. Total pressure and total temperature were specified at the inlet of the vane domain, while static pressure was set at the outlet of the rotor domain. One vane passage and one rotor passage were modeled in the steady state simulations, while one vane and two blade passages were modeled for the unsteady simulations. For the unsteady simulations, rotationally periodic boundary conditions were used in order to model the lowest number of vanes and blades such that the periodic angle of both the NGV and rotor is identical. The turbine stage under investigation in the present study consists of 30 vanes and 60 blades. Therefore, the computational domain for the unsteady simulations consists of 1 vane and 2 blades, yielding a periodic angle of 12° for both the NGV and rotor. A typical computational domain with both the NGV and rotor is shown in Figure 3.2.
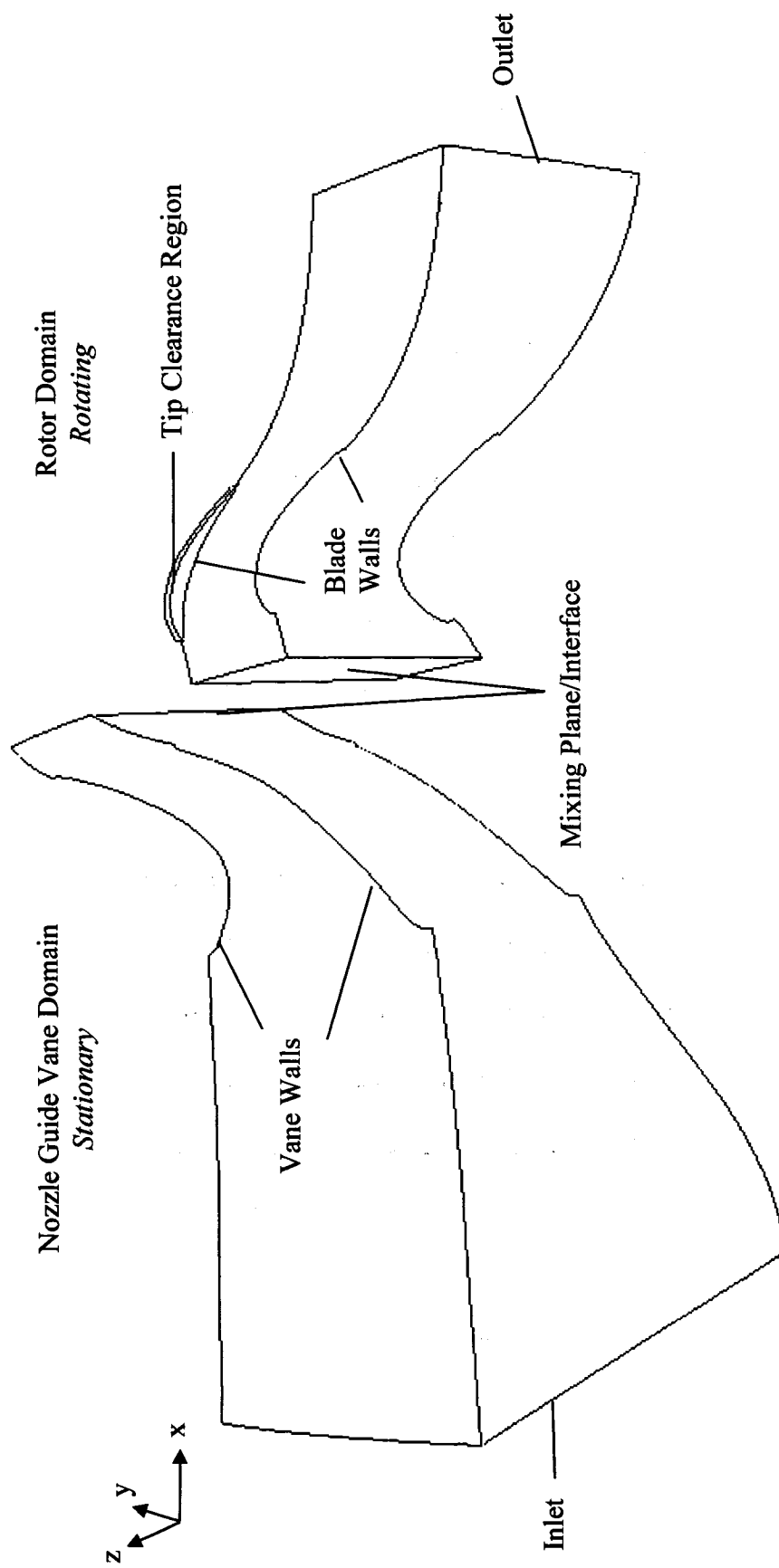
Figure 3.2 Depiction of the nozzle guide vane domain and rotor domain as modeled by Nistar.

60

In the present study, H-meshes were used for both the vane and rotor domains, where the number of nodes in the axial, circumferential, and radial directions of the domains were specified. The node count in the radial direction was set at 49, while the node counts in the axial and circumferential directions were varied such that the multi-grid level was greater than 3 in order to ensure fast convergence of the solution. In addition, the node counts on the leading edge, the airfoil surface, and the trailing edge were also specified in order to accurately depict the shape of the airfoil. The code also generates a tip clearance region just above the blade tip in the rotor domain with a node count of 16 in the radial direction in the tip leakage region. Thus, the total node count in the radial direction in the rotor domain was 65. For the unsteady simulations, a time step size of 1.05262×10^{-6} seconds was used, which is the time required such that 200 time steps are required to traverse one stator pitch of 12°, while 10 inner iterations per time step were used.

It is important to note that the data was recorded on planes called I-planes, J-planes, and K-planes. Figure 3.3 shows the grid of a typical K-plane in which I-planes and J-planes can be seen. As mentioned before, the meshes that are generated are structured and yield y^+ values of less than 1. As a result, the meshes are very fine near the airfoil walls. Similarly, Figure 3.4 shows a typical I-plane, in which the tip clearance grid can also be seen. Once again, finer meshes can be seen close to the airfoil walls as well as the shroud. A node count of 49 was used in the radial direction, with and additional 16 nodes in the tip clearance region, which can be seen in Figure 3.4. A grid independence test was conducted in order to determine the optimal node counts in the axial and
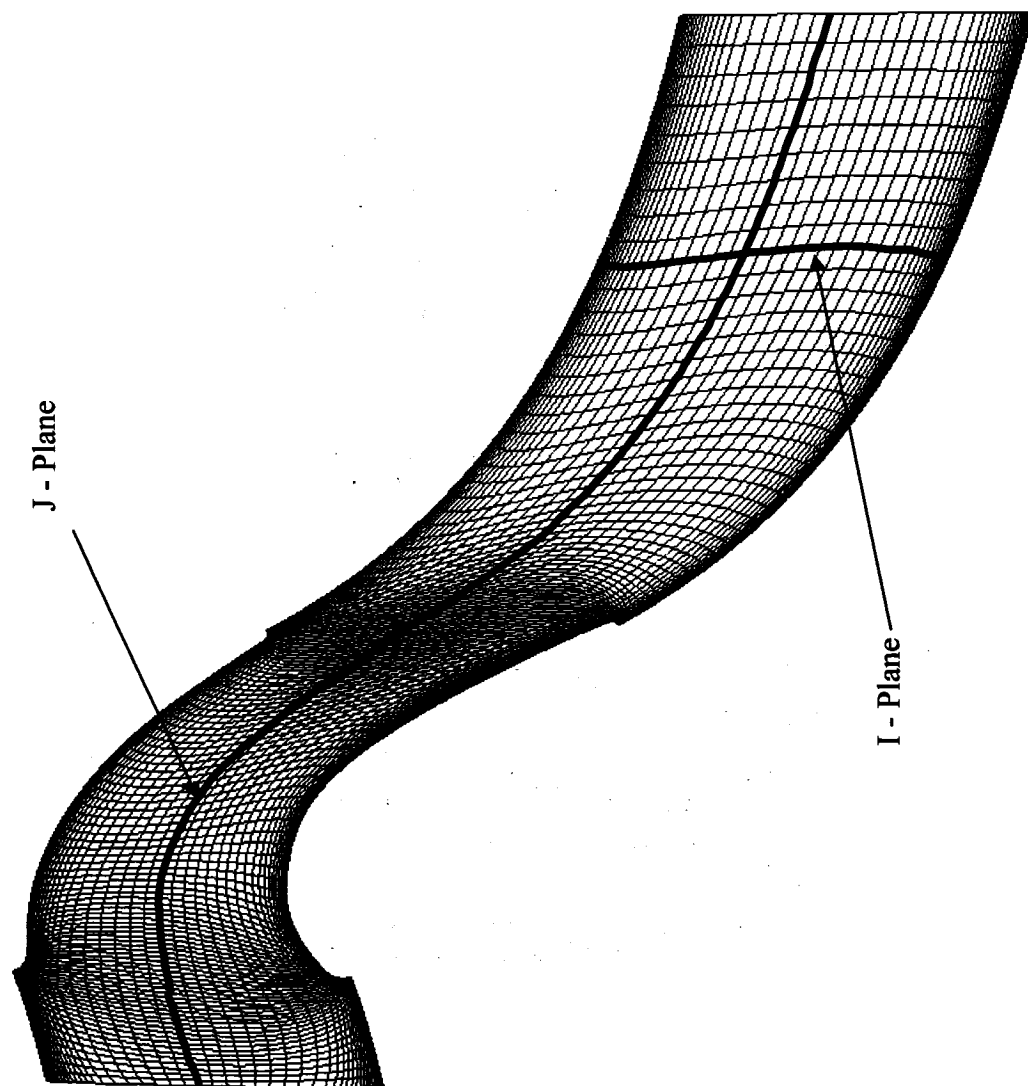
J - Plane

I - Plane

Figure 3.3 Depiction of I – and J- planes on a typical K – plane taken at midspan of the rotor domain.

62
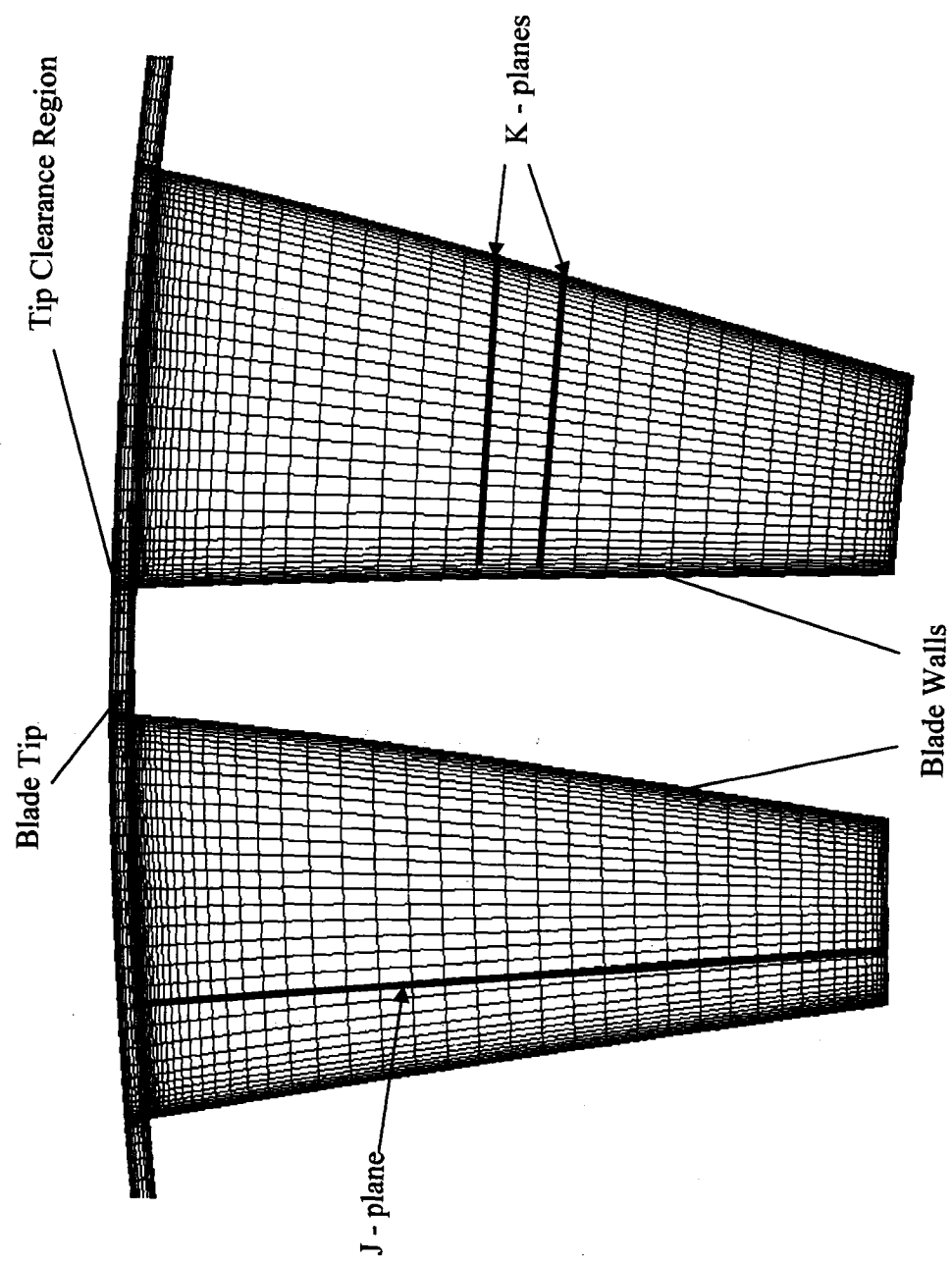
Figure 3.4 Depiction of J – and K- planes on a typical I – plane taken at midspan of the rotor domain.

63

circumferential directions, and will be presented in the following chapter.

The convergence for the steady-state simulations was determined by assuring that the mass flow rates, the total pressure, and static pressure at the inlet and outlet of each domain remain constant over a large number of iterations. In the present study, the steady-state simulations were allowed to run for 5000 iterations. The converged steady-state solution was used as an initial solution for the unsteady simulations. For the unsteady simulations, it is important that the solution attains time periodicity before results are recorded. As a result, the simulation was allowed to run for 2000 time steps or 10 vane passing periods, and the convergence parameters at the inlet and outlet of the domains were recorded to determine time periodicity.

3.6.2 Heat Transfer Calculations

The code used to study the tip leakage aerodynamics is currently not capable of studying unsteady heat transfer characteristics on the shroud. As a result, the commercial CFD software FLUENT Version 6.2.16 was used in the present study to predict the heat transfer on the shroud. Here, second order upwind discretization schemes were used for the flow, turbulent kinetic energy, and specific dissipation rate. The SST k-ω turbulence model was chosen, and the coupled explicit solver was used to simultaneously solve the continuity, momentum, energy, k transport, and ω transport equations in this compressible flow problem. The air density was calculated in the solver according to the ideal gas law. All other air properties such as viscosity, thermal conductivity, and

64

specific heat capacity were considered to vary with temperature in a piecewise linear fashion.

In the present study, the geometries of the vane and blade domains were created in CATIA Version 4 and were provided by the industry. The mesh generation tool called ICEMCFD Version 4.2.0 was then used to generate the meshes. Grid generation specifications were provided by Marini (2005), and were used to ensure the best possible prediction of the tip gap flow field as well as the heat transfer on the shroud. For the FLUENT calculations, the flow areas surrounding the airfoils are modeled. The computational domains for the NGV and rotor are shown in Figures 3.5 and 3.6. The computational domains were comprised entirely of unstructured tetrahedral elements, with the exception of prism elements (boundary layers) along all the walls in the domain. Figures 3.7 and 3.8 show some prism elements (boundary layers) that were placed on the airfoils, blade tip, as well as on the shroud. For both the vane and blade domains, it was ensured that the number of tetrahedral elements in the circumferential direction was between 20 and 40. On the airfoil pressure sides and suctions sides, thirty to forty elements were created in both the spanwise and chordwise directions in order to accurately capture flow physics and heat transfer along the airfoil. In the vane domain, five to ten prism layers were placed along all walls to obtain a high Reynolds turbulence y^+ range between 15 and 30. This was deemed acceptable since the surface of interest is in the rotor domain and not the vane domain, and an excessive amount of computational resources would be used if the vane domain grid were too fine. In the rotor domain, all walls except the shroud had five to ten prism layers attached to it, while ten to twenty
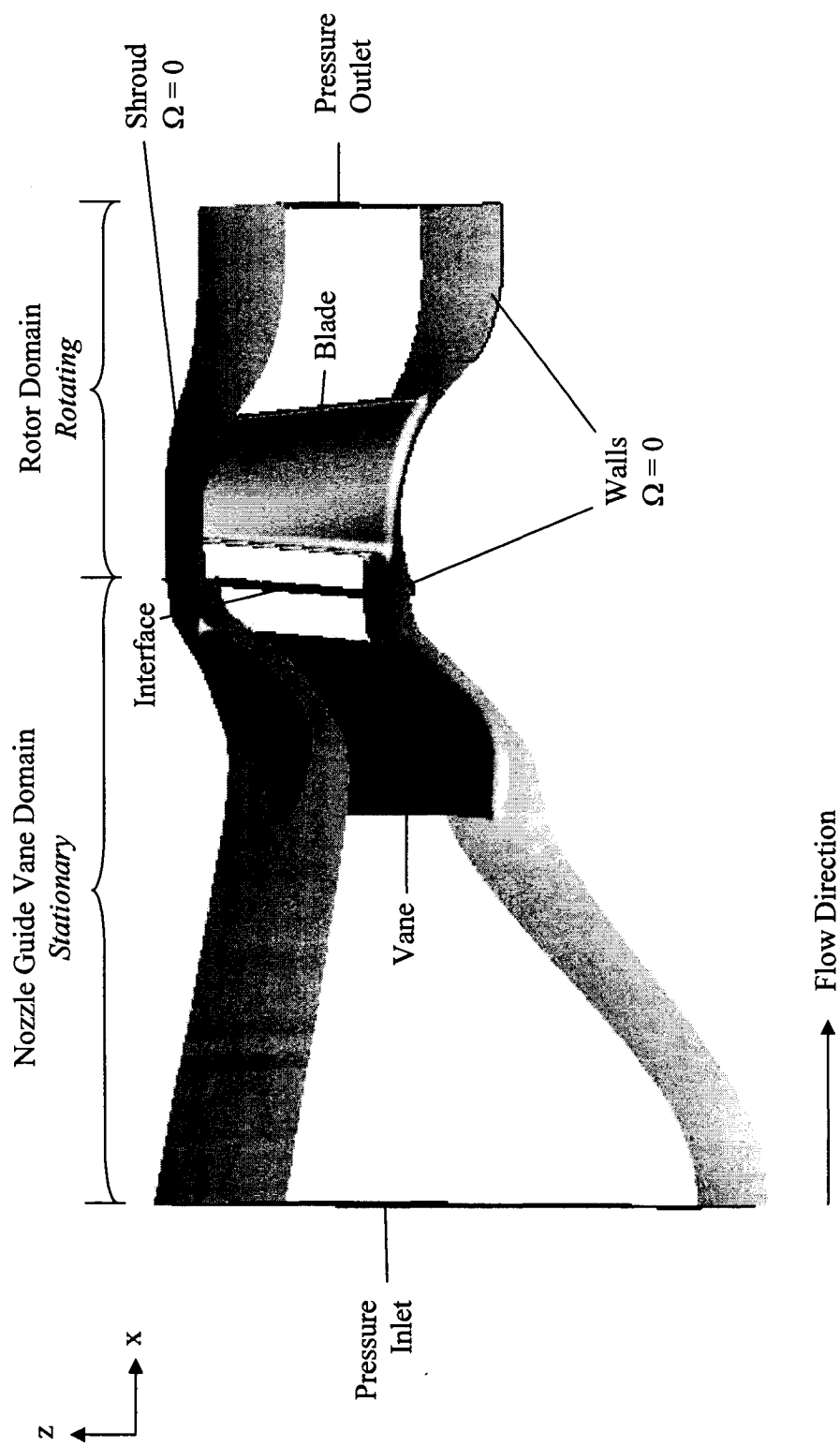
Figure 3.5 Computational domains and boundary conditions for nozzle guide vane and rotor with periodic surfaces removed.

66
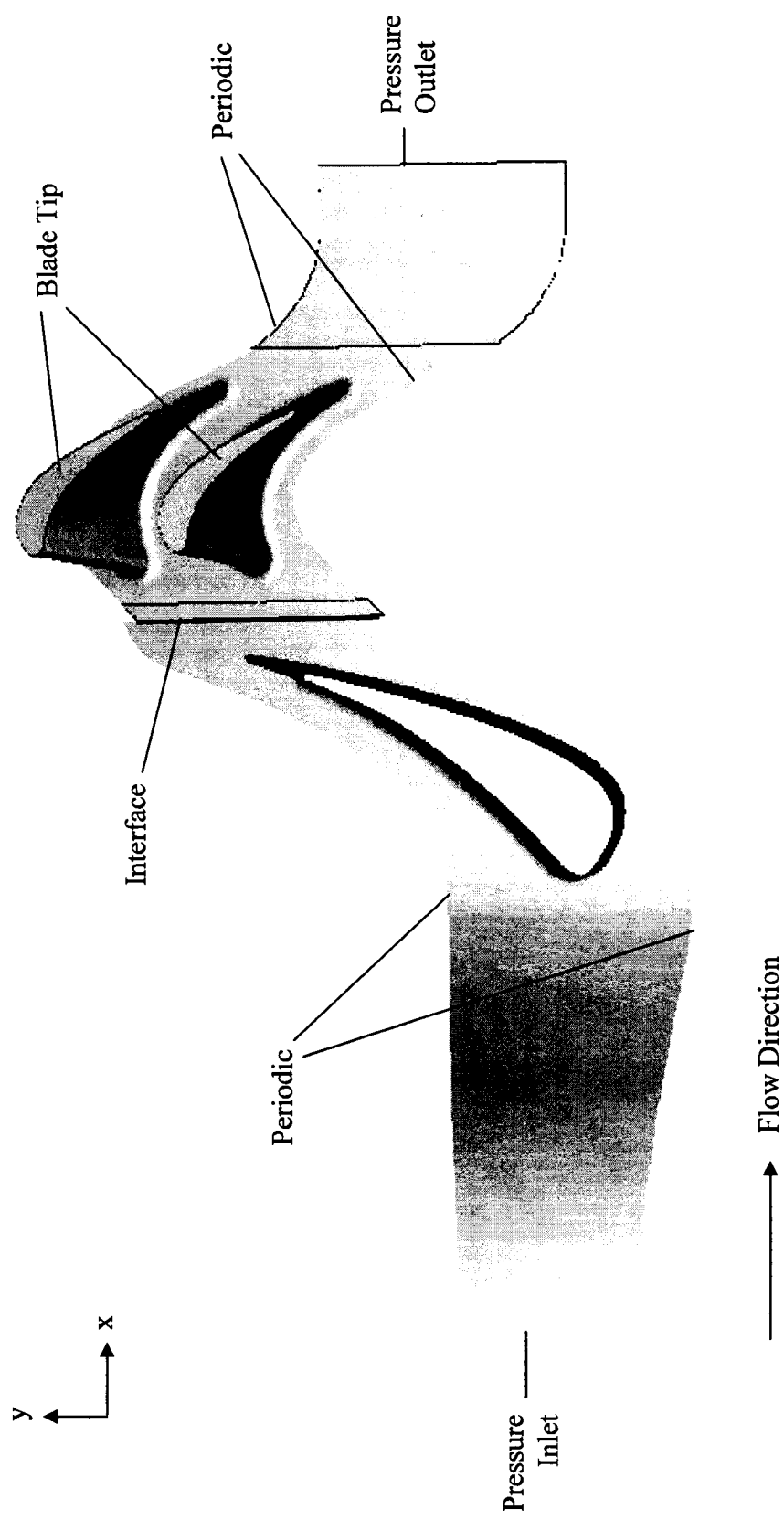
Figure 3.6 Computational domains with outer walls removed.
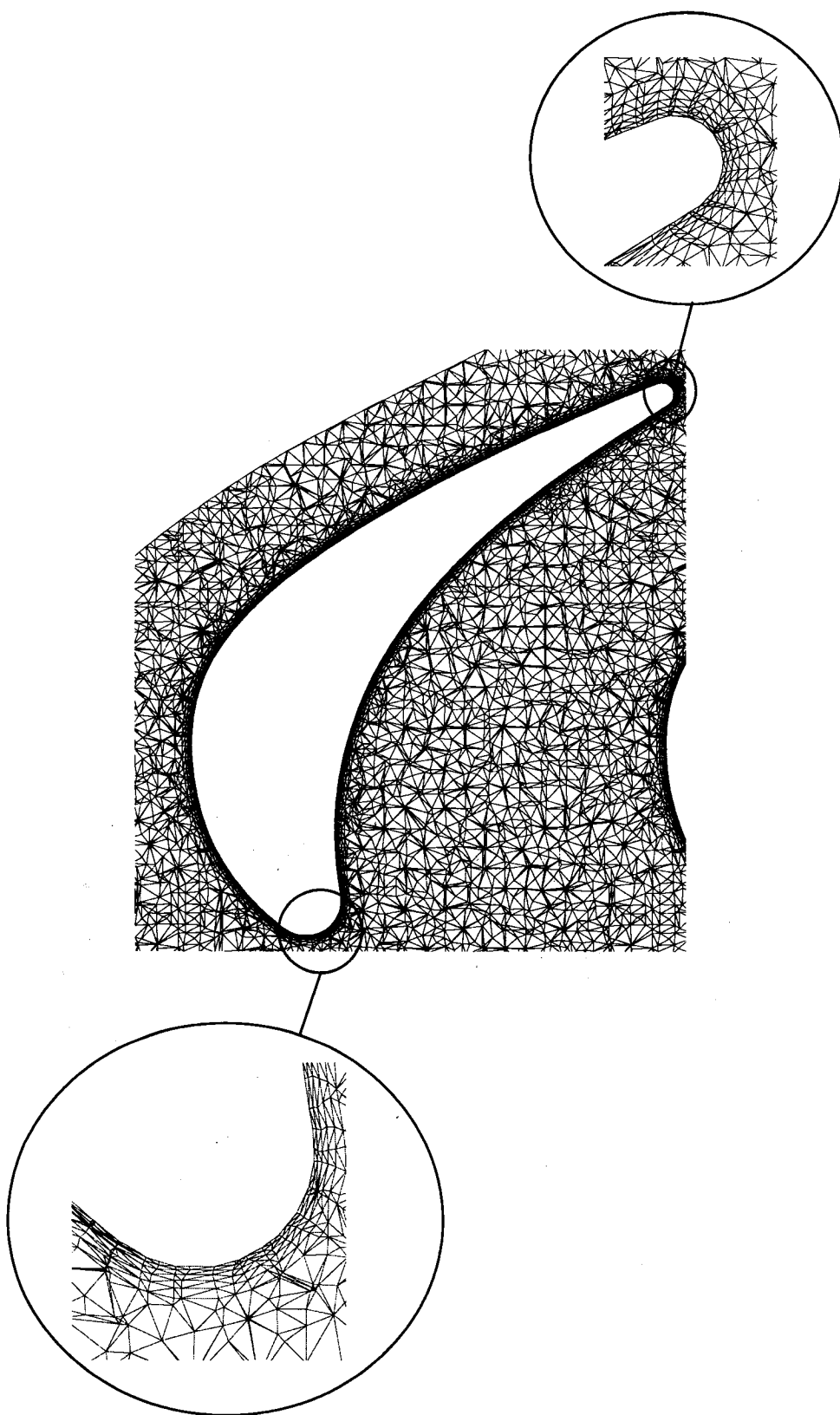
Figure 3.7 Radial cross-section of blade in rotor domain.

68
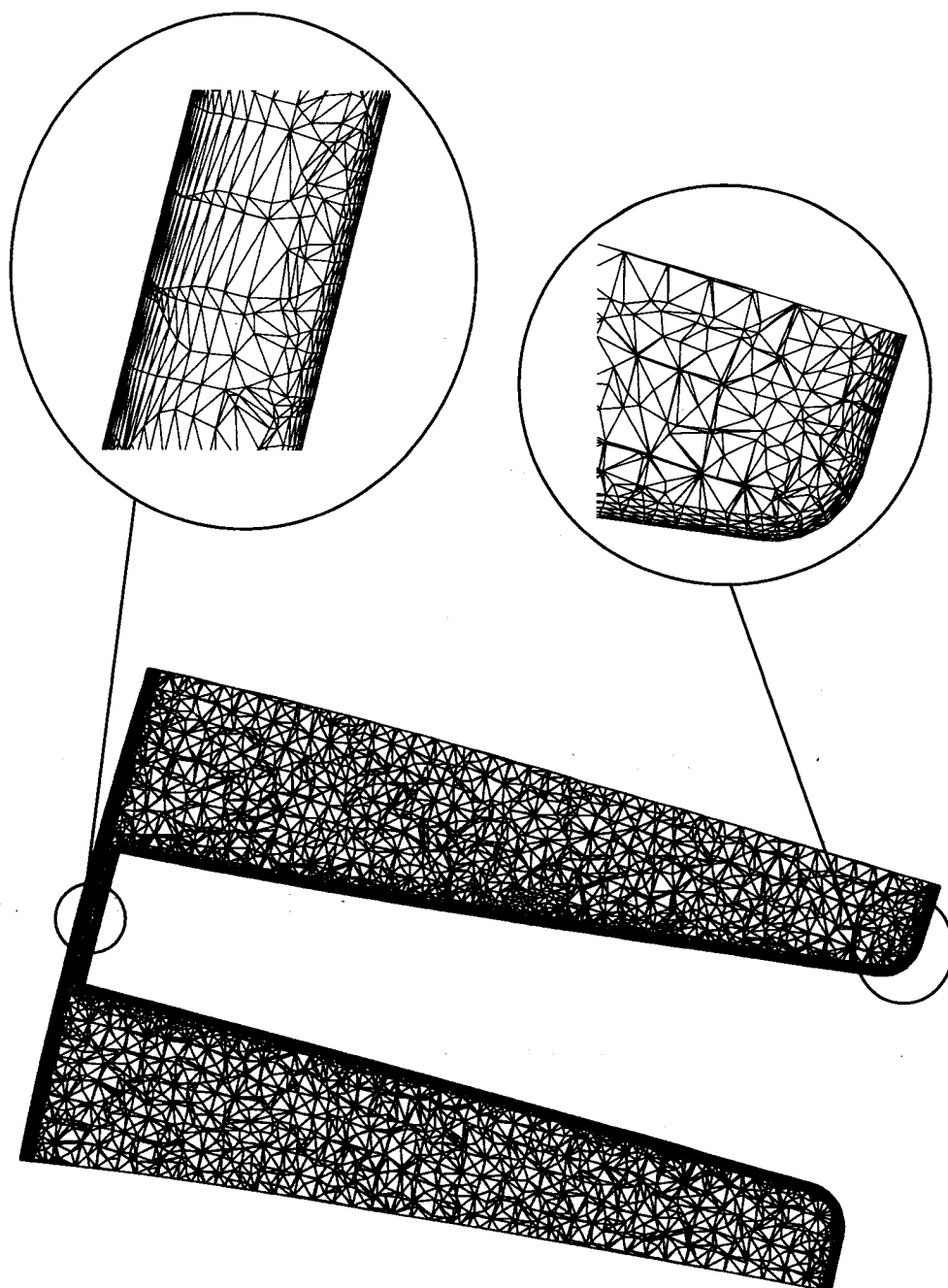
Figure 3.8 Axial cross-section of blade and tip clearance in the rotor domain.

69

prism layers were placed on the shroud in order to resolve the tip gap region as best as possible. Once completed, the mesh was exported in a format that could be read by the commercial computational fluid dynamics (CFD) solver called FLUENT, which uses a control volume based technique to discretize the continuity, momentum, and energy equations.

Constant wall temperatures were given at all walls, so that the heat flux and heat transfer coefficients could be obtained as outputs from the simulations. For the mixing plane approach, only one vane and one blade were modeled. The outlet of the vane domain was specified as the upstream side of the mixing plane, while the inlet of the rotor domain was considered as the downstream side of the mixing plane. For the frozen rotor and unsteady cases, grid interfaces, comprising of the vane domain inlet and rotor domain outlet, were used instead of a mixing plane so that all secondary flow information from the vane domain could enter the rotor domain unaltered. Thus, the grid interfaces allow fluid to move freely in between the two domains. In addition, they allow two domains to move against each other as the rotor domain rotates with a given angular velocity.

A steady frozen rotor simulation was first performed in order to obtain a suitable initial solution for the unsteady simulation. Here, the rotor domain is specified as a moving reference frame, and the amount of iterations that the frozen rotor case was allowed to run for is identical to that used in the mixing plane simulations. Once the frozen rotor solution was obtained, the rotor domain was set as a moving mesh for the unsteady simulations. The unsteady simulation was allowed to run until the static and total

70

pressures as well as mass flow rate at the grid interface and at the rotor outlet were judged to be time-periodic. Once the unsteady solution was considered to be time periodic, all unsteady flow and heat transfer data was then recorded on the shroud.

Chapter 4

Time-Averaged Solution

In the following chapter, the time-averaged predictions of the experimental work of Chana and Jones (2003) will be used to validate the industrially-owned CFD code called Nistar. The work of Chana and Jones (2003) was chosen since the geometry of the turbine stage could be extracted and re-modeled. In addition, results for the adiabatic wall temperature on the shroud were reported by Chana and Jones (2003) and could be used to compare the adiabatic aerodynamic predictions obtained in the present work. The time-averaged results from the simulation will be presented in order to further demonstrate that the code yields realistic physical results. As mentioned previously, the time-averaged results were used as an initial solution for the unsteady simulations.

4.1. Problem Description

Chana and Jones (2003) obtained experimental data in the Isentropic Light Piston Facility (ILPF), which is a short duration wind tunnel that allows full-sized high-pressure turbine stages to be tested. The inlet total pressure and inlet total temperature were reported at 4.6×10^5 Pa and 444 K respectively, and these values were used to apply constant pressure and temperature profiles at the inlet of the vane domain. At the outlet, Chana and Jones specified static pressure readings at the rotor exit at both the hub and casing, which were 1.428×10^5 Pa and 1.435×10^5 Pa respectively, and these values were used as the extremities of a linear pressure profile at the outlet of the rotor domain. Finally, the

rotor speed was set at 9500 rpm in Chana and Jones's work.

It is important to note that the turbine stage geometry of Chana and Jones (2003) has been assumed in the present study. In Chana and Jones's work, a stator with 32 vanes was used, while the rotor consisted of 60 blades. In the present study, the geometry has been scaled so that 30 vanes and 60 blades are modeled, allowing only 1 vane and 2 blades to be used to represent the turbine stage, as opposed to modeling 8 vanes and 15 blades. The geometric model for Chana and Jones's turbine stage was obtained through inference by extracting the basic shape of the airfoils and gas-path from figures available in the open literature. Using this information, Pratt and Whitney Canada appropriately scaled the geometry to 30 vanes and generated a model that yielded comparable results to the experimental data with their in-house code. In addition, the tip clearance was not known and it was assumed to be 1.2 mm, which is the size of the gap used in a similar study by Thorpe et al. (2004). In addition, the location of the inlet and the outlet of the turbine stage were unknown and had to be assumed.

4.2 Grid Independence

Grid independence tests were first conducted before simulating the work of Chana and Jones (2003). Constant total pressure and total temperature distributions were defined at the inlet of the NGV domain, with a linear static pressure distribution at the rotor exit as described above. Four steady-state runs were performed using the exact conditions of the experimental study, but each with different grid counts. All grids consisted of a node

count of 49 with an additional 16 nodes in the tip clearance region in the radial direction. The node counts in the axial and circumferential direction were varied to determine the coarsest mesh that could be used while yielding similar results to finer meshes. The total node counts for the four cases were 313698, 534934, 657874, and 742938 nodes, respectively.

In order to show that grid independence in two different directions, the static pressure profile at the exit of the NGV (Figure 4.1) was recorded as well as the isentropic Mach number distribution on the vane airfoil suction surface at midspan (Figure 4.2). Figure 4.1 shows a linear static pressure distribution at the NGV exit, which is expected since a linear pressure distribution was defined at the outlet of the rotor exit. Figure 4.2 shows the variation of the isentropic Mach number in the axial direction on the vane airfoil suction surface. The differences in the results occur in the downstream region, which coincides with the development of the suction side wakes. It can be seen in both figures that the coarsest mesh underpredicted the results from much finer meshes, and that predictions obtained with 657874 nodes and 742938 nodes yielded similar results. Therefore, a grid count of 657874 nodes was used for all cases in the present study.

4.3 Validation of the CFD code

Predictions obtained with the Nistar were compared to experimental data to validate its
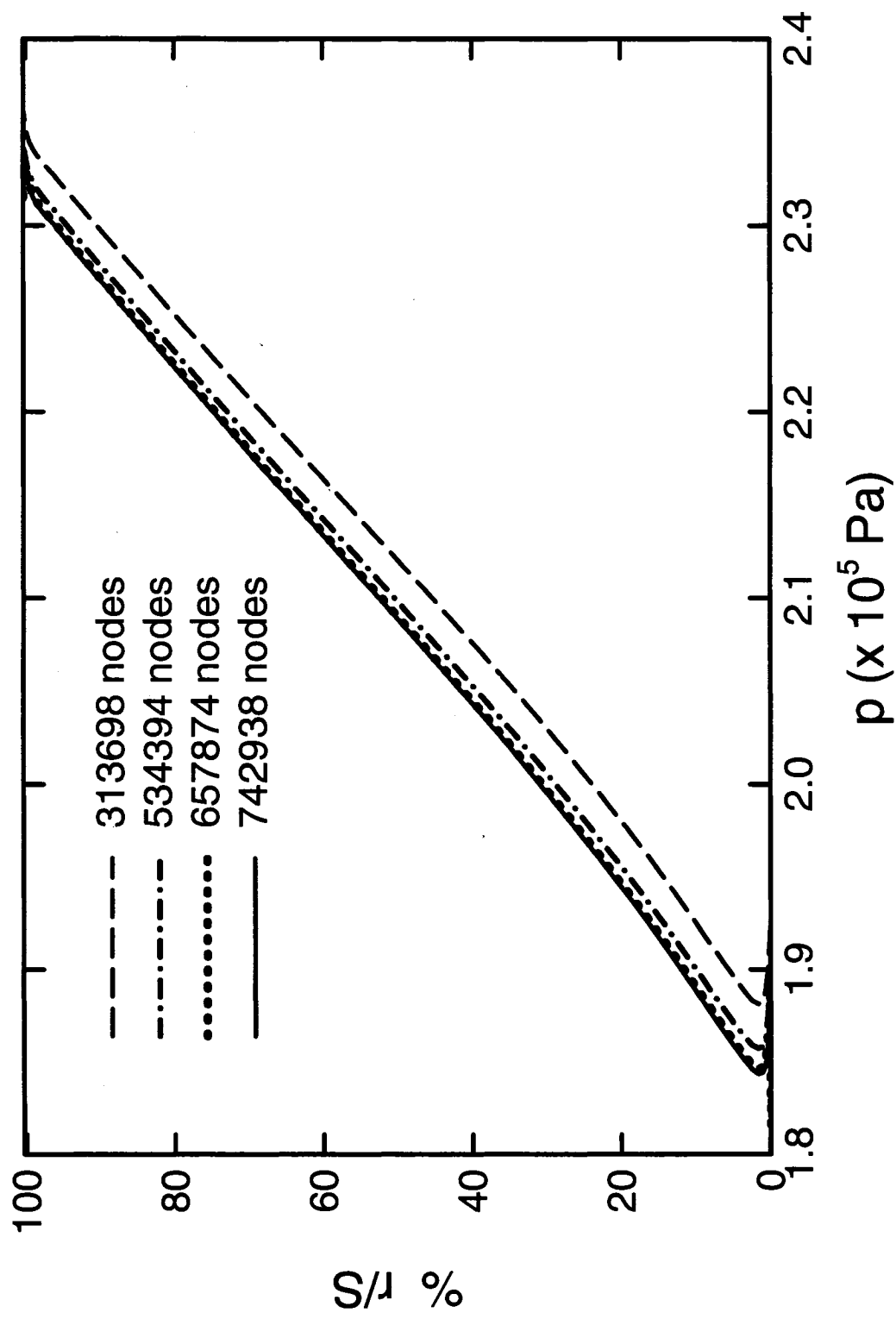
Figure 4.1 Static pressure profiles at the exit of the NGV obtained from grids with different node counts.
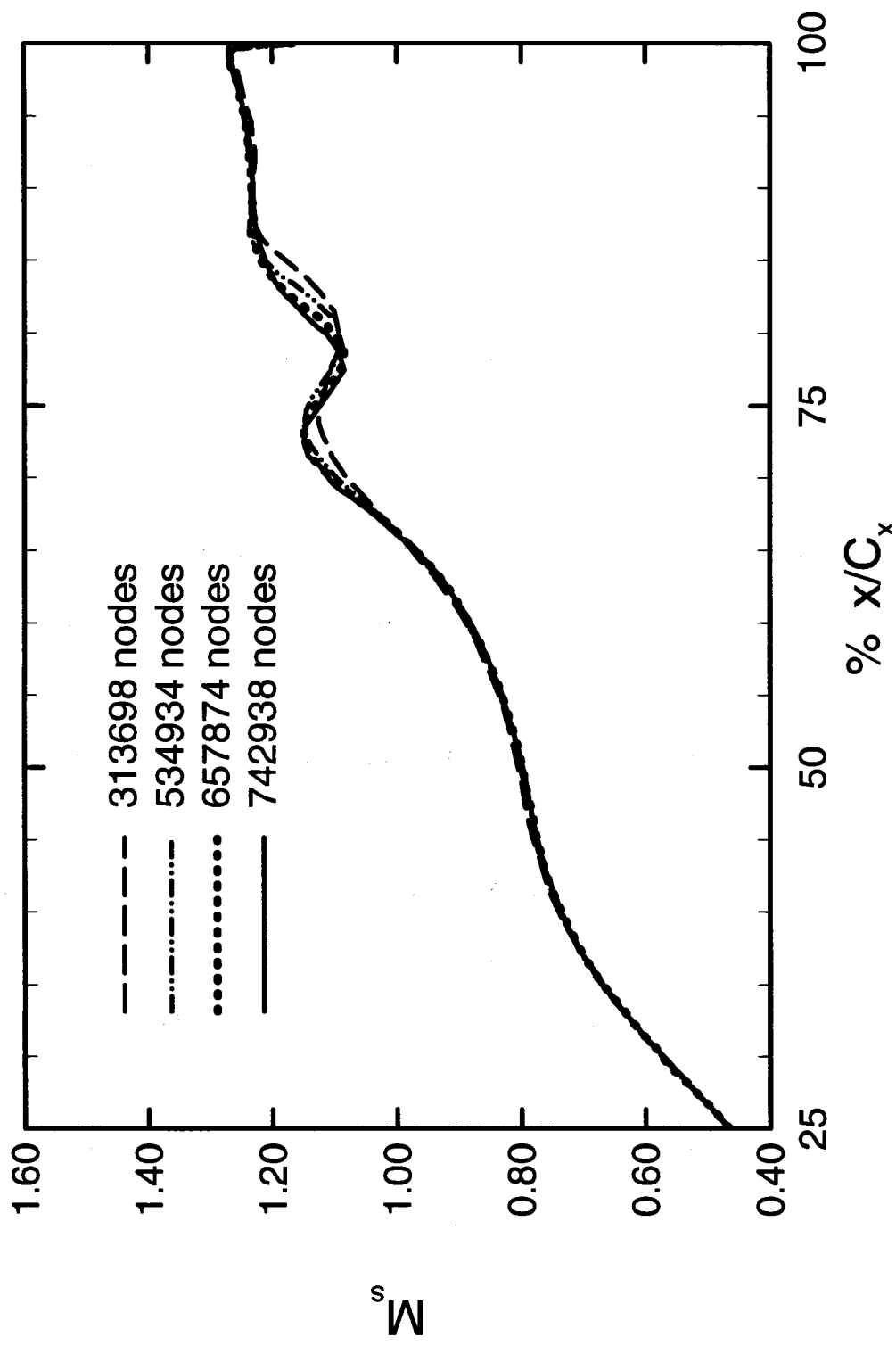
Figure 4.2 Isentropic Mach number distribution on the vane airfoil suction surface at midspan obtained from grids with different node counts.

use for the present study. The isentropic Mach numbers at both the hub and casing at the exit of the NGV are compared in Table 4.1, and show good agreement with less than 15% difference. In both cases, the value of the isentropic Mach number is higher at the hub, which is expected since the velocity at the casing is reduced due to relative motion of the shroud. The difference in the values could be due to the fact that the NGV model was scaled to 30 vanes, whereas the NGV used in Chana and Jones (2003) consisted of 32 vanes. In addition, as mentioned before, the entire geometry for the both the NGV and rotor domains was obtained through inference of the information presented in Chana and Jones (2003).

In Figure 4.3, the variation of the adiabatic wall temperature on the shroud in the axial direction was compared. The experimental data was recorded at one row of gages in the rotor passage. Since the location of the gages was unknown, circumferentially averaged data from eight planes in the circumferential direction was obtained from the simulation results and used for comparison. The prediction is in very good agreement with the experimental data. Since there is no heat transfer in the simulation, the drop in the temperature in the axial direction is evident of the work extraction across the rotor. At the leading edge of the shroud, the total temperature is equal to 444 K, which is expected since there is no work extraction across the NGV since the domain is stationary. The amount of drop in the temperature is very comparable to the experimental data, which shows that the Nistar is capable of simulating the work of Chana and Jones (2003) well.

Convergence for the time-averaged simulations were determined by the mass flow rate,

Table 4.1 Comparison of the exit isentropic Mach numbers at the NGV exit for Chana and Jones (2003) and the time-averaged solutions.

Study	Description	NGV exit isentropic Mach number
Chana and Jones (2003)	Hub	1.034
	Casing	0.925
Nistar	Hub	1.191
	Casing	1.010
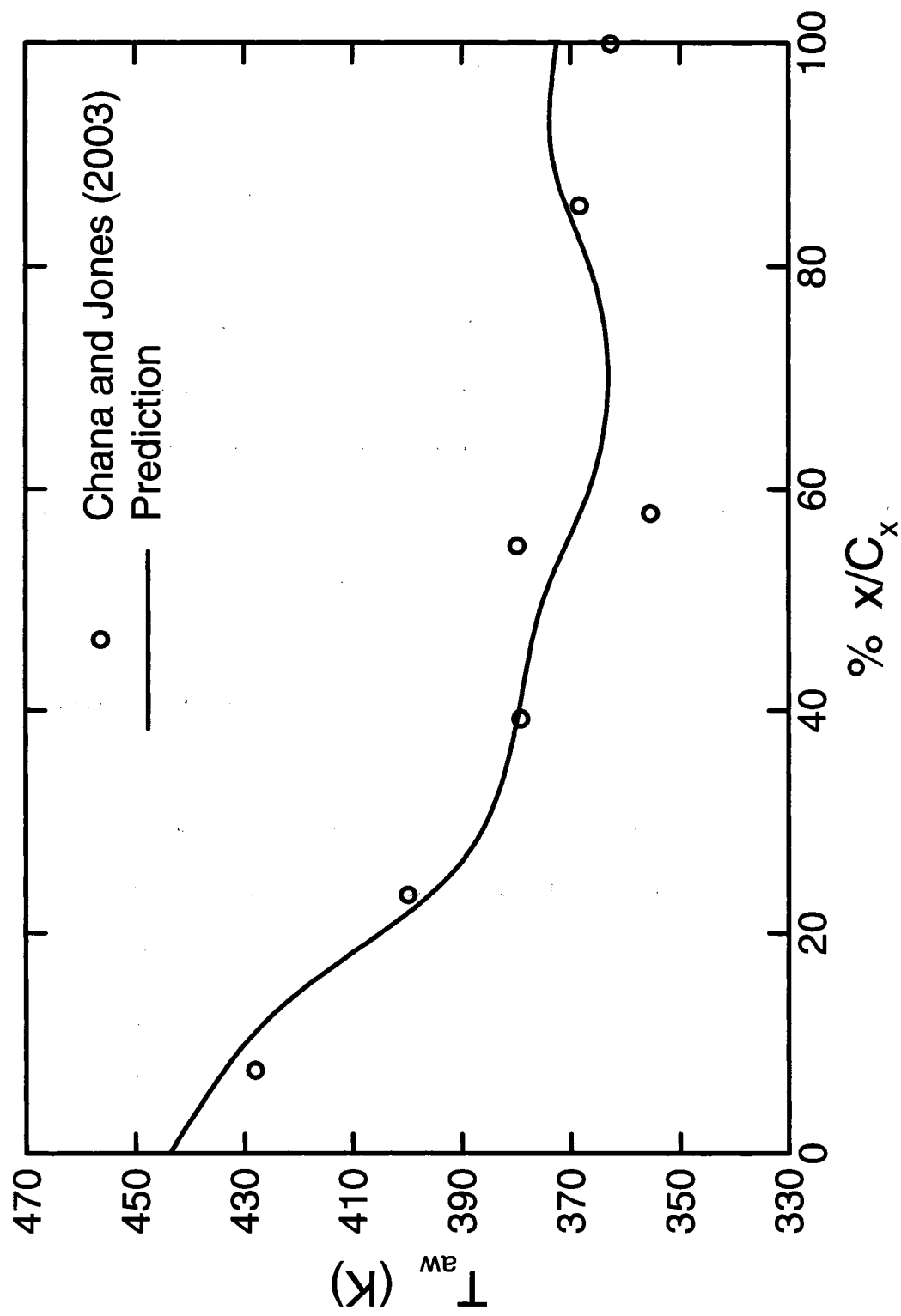
Figure 4.3 Comparison of the circumferentially averaged adiabatic wall temperature variation on the shroud in the axial direction.

total pressure, static pressure, and total temperature at the NGV and rotor inlets and exits, shown in Figure 4.4. It should be noted that all parameters, except the mass flow rates, are the mass-averaged values. As mentioned before, the steady-state cases were run for 5000 iterations, and it can be seen that the physical properties have converged to a single value after this amount of iterations. A summary of the final steady state values for these parameters are given in Table 4.2, and it is most important to note the values make physical sense. It can be seen that the mass flow rate is conserved from the NGV inlet to the rotor exit for both simulations. In addition, there is an evident drop in the stagnation pressure and temperature across the rotor, which is due to the turbine expansion process and the extraction of kinetic energy from the fluid. On the other hand, there is very little drop in the total pressure across the NGV, which is expected since there is no work being extracted here. However, there is a drop in the static pressure since the subsonic flow is being accelerated through the NGV as it guided smoothly to the rotor. Consequently, the flow is expanded across the NGV as well.

Therefore, it was concluded that Nistar was appropriate for modeling Chana and Jones's turbine stage since the predictions agreed well with the experimental data. In addition, the behavior of the physical properties makes sense, and as a result, the time-averaged results were analyzed in order to study the time-averaged behavior of the tip leakage flow in the shroud region. Note that the results in the rotor domain are considered in the rotating reference frame.
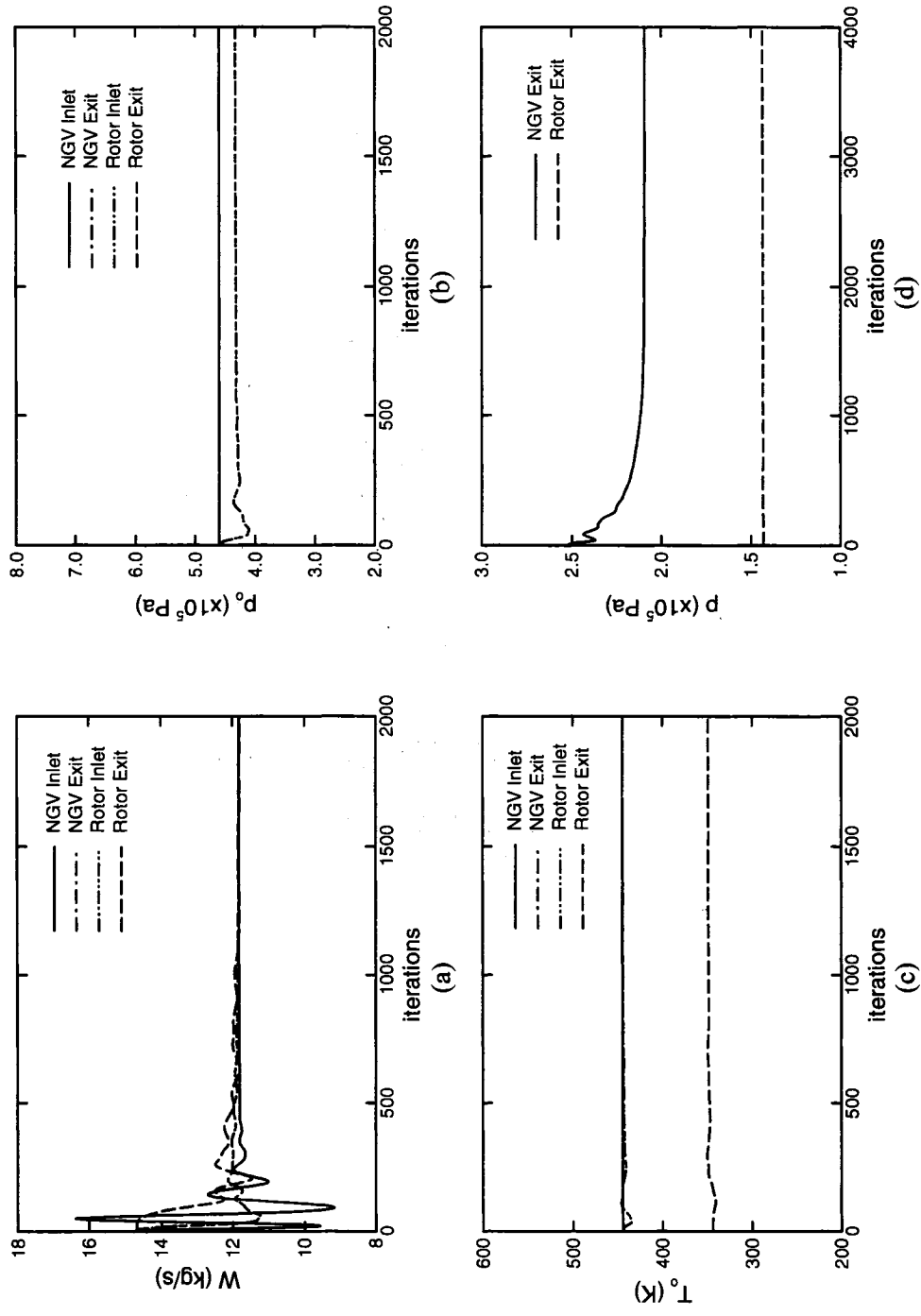
Figure 4.4 Convergence of the a) mass flow rate, b) stagnation pressure, c) stagnation temperature, and d) static pressure for the steady simulation of the baseline case.

Table 4.2 Steady-state values for the convergence parameters for the baseline case.

Location	Parameter	Final Steady-State Value
NGV Inlet	$\dot{m}$ (kg/s)	11.810
	p_o ($\times 10^5$ Pa)	4.599[*]
	T_o (K)	444.294[*]
NGV Exit	$\dot{m}$ (kg/s)	11.816
	p_o ($\times 10^5$ Pa)	4.329
	p ($\times 10^5$ Pa)	2.094
	T_o (K)	444.322
Rotor Inlet	$\dot{m}$ (kg/s)	11.815
	p_o ($\times 10^5$ Pa)	4.329
	T_o (K)	444.322
Rotor Exit	$\dot{m}$ (kg/s)	11.793
	p_o ($\times 10^5$ Pa)	1.646
	p ($\times 10^5$ Pa)	1.434[*]
	T_o (K)	348.542

4.4 Time-Averaged Results

Figure 4.5 shows the pressure contours in the tip clearance region at approximately $x/C_x = 48\%$ (I-plane = 36 in the tip clearance region). The separation bubble is evident at the pressure side of the blade tip, which develops as the flow enters the tip leakage region. Downstream of the separation bubble, a region of high pressure was observed and indicates where the extremity of the separation bubble meets with the main leakage flow at the blade tip. The flow in the separation bubble is moving towards the pressure side, while the main leakage flow is moving towards the suction side. As a result, a region of very low velocity or high static pressure forms at the blade tip. In addition, it can be seen that the static pressure at the shroud decreases near the leading edge from the pressure side to the suction side, which indicates where the leakage flow is dominant. The static pressure at the shroud then increases further downstream, showing that the effect of the relative motion of the shroud, moving from the suction surface to the pressure surface of the blade, is dominant beyond this point. The cross-flow from the adjacent rotor passage also contributes to the leftward moving flow at the shroud. There is a pressure difference across the rotor passage from the pressure side of one blade to suction side of the adjacent blade, which causes cross-flow to occur. In addition, a small re-circulation zone develops at the suction side blade tip and was attributed to the downward motion of the leakage flow interacting with the cross-flow from the adjacent blade passage.

The relative x-, y-, and z- velocity profiles in the tip gap region at approximately

83
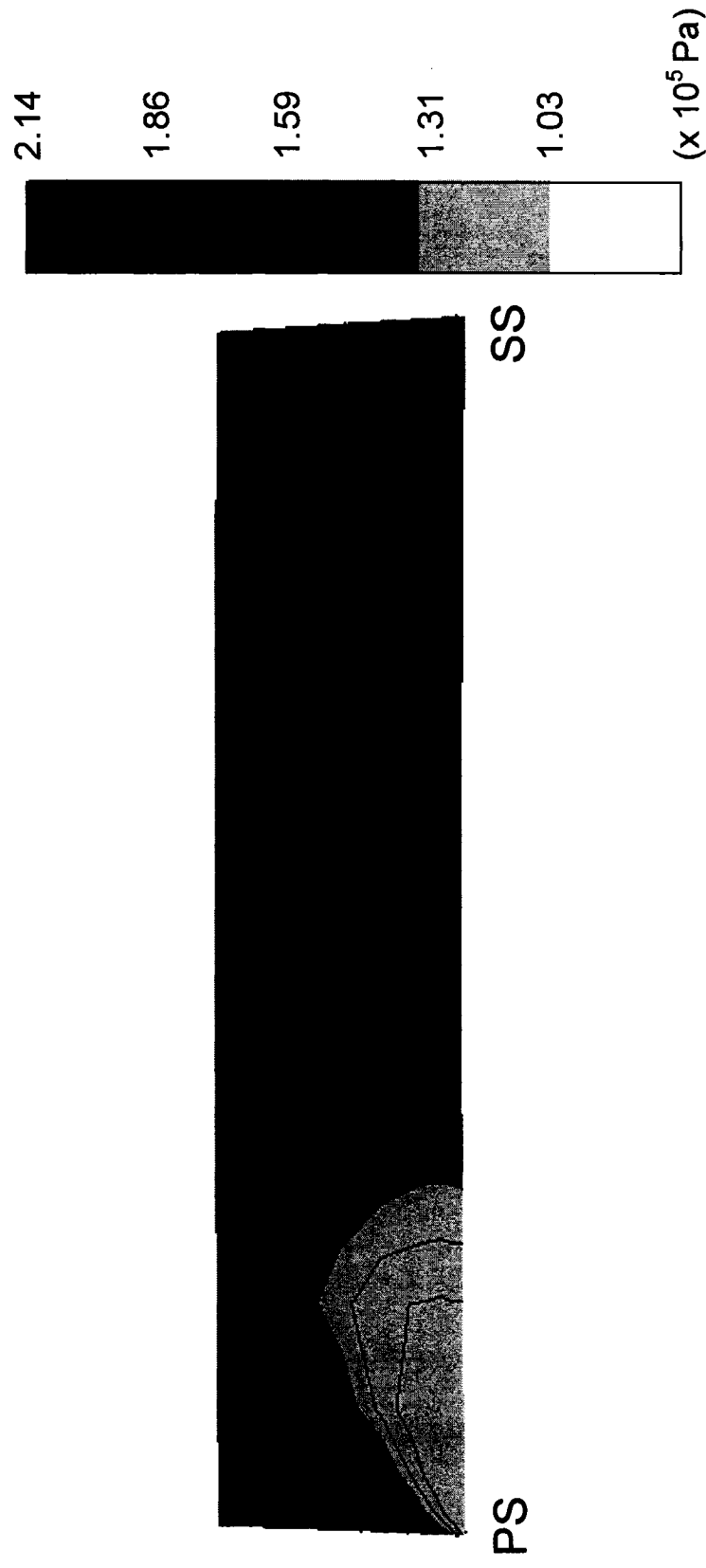
Figure 4.5 Static pressure contours in the tip clearance region at approximately $x/C_x = 48\%$ and along the camber line of the blade tip for the steady simulation of the baseline case.

$x/C_x = 48\%$ and on the camber line of the blade tip are presented in Figures 4.6, 4.7, and 4.8 respectively. The relative x-velocity shown in Figure 4.6 is in fact the axial component of the flow velocity, and an extremely steep velocity gradient can be observed at both the blade tip and shroud where the relative x-velocity is zero. The relative x-velocity at the shroud is zero is expected since the shroud's only movement is in the circumferential direction and due to no-slip boundary conditions, the flow adjacent to shroud should likewise move at the same velocity and in the same direction. A maximum of 222 m/s occurs at the middle of the gap measuring only 1.2 mm, which is extremely high for such a small space. This explains why high heat transfer rates occur in the tip gap region since the flow conditions are so extreme.

It is important to study the relative y-velocity profile in the tip gap region (Figure 4.7) since the y-direction is essentially the circumferential direction, which is the direction of the leakage flow as well as the shroud relative motion. As expected, the velocity is zero at the blade tip, and continues to increase in the radial direction due to the presence of the leakage flow. However, almost immediately, the velocity jumps to −80 m/s just above the blade tip. The negative sign indicates flow moving from the suction side to the pressure side. The relative y-velocity is negative until approximately r/h = 8% and this could represent the presence of the re-circulation surrounding the separation bubble at this location. The velocity then becomes positive from r/h = 8% to 86%, which shows the dominance of the leakage flow moving from the pressure side to the suction side of

85

Figure 4.6 Relative x-velocity profile in the tip clearance region at approximately $x/C_x = 48\%$ and on the camber line of the blade tip.

Figure 4.7 Relative *y*-velocity profile in the tip clearance region at approximately $x/C_x = 48\%$ and on the camber line of the blade tip.

Figure 4.8 Relative z-velocity profile in the tip clearance region at approximately $x/C_x = 48\%$ and on the camber line of the blade tip.

the blade tip. From r/h = 86% to 100%, the effect of the wall's relative motion becomes significant near the shroud, causing the flow velocity to change direction. As a result, a stagnation point develops where the relative y-velocity is zero at 90% r/h. This will cause a region of high pressure in the tip clearance region, rendering it susceptible to high heat transfer rates at this location.

The magnitude of the relative z-velocity is relatively small compared to its x- and y- counterparts, as shown in Figure 4.8. The direction of the radial component of relative velocity is mainly downward (negative), except near the blade tip and the shroud. The maximum absolute value is -60 m/s compared to 222 m/s and 165 m/s for the relative x- and y- velocities, respectively. The smaller magnitude makes sense since the height of the tip gap region is so small, leaving little room for the flow to be maneuvered in the radial direction. Near the blade tip, it was observed that the relative z-velocity is slightly positive or moving upwards, which indicates the presence of recirculation from the separation bubble. In addition, the relative z-velocity gradient is very steep near the shroud, and another stagnation point, where the relative z-velocity is zero, can be found at 92% r/h. This point indicates the intersection between the leakage flow and the flow caused by the relative motion of the shroud. Below 92% r/h, the flow is moving downward as the leakage flow maneuvers around the boundary layer flow from the shroud. The change in the flow direction closer to the shroud indicates the presence of the boundary layer flow, which has a slight upward motion due to its interaction with the tip leakage flow. Also, the relative z-velocity is positive near the shroud since the rotation of the shroud in the yz plane has a slight positive z-component.

89

Figure 4.9 shows the resultant relative Mach number profile in the tip clearance region at approximately $x/C_x = 48\%$ and on the camber line of the blade tip. A steep velocity gradient was observed at the blade tip, where the flow just above the blade tip is moving at a relative Mach number of 0.2 while the blade tip is at zero relative velocity. The velocity remains steady at approximately Mach 0.2 until 5% r/h, indicating the presence of the separation bubble, which prevents the development of a parabolic velocity profile. From Figure 4.8, it can be seen that the relative z-velocity is positive or upward until approximately 5% r/h, which slightly obstructs the leakage flow which has a downward motion since it must negotiate the separation bubble at the blade tip and opposing boundary layer flow at the shroud. Thus, the resultant Mach number profile shows a slight delay before developing into a parabolic shape from 5% r/h to 92% r/h. Above 92% r/h, the effect of the shroud boundary layer becomes dominant. The motion of the shroud causes the flow adjacent to it to move from the suction side to pressure side of the blade, which is in the opposite direction of the leakage flow. As a result, the relative y- and z- velocities become zero at approximately 92% r/h as can be seen in Figures 4.7 and 4.8, after which they increase once again. Also, the relative x-velocity decreases rapidly to zero from 92% r/h to 100% r/h, and so only the y- and z-velocities contribute to the resultant Mach number, which explains why the Mach number increases near the shroud.

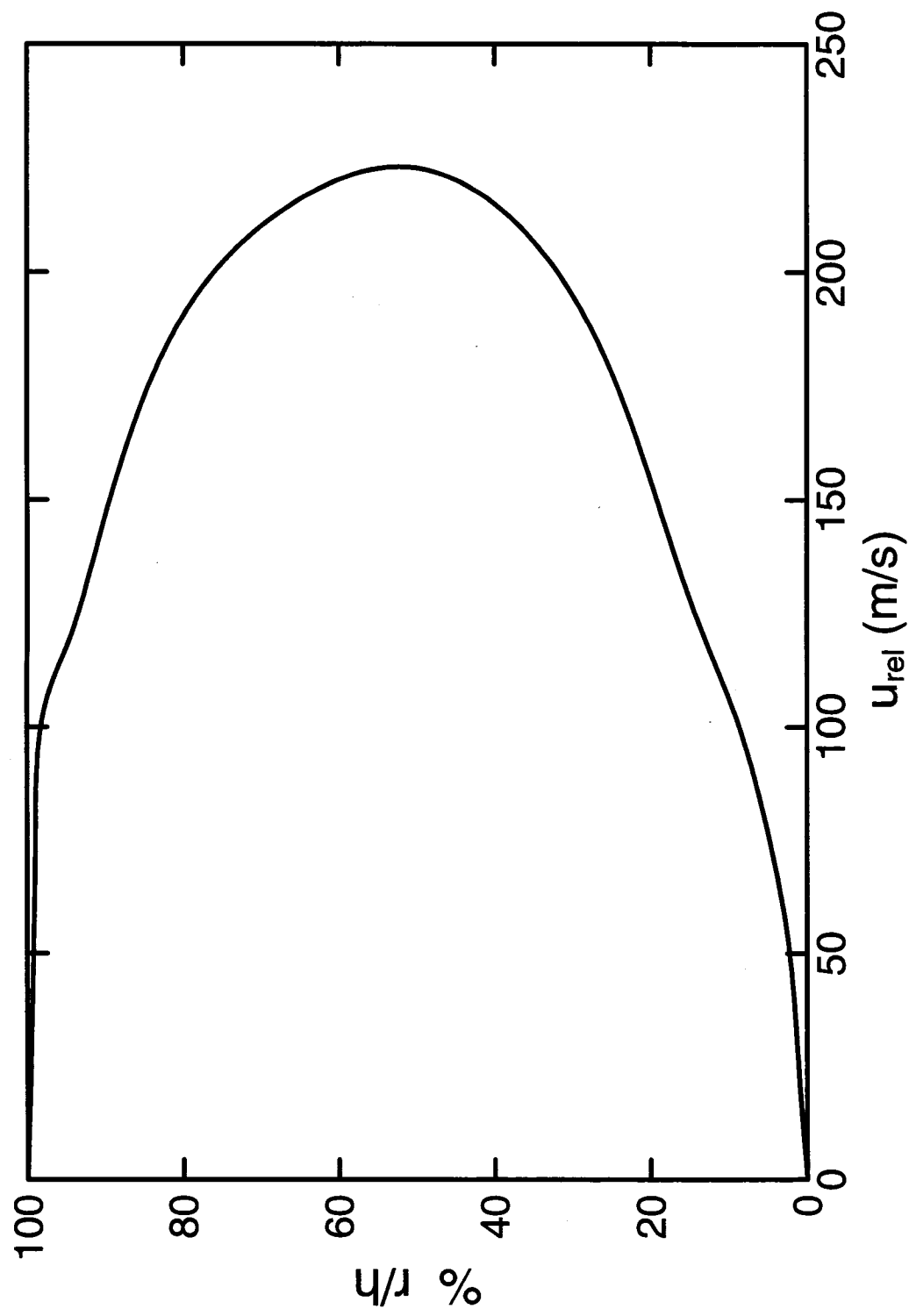Figure 4.9 Relative Mach number profile in the tip clearance region at approximately $x/C_x = 48\%$ and on the camber line of the blade tip.
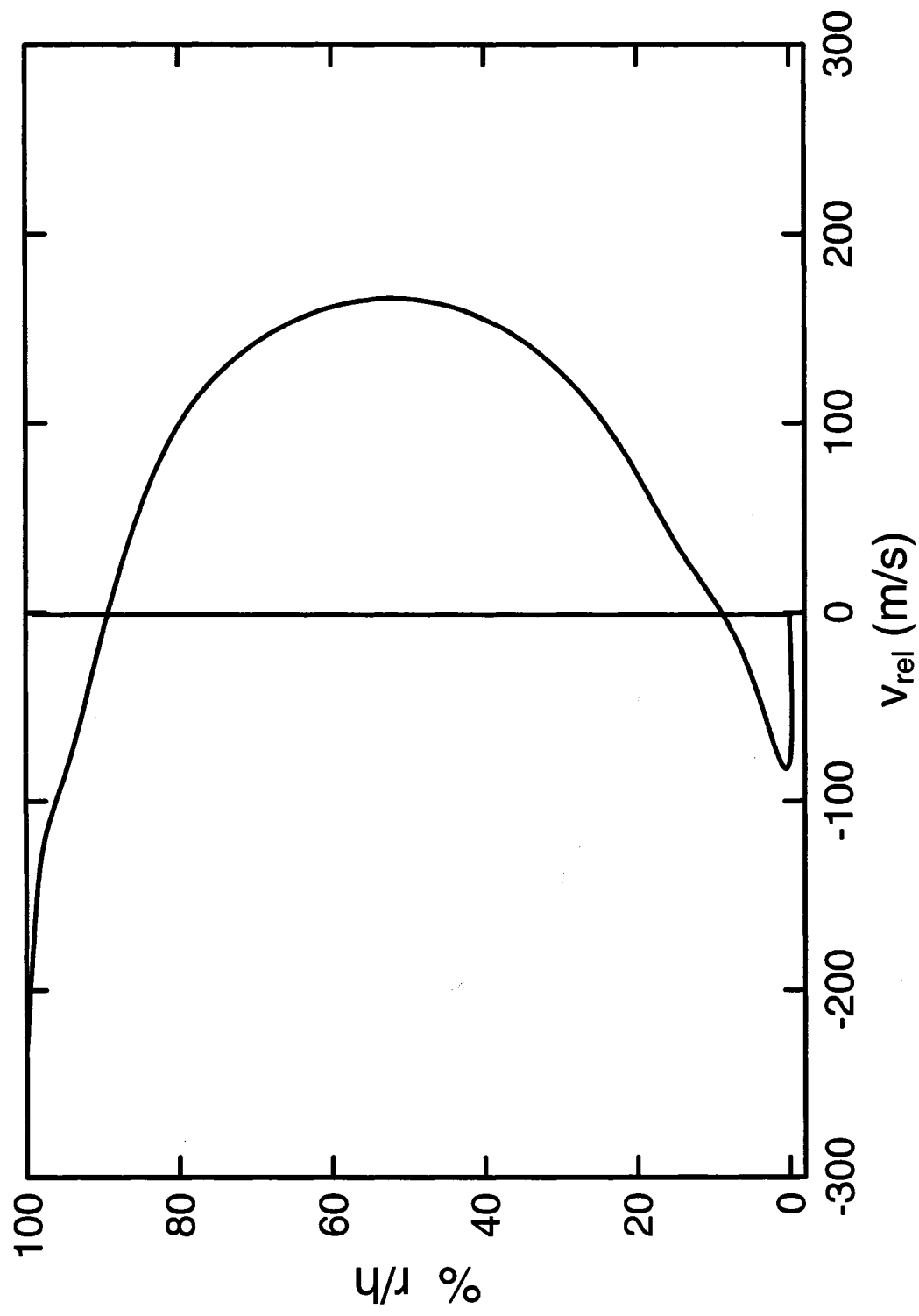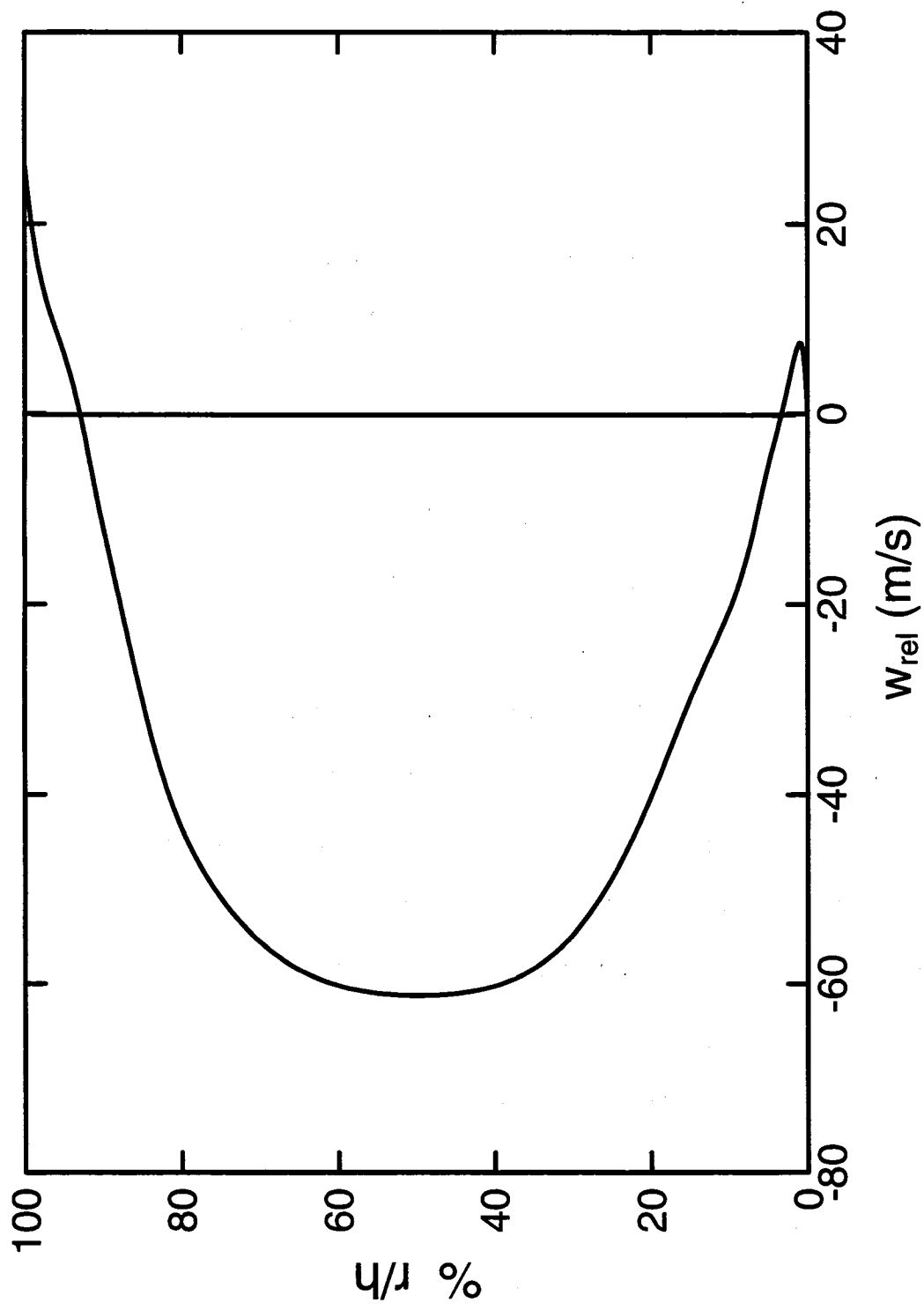
The static temperature profile in the tip clearance region at approximately $x/C_x = 48\%$ and on the camber line of the blade tip has been presented in Figure 4.10. At the blade tip, an adiabatic wall temperature of 382 K was found, while a temperature of 373 K was found at the shroud. The temperature profile follows an opposite trend as that of the relative Mach number in Figure 4.9, as expected. As the flow accelerates, the kinetic energy increases and so the static temperature must decrease due to conservation of energy. The opposite trend occurs if the flow decelerates, whereby the static temperature increases due to conservation of energy. The static temperature reaches a minimum of 346 K at the midspan of the tip clearance region (50% r/h) and increases to a maximum of 390 K at 95% r/h. The high static temperature near the shroud indicates that only a small amount of work has been extracted from the flow near the shroud. This demonstrates how leakage flow is highly undesirable since this flow is a loss, which decreases the efficiency of the engine.

Next, the flow behaviour in the axial direction will be investigated. Figure 4.11 shows the relative Mach number variation at the midspan of the clearance region along the camber line of the blade tip. Near the leading edge, the relative Mach number decreases until $x/C_x = 25\%$ and this was attributed to the presence of the separation bubble since it has been observed in previous studies that that the leakage flow enters the tip clearance region near the leading edge. From $x/C_x = 25\%$ to $x/C_x = 81\%$, the flow accelerates to a relative Mach number of 1.36 indicating that the flow is inside a re-circulation region caused by the opposing flow changing direction inside the tip clearance region midspan.

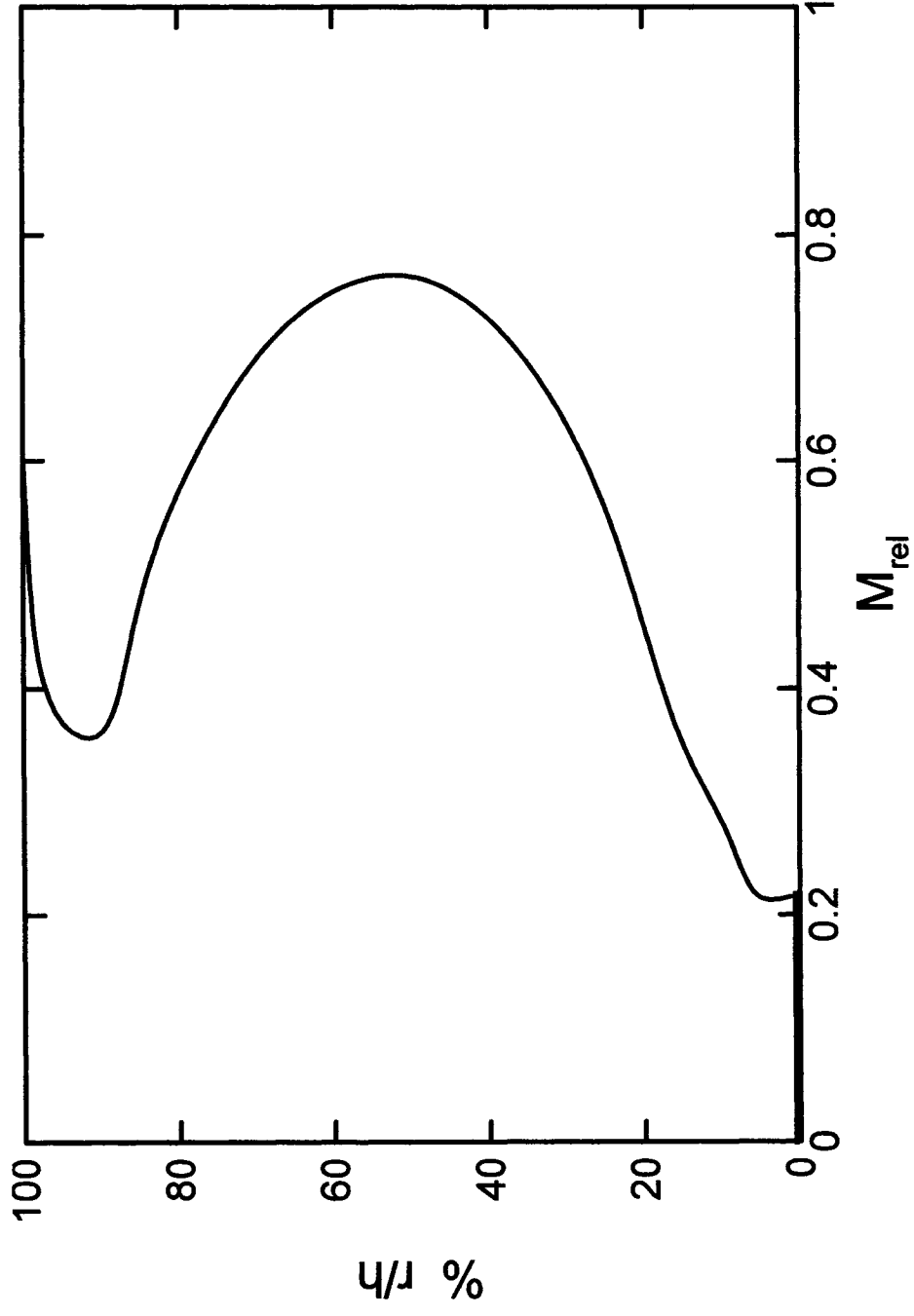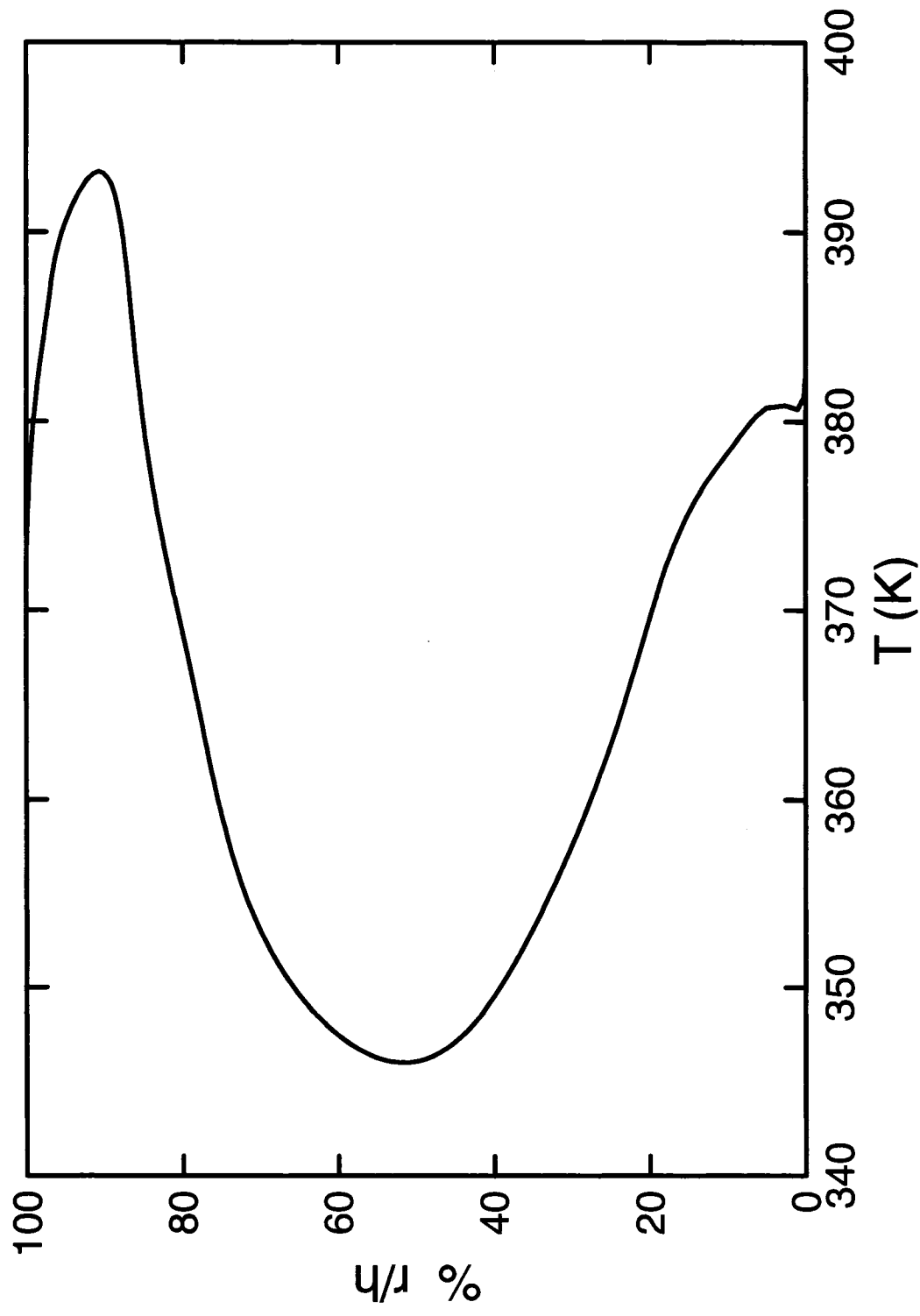Figure 4.10 Static temperature profile in the tip clearance region at approximately $x/C_x = 48\%$ and on the camber line of the blade tip.

Figure 4.11 Variation of the relative Mach number at the midspan of the tip clearance region along the camber line of the blade tip.

94

Note that in Figures 4.6 to 4.8, the magnitudes of the velocity components at $x/C_x = 48\%$ are at their maximum values at midspan. Near the trailing edge, the tip leakage flow decelerates once again, indicating that the opposing flow from the suction side is dominant as it enters the tip clearance through the suction side.

The variation of the static temperature in the axial direction at the midspan of the tip clearance region along the camber line is shown in Figure 4.12. As expected the trend is opposite to the relative Mach number distribution shown in Figure 4.11. The static temperature increases as the flow decelerates due to obstruction caused by the separationbubble. Due to conservation of energy, the velocity is decreasing and so the kinetic energy is transformed into internal energy thus increasing the static temperature. Once the leakage flow negotiates around the separation bubble at $x/C_x = 21\%$, it is able to accelerate until $x/C_x = 81\%$ thus decreasing the temperature of the flow as energy is transformed into kinetic energy. At the trailing edge, the leakage flow decelerates once again as it meets the opposing secondary cross flow from the adjacent blade passage. The deceleration causes the internal energy to increase, thus raising static temperature near the trailing edge.

Figure 4.13 shows the mass flow rate entering the tip clearance region through the pressure side and exiting through the suction side at midspan. For the pressure side curve, positive mass flow rates indicate flow entering the tip clearance region. For the suction side curve, negative mass flow rates represent flow exiting the tip clearance

95

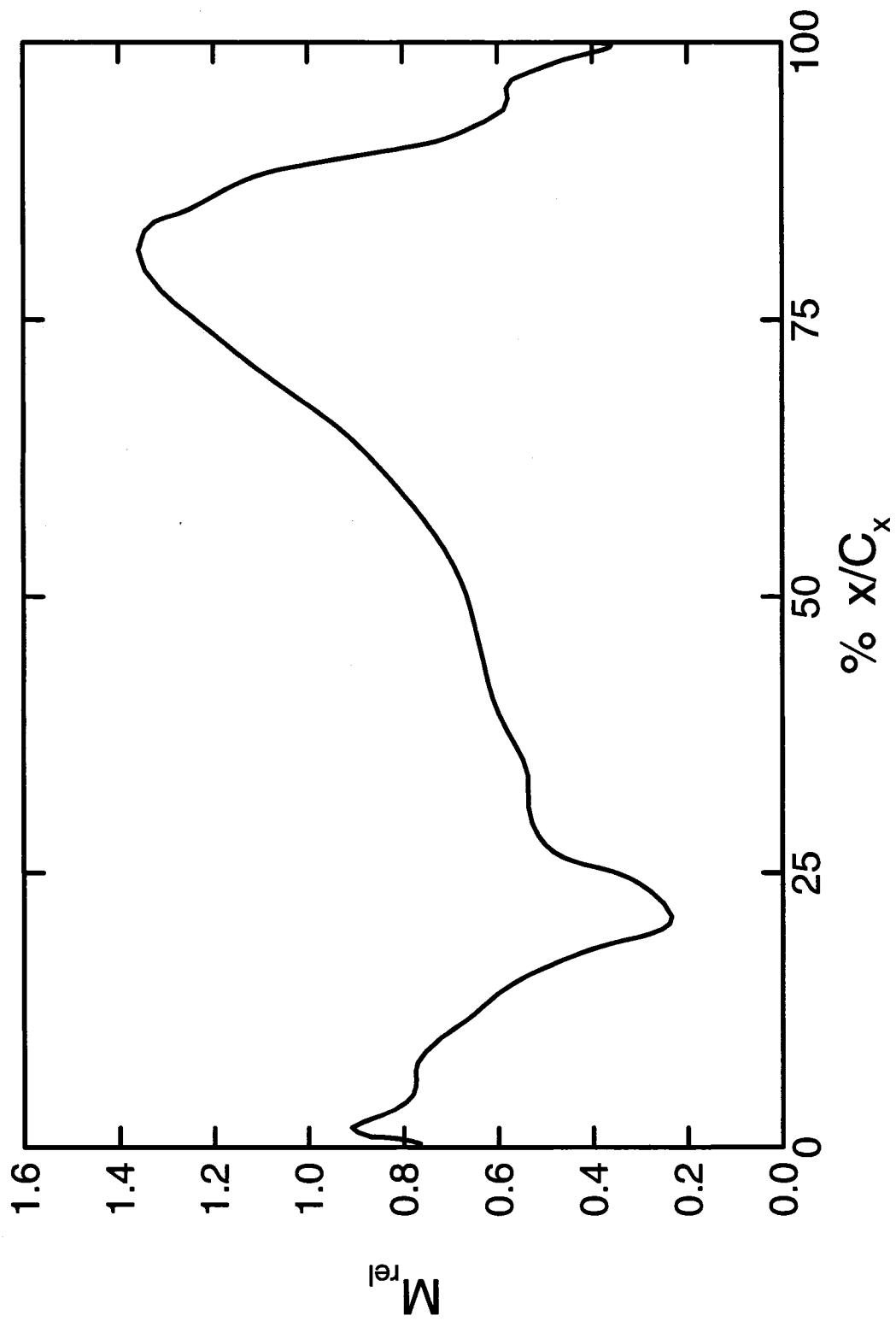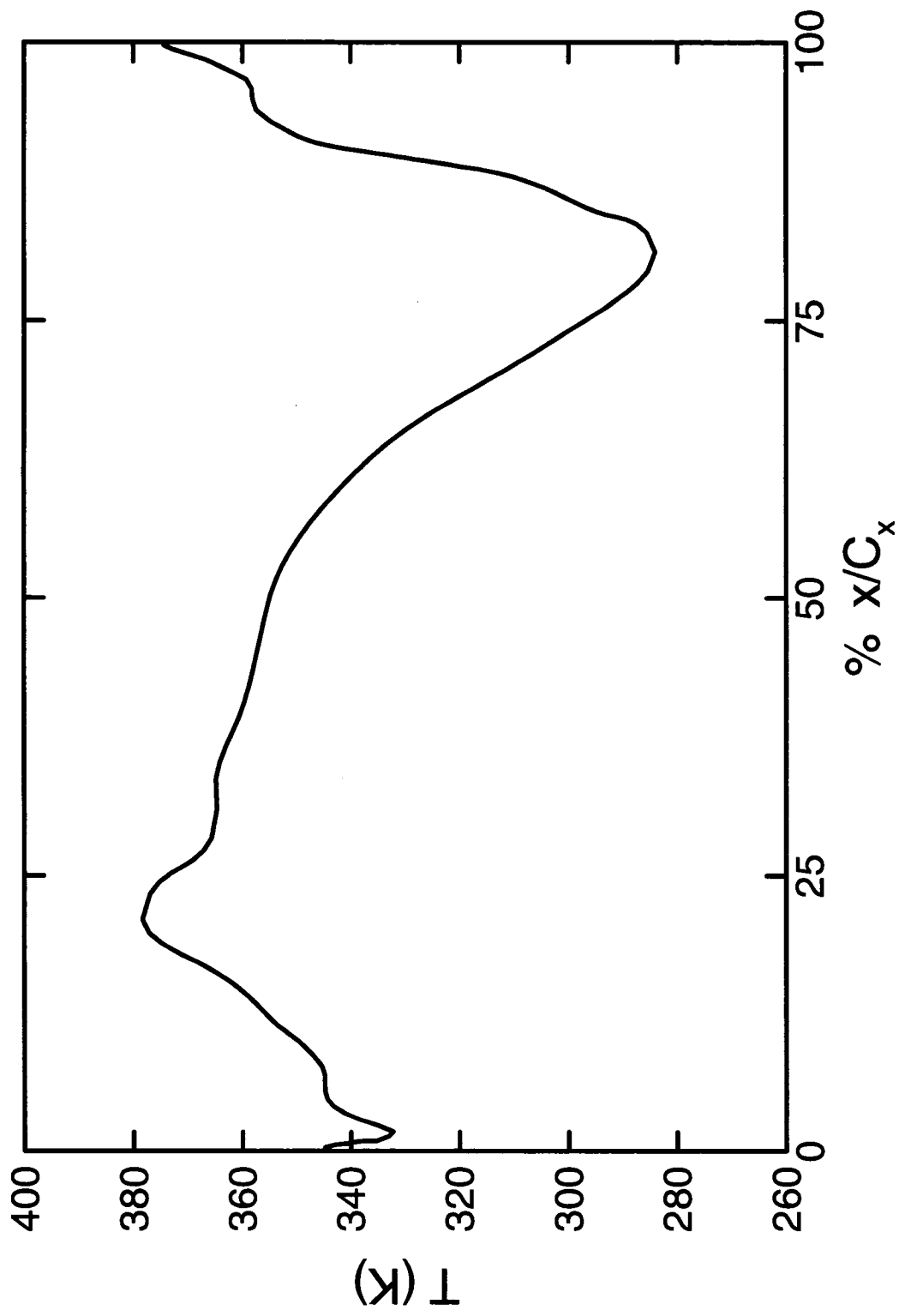Figure 4.12 Variation of the relative static temperature at the midspan of the tip clearance region along the camber line of the blade.
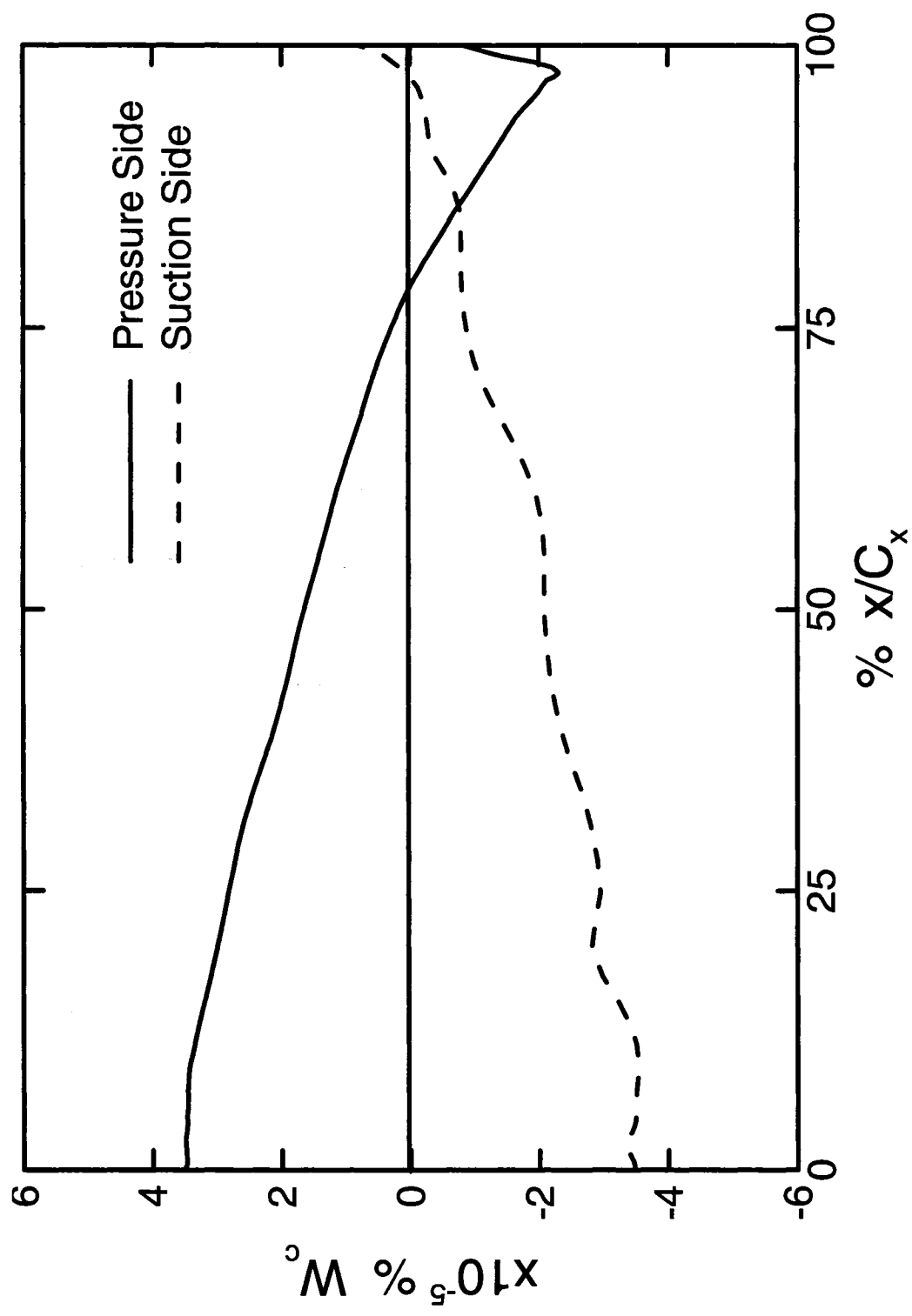
Figure 4.13 Comparison of mass flow rates at the pressure side and suction sides of the tip clearance region at midspan.

97

region. It can be seen from this curve that the mass flow entering and exiting the tip leakage region is nearly identical at each axial location up until $x/C_x = 50\%$. After which, more mass flow appears to be leaving than entering at a particular axial location. This is due to the fact that, further downstream, the leakage flow does not cross over the blade tip at an angle perpendicular to the axial direction. Instead, the flow enters at an angle, which depends on the shape of the airfoil and flow conditions. It can be seen from Figure 4.13 that most of the leakage flow enters the tip clearance region at the leading edge, as expected. A maximum flow rate of 3.49×10^{-5} $\% W_c$ enters and leaves the tip clearance region at the leading edge. Leakage flow continues to enter until $x/C_x = 77\%$, after which flow exits at both the suction side and pressure side. This is due to the interaction of the leakage flow with the secondary cross flow causing the flow to wrap up into a recirculation zone near the trailing edge. The flow rotates in a plane parallel to the blade tip, and near the trailing edge the airfoil thickness is small. As a result, the rotating flow will exit through both the pressure side and suction side near the trailing edge.

In order to examine the effect of the leakage flow on the shroud, the static pressure and adiabatic wall temperature contours have been presented in Figures 4.14 and 4.15. The static pressure and adiabatic wall temperature on the shroud reflect the flow behavior, which has been described throughout this chapter. From the pressure contours it can be seen that there is a low-pressure region near the trailing edge in the tip clearance region. This is indicative of the re-circulation region mentioned above, which develops due to the

2.14
1.78
1.41
1.05
0.69

$(\times 10^5 \text{ Pa})$
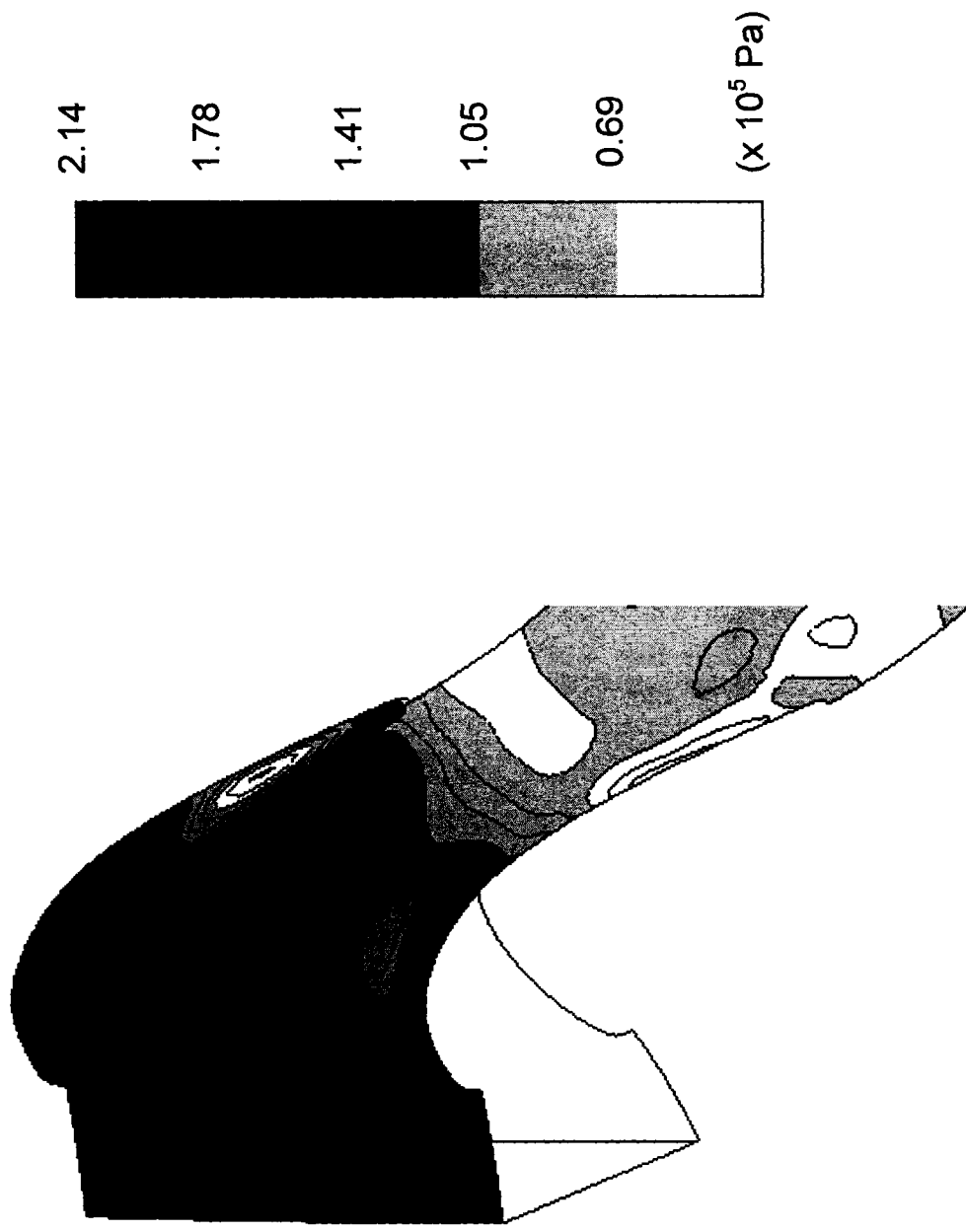
Figure 4.14 Static pressure contours on the shroud for the steady simulation of the baseline case.

444.00

413.89

383.33

352.78

322.22

(K)

Figure 4.15   Adiabatic wall temperature contours on the shroud for the steady simulation of the baseline case.

100

interaction of the tip leakage flow with the secondary cross flow. In the rotor passage area, a pressure gradient can be observed spanning from the pressure side of the airfoil to the suction side of the adjacent blade at the throat area, which is the smallest area of the converging-diverging nozzle. As a result of this pressure gradient, secondary cross flow develops which moves from the pressure side of the airfoil to the suction side of the adjacent blade. However, a high-pressure region was found near the suction side at the throat area, and was attributed to the interaction of the tip leakage flow with the secondary cross flow. As a result, another small recirculation zone appears in the rotor passage.

From Figure 4.15, it can be seen that at the inlet of the shroud, the adiabatic wall temperature is nearly equal to the total temperature of the turbine stage. This is expected since no work has been extracted from the NGV. High adiabatic wall temperatures were observed at the leading edge of the blade tip. These high temperatures occur due to the flow deceleration that occurs as the flow from the vane strikes the blade tip leading edge. In the tip clearance region, the adiabatic wall temperature decreases from the leading edge to the trailing edge, indicating that work is being extracted from the rotor. In the rotor passage area, the adiabatic wall temperature decreases in the circumferential direction along the throat area from the pressure side of the airfoil to the suction side of the adjacent blade. A region of low adiabatic wall temperature develops in the passage area, which coincides with the re-circulation zone mentioned above. The kinetic energy in the re-circulation zone increases, which decreases the internal energy of the flow due to conservation of energy.

Chapter 5

Time-Accurate Solution

As observed from the rotating reference frame, the flow behaviour inside the tip clearance region is time dependent due to the periodic passing of the vanes. In this chapter, time-dependent simulations will be performed in order to investigate the effect of the tip clearance height, the inlet turbulence intensity, the inlet stagnation temperature, and the rotor angular velocity on the unsteady tip clearance flow behavior. The work of Chana and Jones (2003), described in the previous chapter, will serve as the baseline case to which the results will be compared. In addition, the trials of using a commercial CFD package to obtain time-accurate heat transfer calculations on the shroud will be presented.

5.1 Problem Description

Time-accurate simulations require a huge number of computer resources. For the unsteady cases, one vane passage and two blade passages were modeled so that both the NGV and rotor domains are of equal pitch. This allows information to be transmitted appropriately through the interface during the unsteady simulation. In this case, Nistar makes an exact copy the blade mesh used in the steady-state simulations, which significantly increases the size of the entire computational domain. The time step was chosen such that 200 time steps are required for one vane passing period. In addition, 10 inner iterations were used for each time step calculation.

Since data is recorded in the rotating reference frame, the time periodicity of the results should be equal to the time between consecutive vane passings or the vane passing periods. The time-accurate results have been presented at four different times normalized by the vane passing period. The non-dimensional time variable, t^*, is defined as follows:

$$t^* = \frac{t}{\Theta_{vane}},$$ (5.1)

where Θ_{vane} is the vane passing period obtained from

$$\Theta_{vane} = \frac{\theta_{vane}}{\Omega}.$$ (5.2)

Here, θ_{vane} represents the vane angular pitch and Ω is the rotor angular velocity.

It is also important to note that the shroud is stationary in the absolute reference frame. However, the results obtained in the present study are in the rotating reference frame, and since there is no post-processor for Nistar, it was not possible to obtain time-accurate results of the shroud as seen from the absolute reference frame. Thus, the results for the shroud were recorded at the K-plane just below the shroud, and are thus still in the rotor reference frame. Since the heat transfer to the shroud is determined by the flow physics and temperature just below the shroud, this information is still useful for understanding heat transfer mechanisms to the shroud.

5.1.1 Test Matrix

For the unsteady investigation, a total of eight cases were simulated as shown in the test

103

Table 5.1 Test matrix for the unsteady parametric investigation.

Parameter	Case Number	h, mm	I, %	T_o, K	Ω, rpm
Effect of tip clearance height, h	Baseline	1.2	3	444	9500
	1	0.6			
	2	2.0			
Effect of vane inlet turbulence intensity, I	3	1.2	0.5		
Effect of inlet stagnation temperature, T_o	4	1.2	3	600	
	5			800	
Effect of rotor angular velocity, Ω	6			444	7500
	7				11500

matrix (Table 5.1). The test parameters were chosen such that significant differences from the baseline results could be observed. In Case 1, a tip clearance of $h = 0.6$ mm was chosen since tip clearances are usually smaller than 1.2 mm. In addition, a tip clearance of 2.0 mm was chosen in Case 2 in order to study the effect of larger tip clearances. The inlet turbulence intensity is defined as $I = u'/U_\infty$, and an intensity of 0.5% was chosen for Case 3. This value is quite low, but previous studies (eg., Radomsky and Thole, 2000) have also used similar values in order to study secondary flow in gas turbines. Higher inlet stagnation temperatures of $T_O = 600\ K$ and $T_O = 600\ K$ were used in Cases 4 and 5 since it is desirable to increase the inlet turbine temperatures in order to improve efficiency of the engine. Finally, angular velocities of $\Omega = 7500$ rpm and $\Omega = 11\ 500$ rpm were chosen in Cases 6 and 7 in order to study the effect of rotor angular velocity.

5.1.2 Convergence of Time-Averaged Solutions

As mentioned before, an appropriate steady-state or time-averaged solution must be used as an initial solution for the unsteady simulations. Therefore, for all cases, steady-state \mixing plane simulations were performed until the mass flow rates, the stagnation pressures, and the stagnation temperatures, at the inlets and outlets of both the NGV domain and rotor domain reached convergence. In addition, the static pressures at outlets of the domains were recorded. Once again all parameters, except the mass flow rates, are the mass-averaged values. The baseline convergence for the time-averaged solution was presented in Figure 4.4, while those for all other cases are presented in Figures 5.1 to 5.7.

105

Figure 5.1 Convergence of the a) mass flow rate, b) stagnation pressure, c) stagnation temperature, and d) static pressure for the steady simulation of Case 1.

106

Figure 5.2 Convergence of the a) mass flow rate, b) stagnation pressure, c) stagnation temperature, and d) static pressure for the steady simulation of Case 2.

107

Figure 5.3 Convergence of the a) mass flow rate, b) stagnation pressure, c) stagnation temperature, and d) static pressure for the steady simulation of Case 3.

108

Figure 5.4 Convergence of the a) mass flow rate, b) stagnation pressure, c) stagnation temperature, and d) static pressure for the steady simulation of Case 4.

109

Figure 5.5 Convergence of the a) mass flow rate, b) stagnation pressure, c) stagnation temperature, and d) static pressure for the steady simulation of Case 5.

110

Figure 5.6 Convergence of the a) mass flow rate, b) stagnation pressure, c) stagnation temperature, and d) static pressure for the steady simulation of Case 6.
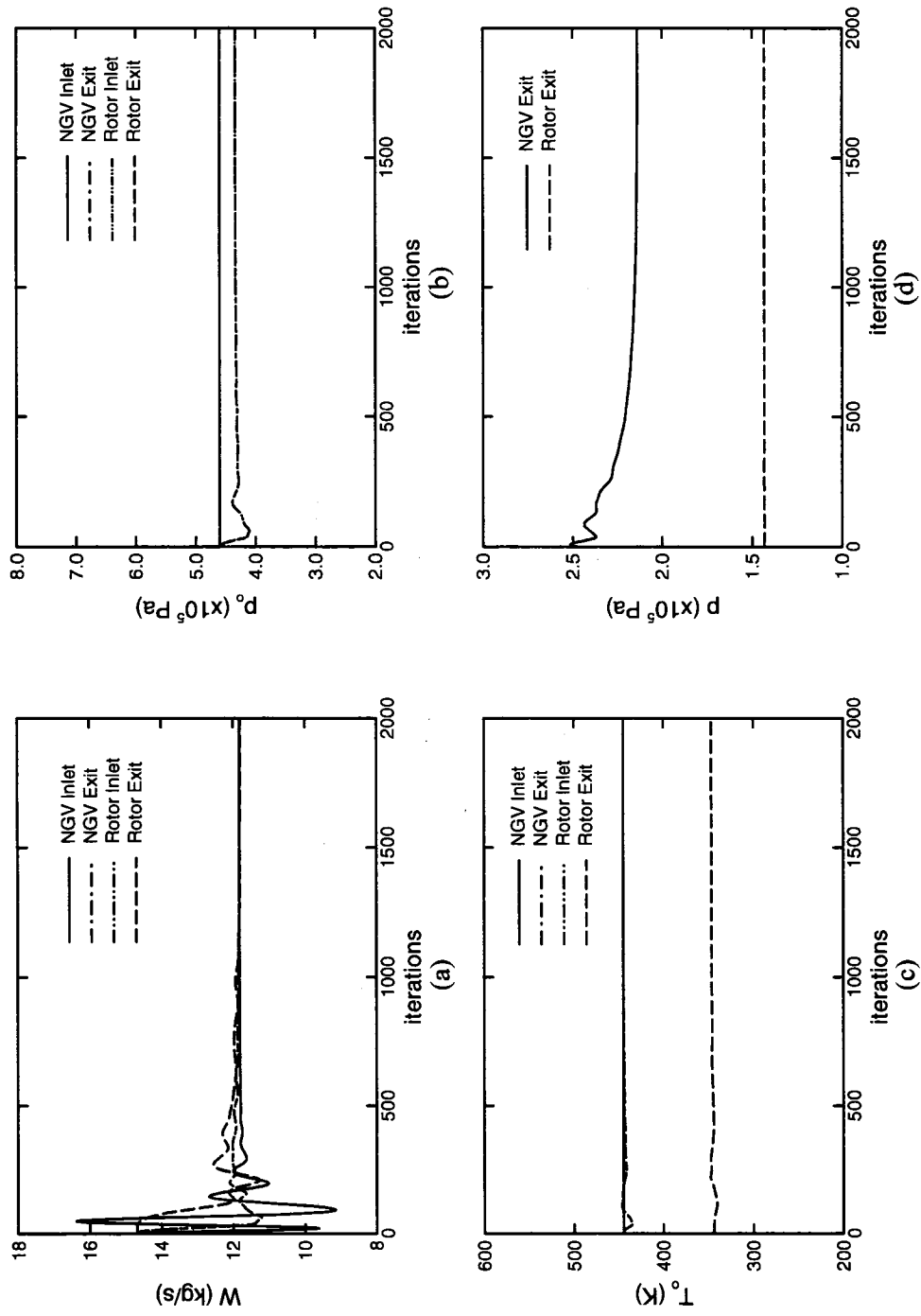
111

Figure 5.7 Convergence of the a) mass flow rate, b) stagnation pressure, c) stagnation temperature, and d) static pressure for the steady simulation of Case 7.

112

Table 5.2 Final steady-state values of the convergence parameters.

Location	Parameter	Steady-State Value							
		Baseline	Case1	Case 2	Case 3	Case 4	Case 5	Case 6	Case 7
NGV Inlet	$\dot{m}$ (kg/s)	11.810	11.809	11.808	11.791	10.154	8.784	11.810	11.803
	p_o (×10^5 Pa)*	4.599	4.599	4.599	4.599	4.599	4.599	4.599	4.599
	T_o (K)*	444	444	444	444	600	800	444	444
NGV Exit	$\dot{m}$ (kg/s)	11.816	11.815	11.816	11.807	10.157	8.786	11.834	11.806
	p_o (×10^5 Pa)	4.329	4.337	4.323	4.350	4.326	4.323	4.329	4.356
	p (×10^5 Pa)	2.094	2.135	2.074	2.123	2.092	2.099	2.092	2.232
	T_o (K)	444.322	444.322	444.321	444.218	600.057	800.126	444.326	444.327
Rotor Inlet	$\dot{m}$ (kg/s)	11.815	11.815	11.816	11.807	10.157	8.786	11.839	11.806
	p_o (×10^5 Pa)	4.329	4.337	4.324	4.351	4.326	4.323	4.329	4.356
	T_o (K)	444.322	444.323	444.322	444.219	600.059	800.129	444.326	444.328
Rotor Exit	$\dot{m}$ (kg/s)	11.793	11.797	11.791	11.945	10.140	8.774	11.758	11.785
	p_o (×10^5 Pa)	1.646	1.643	1.633	1.640	1.712	1.767	1.748	1.621
	p (×10^5 Pa)	1.434	1.432	1.434	1.433	1.434	1.434	1.434	1.433
	T_o (K)	348.542	346.312	350.267	348.634	479.989	651.654	358.811	344.491

* indicates values that were set as constants in the CFD solver.

Due to rapid convergence, in most cases, the results are shown up to 2000 iterations even though the steady simulations were allowed to run for 5000 iterations. The final steady-state values for all the convergence parameters are presented in Table 5.2. It can be seen from Figure 4.4 & Figures 5.1 to 5.7 that nearly all parameters converged to a single value. For the baseline case, Case 1, Case 2, Case 4, Case 5, Case 6 and Case 7, mass conservation can be observed. However, for Case 3, some fluctuations in the mass flow rate at the rotor exit were observed, varying between 11.54 and 11.94 kg/s. This was attributed to numerical error, and was deemed acceptable since the fluctuations represent differences of less than 3%. Meanwhile, as expected, the stagnation pressure and temperature remains the same from the NGV inlet to the rotor inlet since no work is extracted by the NGV, as it is stationary in the absolute reference frame. On the other hand, it can be seen that the stagnation pressure and stagnation temperature drop across the rotor indicating the presence of the turbine expansion process and the extraction of kinetic energy from the fluid. The mass-averaged static pressure at the rotor exits is constant due to the linear profile applied there. Finally, a drop in the static pressure from the NGV exit to the rotor exit was observed and was attributed to the turbine expansion process.

5.1.3 Time Periodicity of the Time-Accurate Solutions

Before results could be recorded, however, it is important that the unsteady simulation be allowed to run until time periodicity of the solution is attained. This ensures that the results will repeat after subsequent vane passings. Therefore, once the final steady-state solution was obtained, time dependence was implemented and the unsteady simulation

was allowed to for 10 vane passing periods or 2000 time steps. After this amount of time, it was deduced that the solution would have shown time periodic behaviour. The convergence of the mass flow rate, the stagnation pressure, the stagnation temperature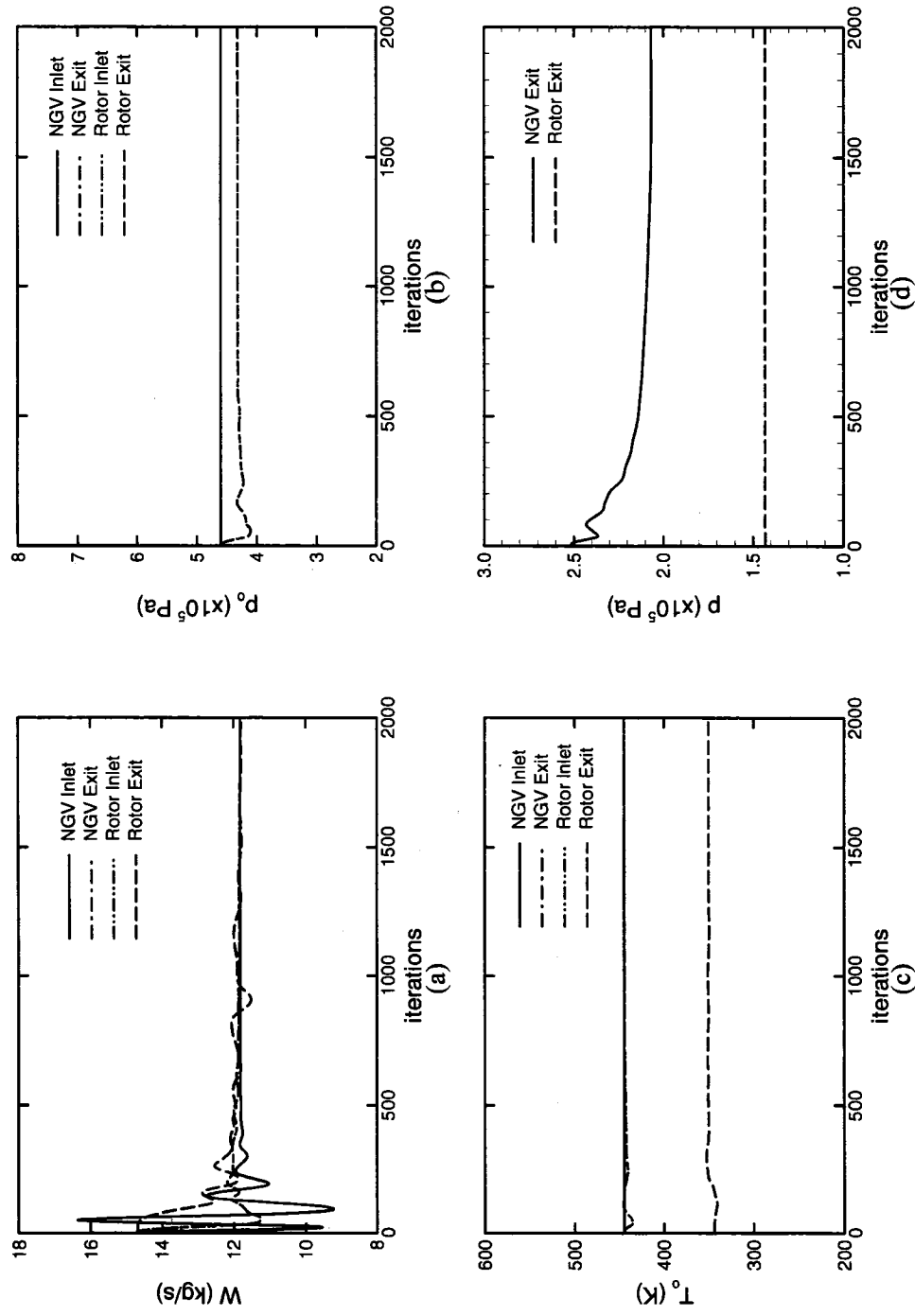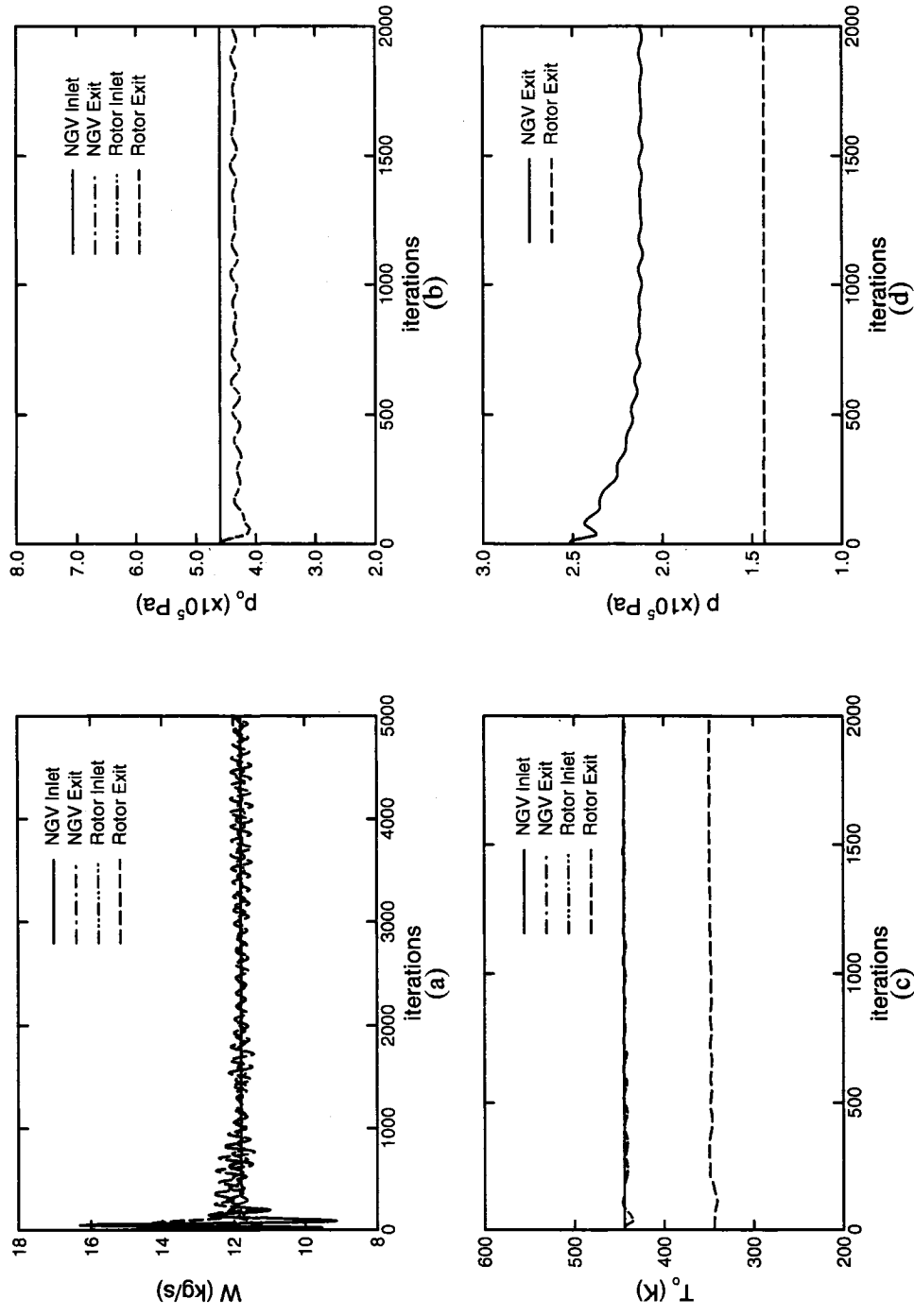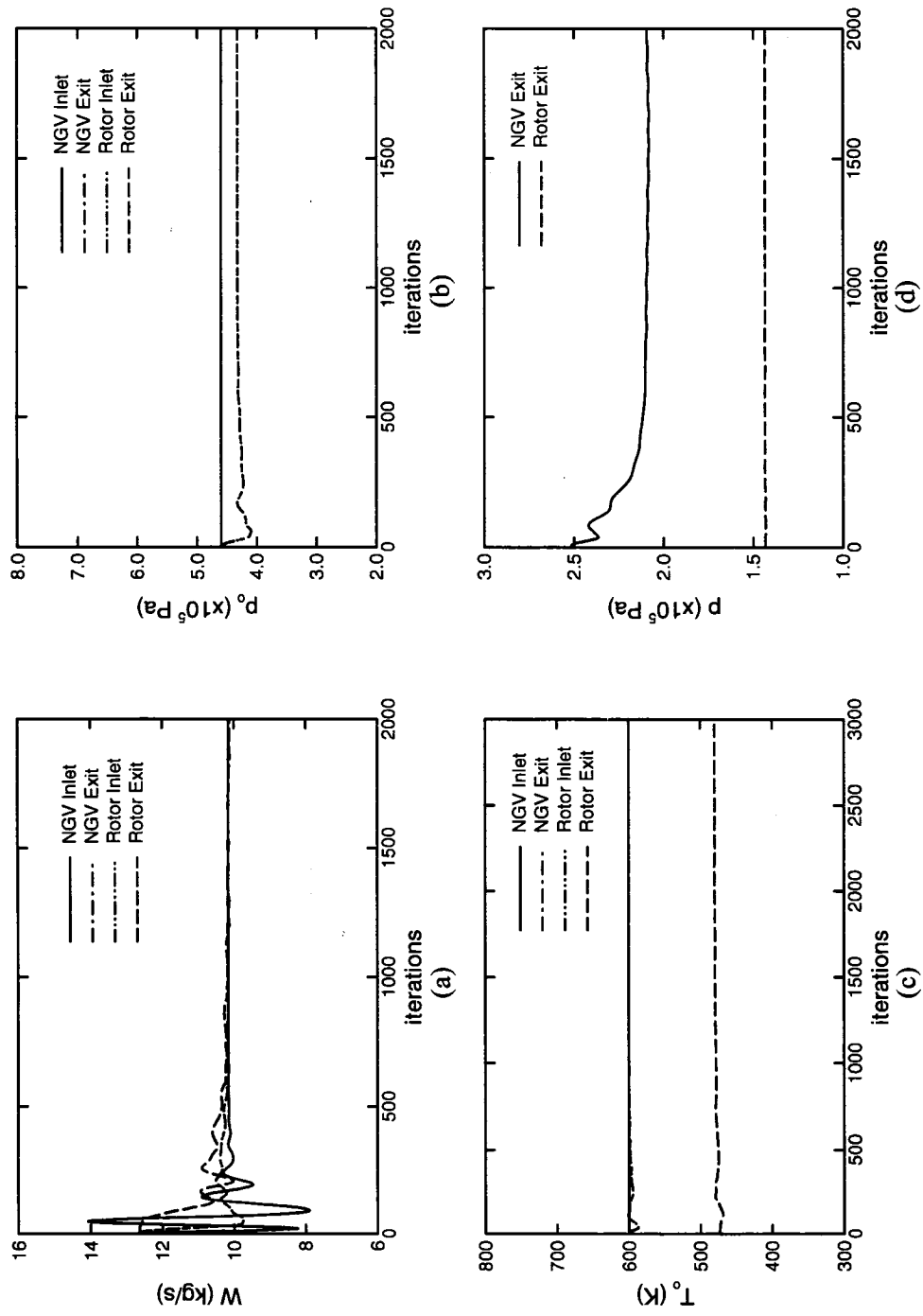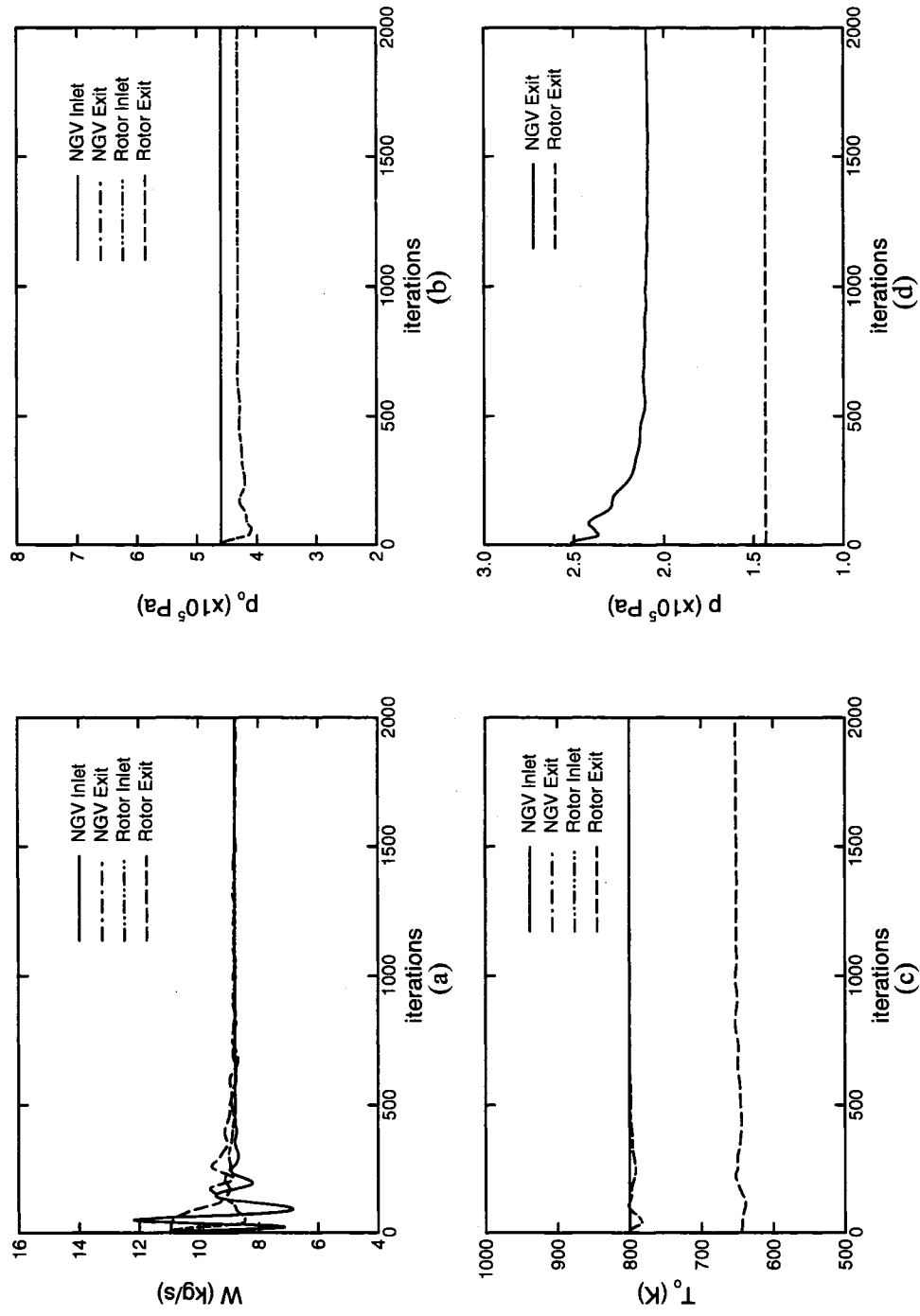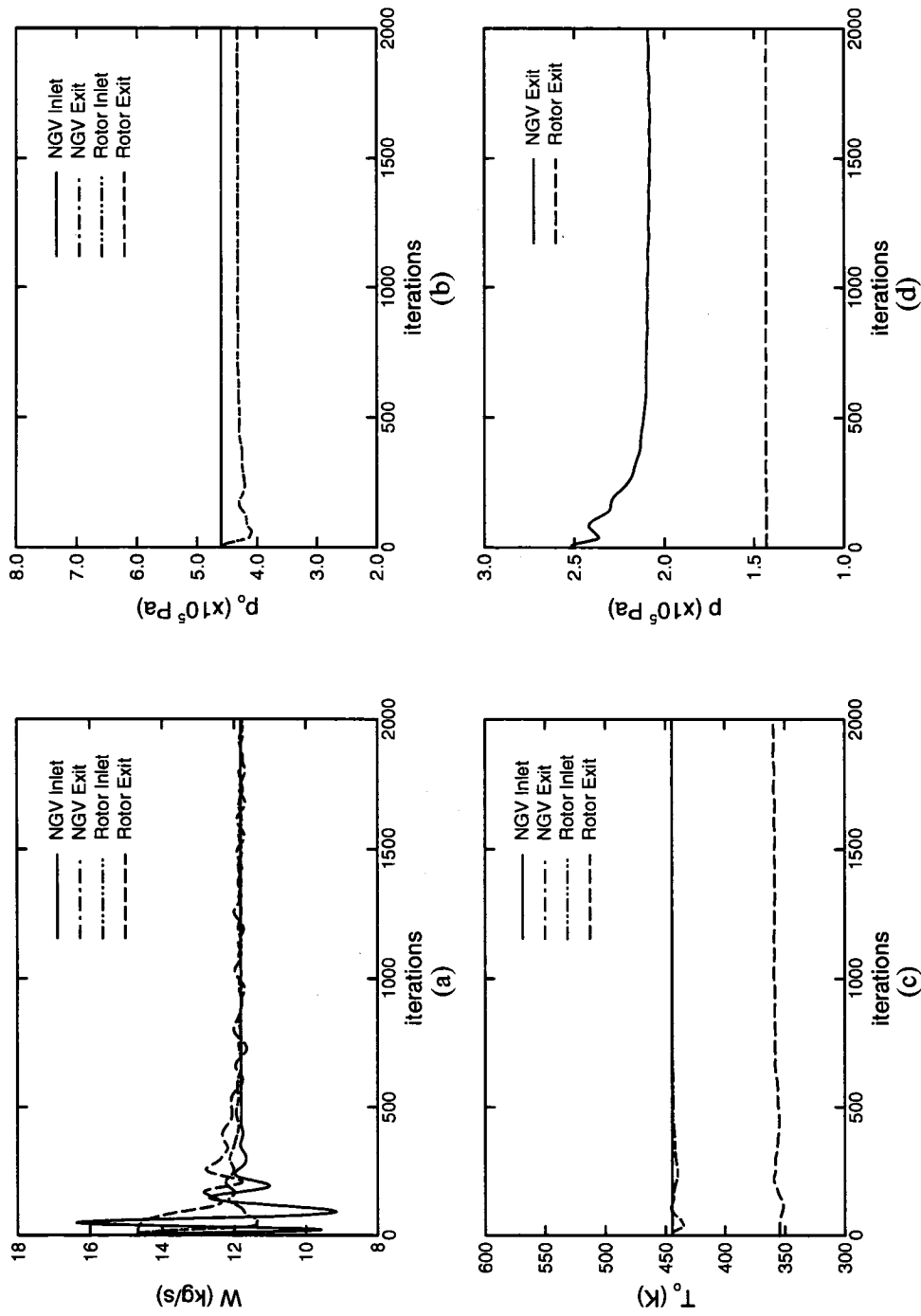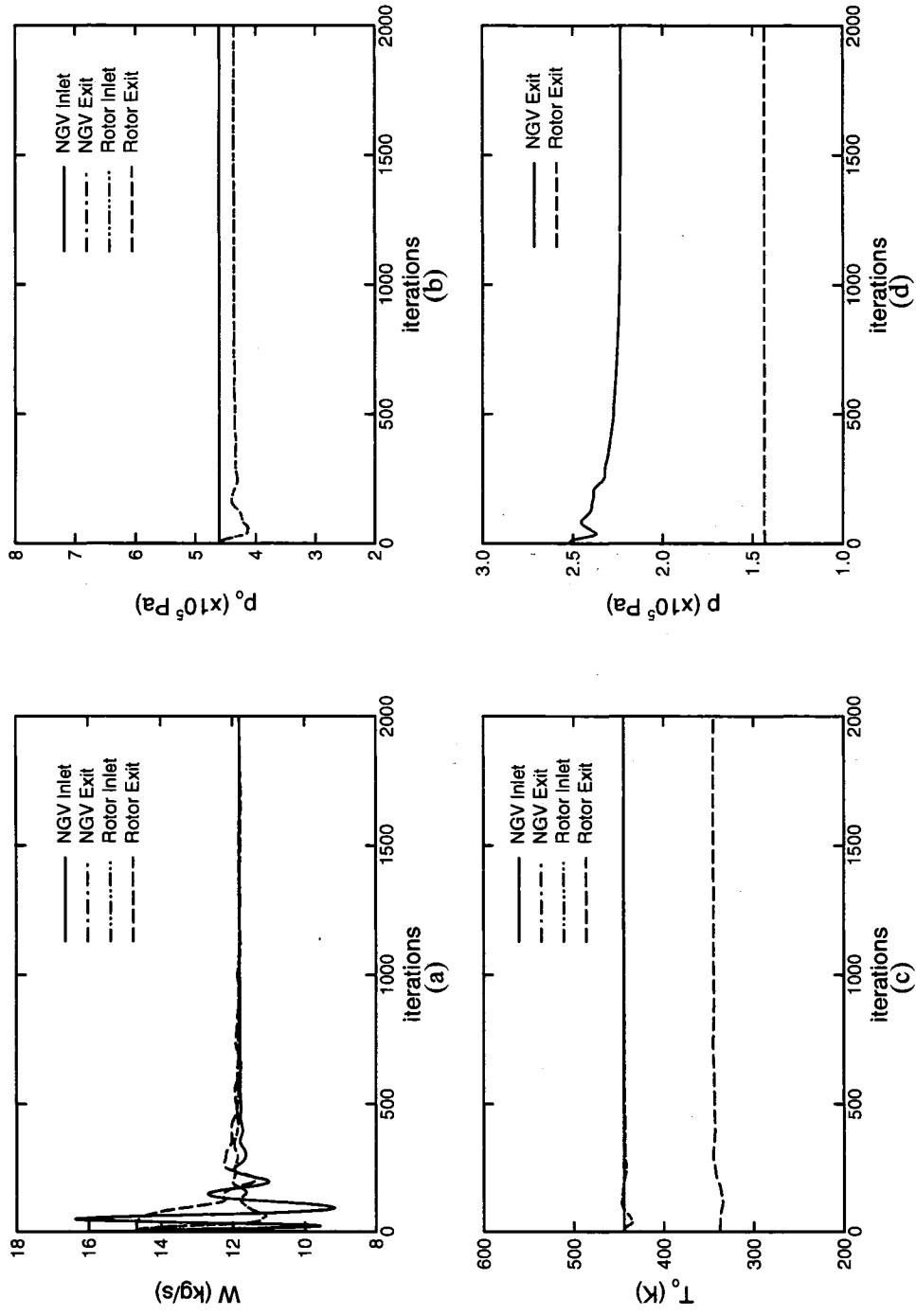, and static pressure for all the unsteady simulations are shown in Figures 5.8 to 5.15, and it can be seen that the results are indeed repeating with time. It is also important to note that the steady-state values presented in Table 5.2 fall within the time-accurate signals in Figures 5.8 to 5.15.

As mentioned before, the time periodicity of the results in the rotor domain should be equal to the vane passing period, and the convergence results confirm this. Consider the baseline case as an example. The rotor angular velocity is 9500 rpm and, since there are 30 vanes, the vane angular pitch is 12°. Thus, from Equation 5.2, the vane passing period is equal to 2.105×10^{-4} seconds, and so the time step size becomes $\Delta t = \Theta/200 = 1.052 \times 10^{-6}$ seconds. From Figure 5.8a, the rotor inlet mass flow rate signal can be seen to repeat itself at time steps 1784 and 1984, or over the span of 200 time steps, as expected. Similarly, the results obtained in the NGV domain are equal to half the vane passing period, which is expected since the blade pitch in the rotor domain is equal to half that of the vane pitch. From Figure 5.8d, the static pressure signal at the NGV exit repeats itself at time steps 1837 and 1937, or over 100 time steps. The unsteady convergence results for all cases show this trend, and so it was concluded the time periodicity of the results was successfully captured over 2000 time steps.
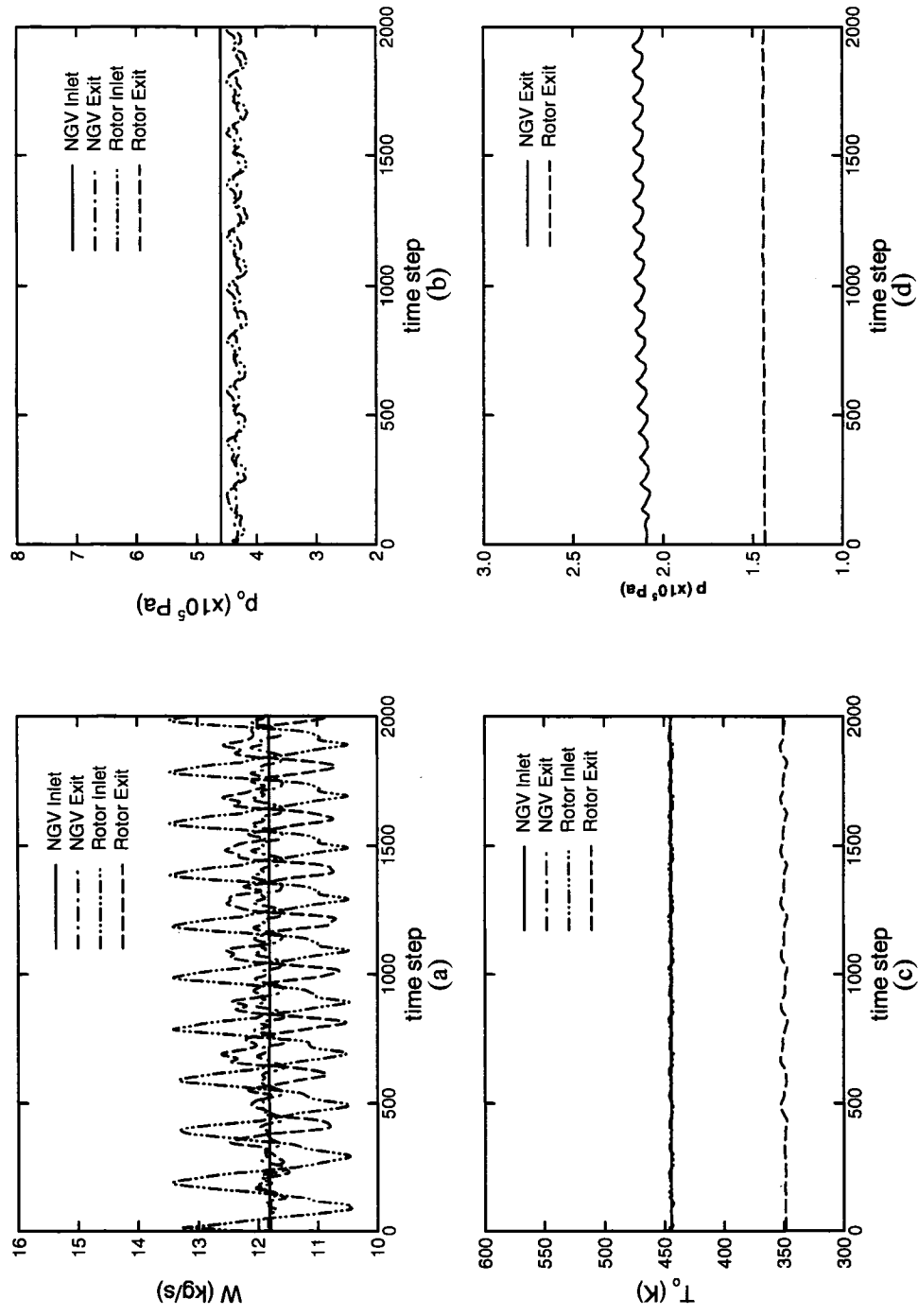
Figure 5.8 Convergence of the a) mass flow rate, b) stagnation pressure, c) stagnation temperature, and d) static pressure for the unsteady simulation of the baseline case.

116
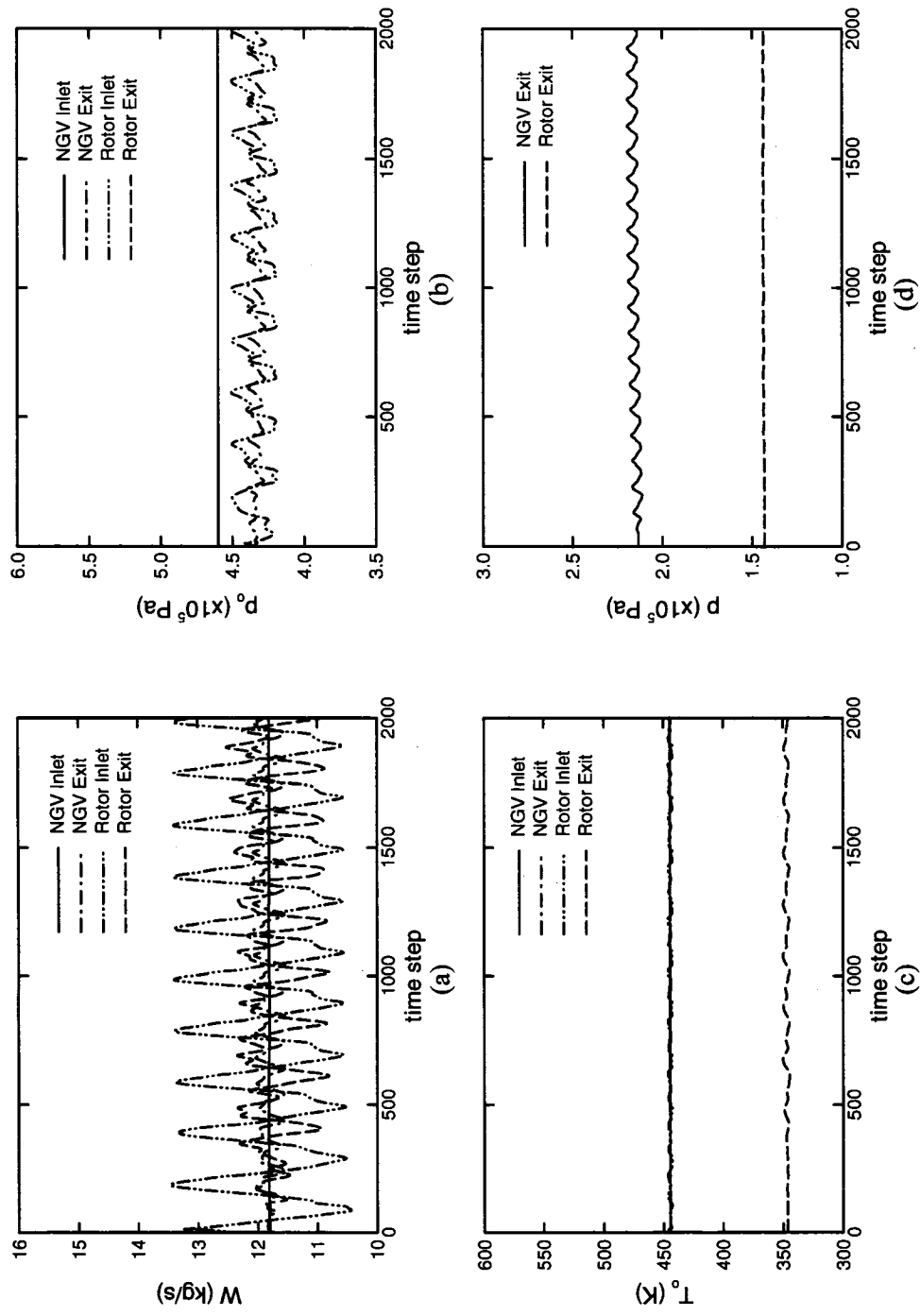
Figure 5.9 Convergence of the a) mass flow rate, b) stagnation pressure, c) stagnation temperature, and d) static pressure for the unsteady simulation of Case 1.

117
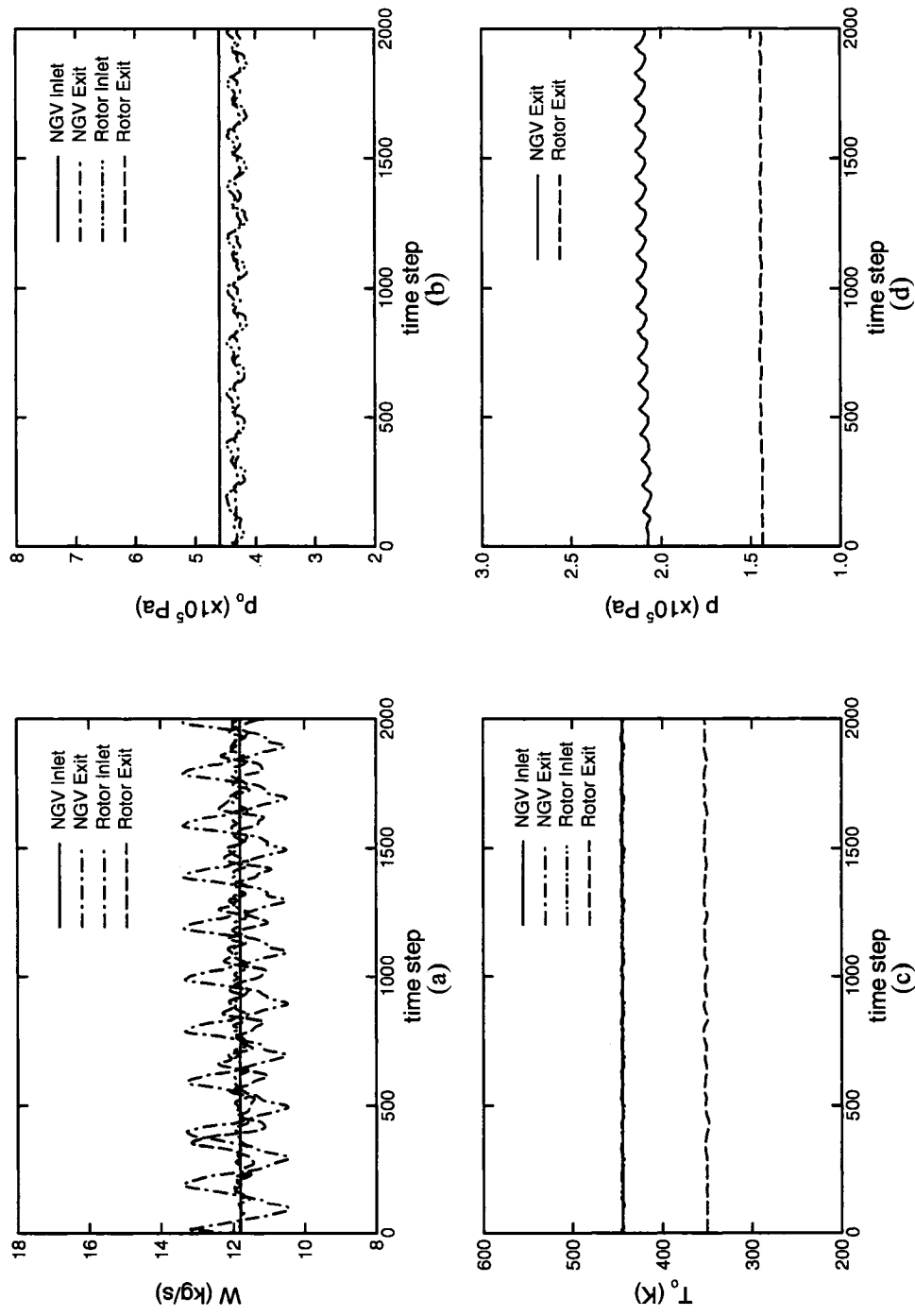
Figure 5.10 Convergence of the a) mass flow rate, b) stagnation pressure, c) stagnation temperature, and d) static pressure for the unsteady simulation of Case 2.

118
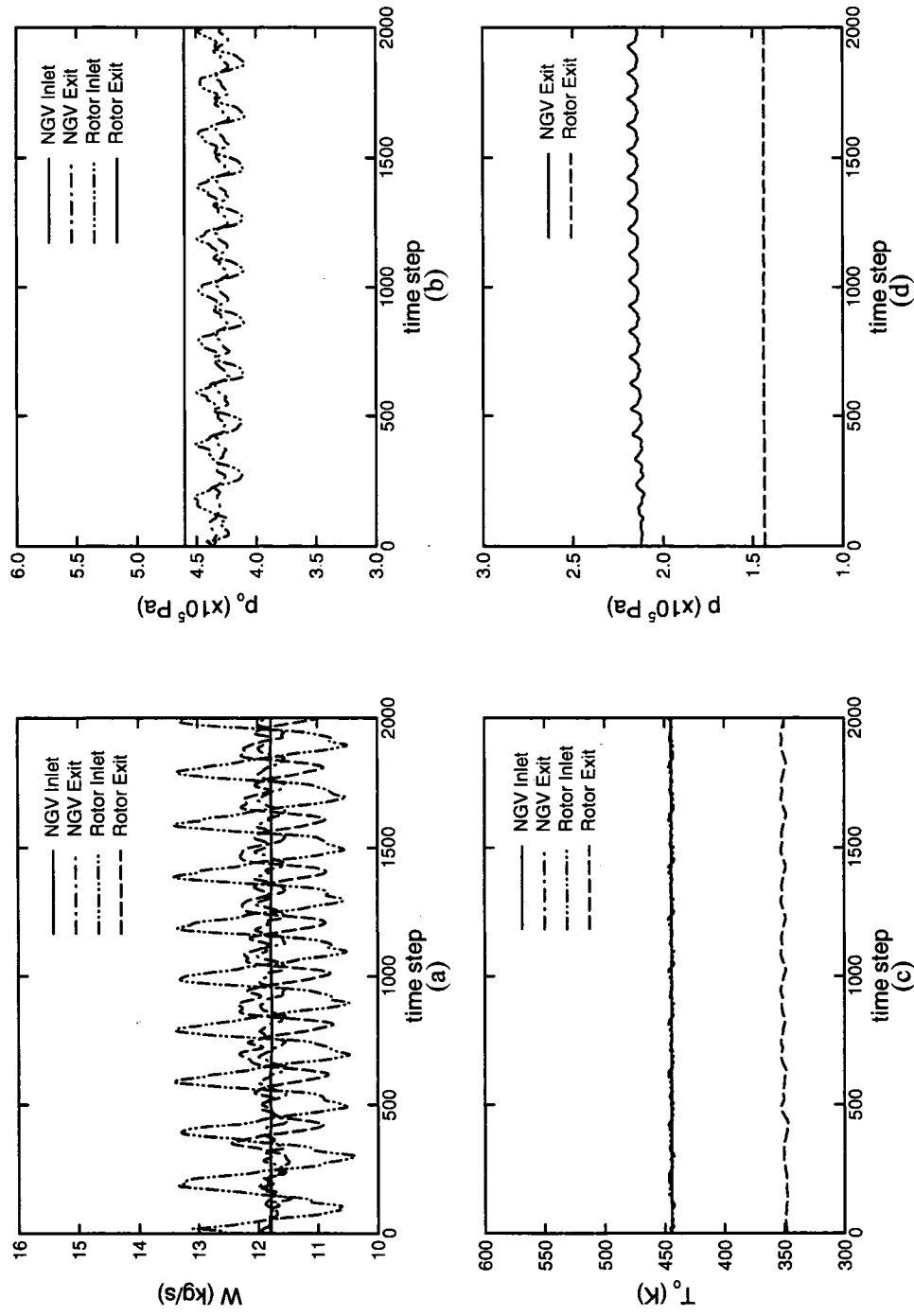
Figure 5.11 Convergence of the a) mass flow rate, b) stagnation pressure, c) stagnation temperature, and d) static pressure for the unsteady simulation of Case 3.

119
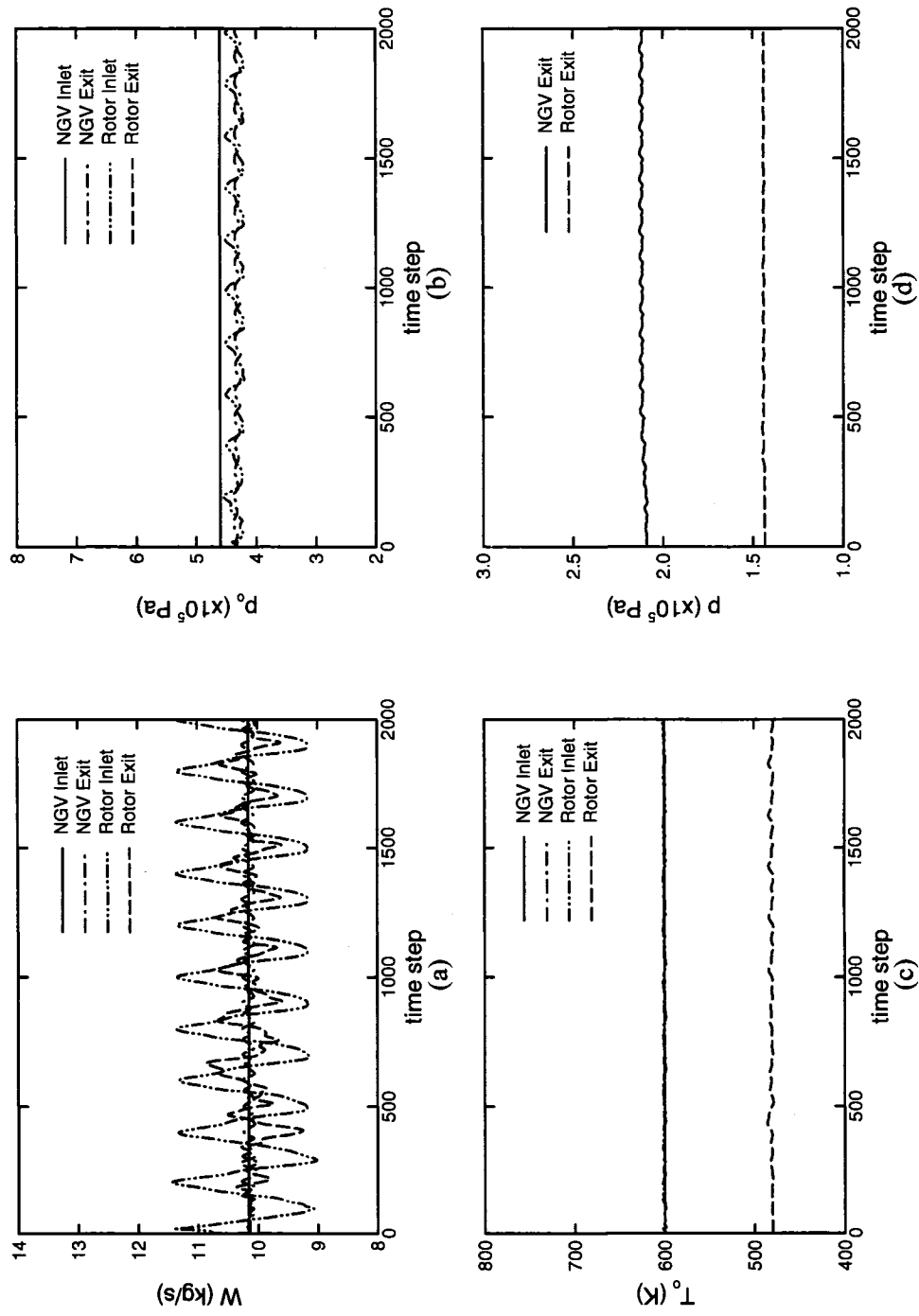
Figure 5.12 Convergence of the a) mass flow rate, b) stagnation pressure, c) stagnation temperature, and d) static pressure for the unsteady simulation of Case 4.

120
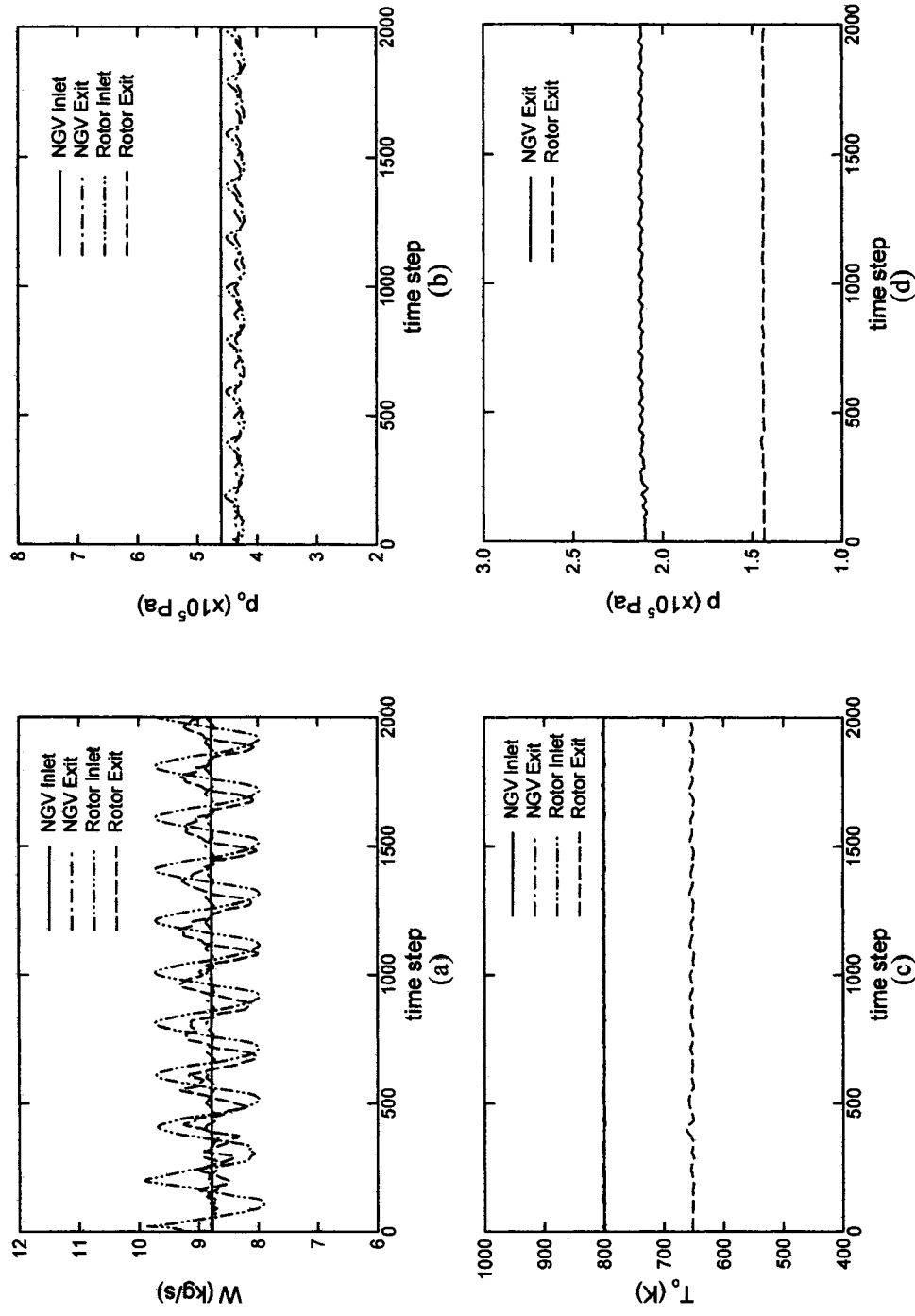
Figure 5.13 Convergence of the a) mass flow rate, b) stagnation pressure, c) stagnation temperature, and d) static pressure for the unsteady simulation of Case 5.

121
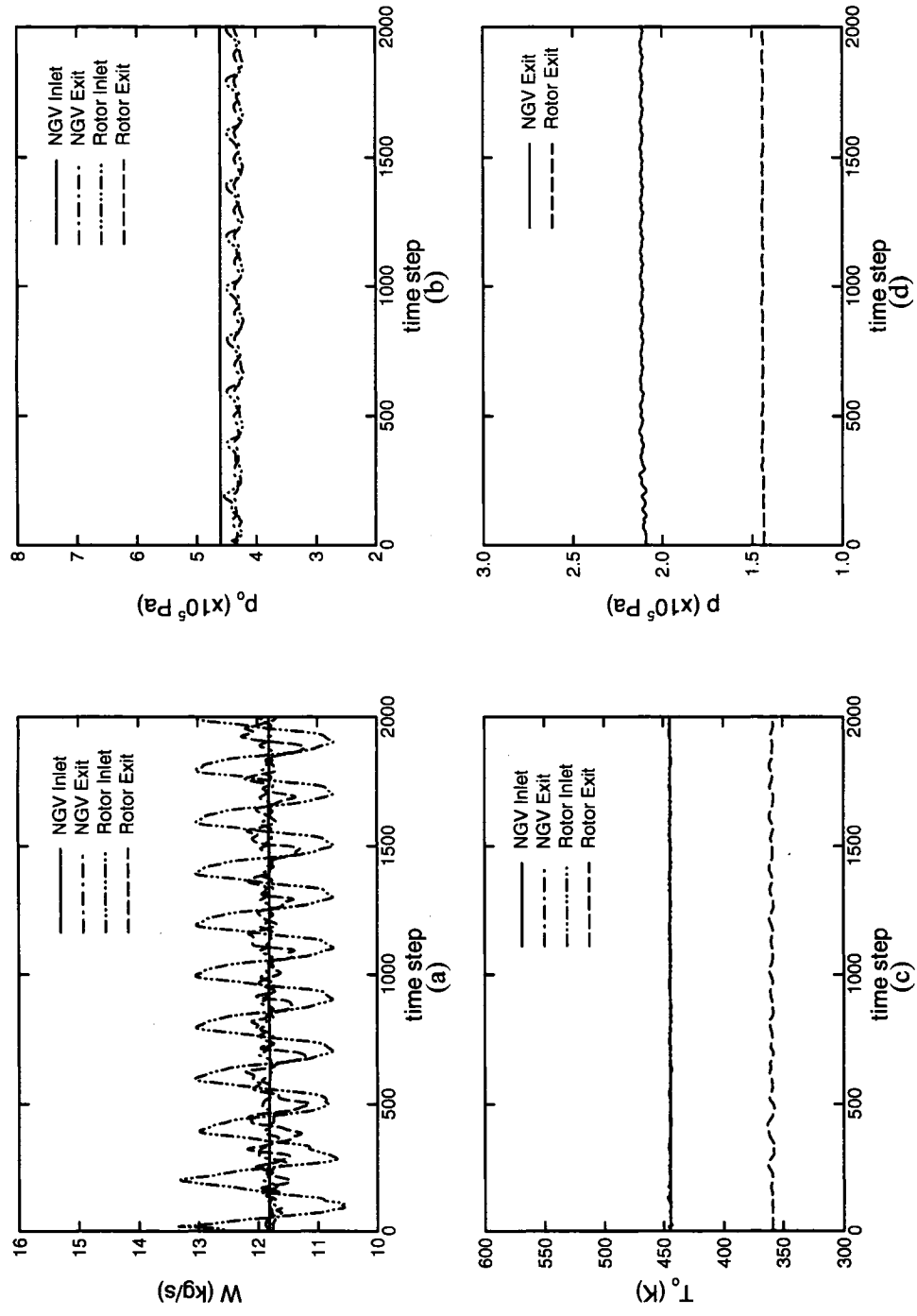
Figure 5.14 Convergence of the a) mass flow rate, b) stagnation pressure, c) stagnation temperature, and d) static pressure for the unsteady simulation of Case 6.
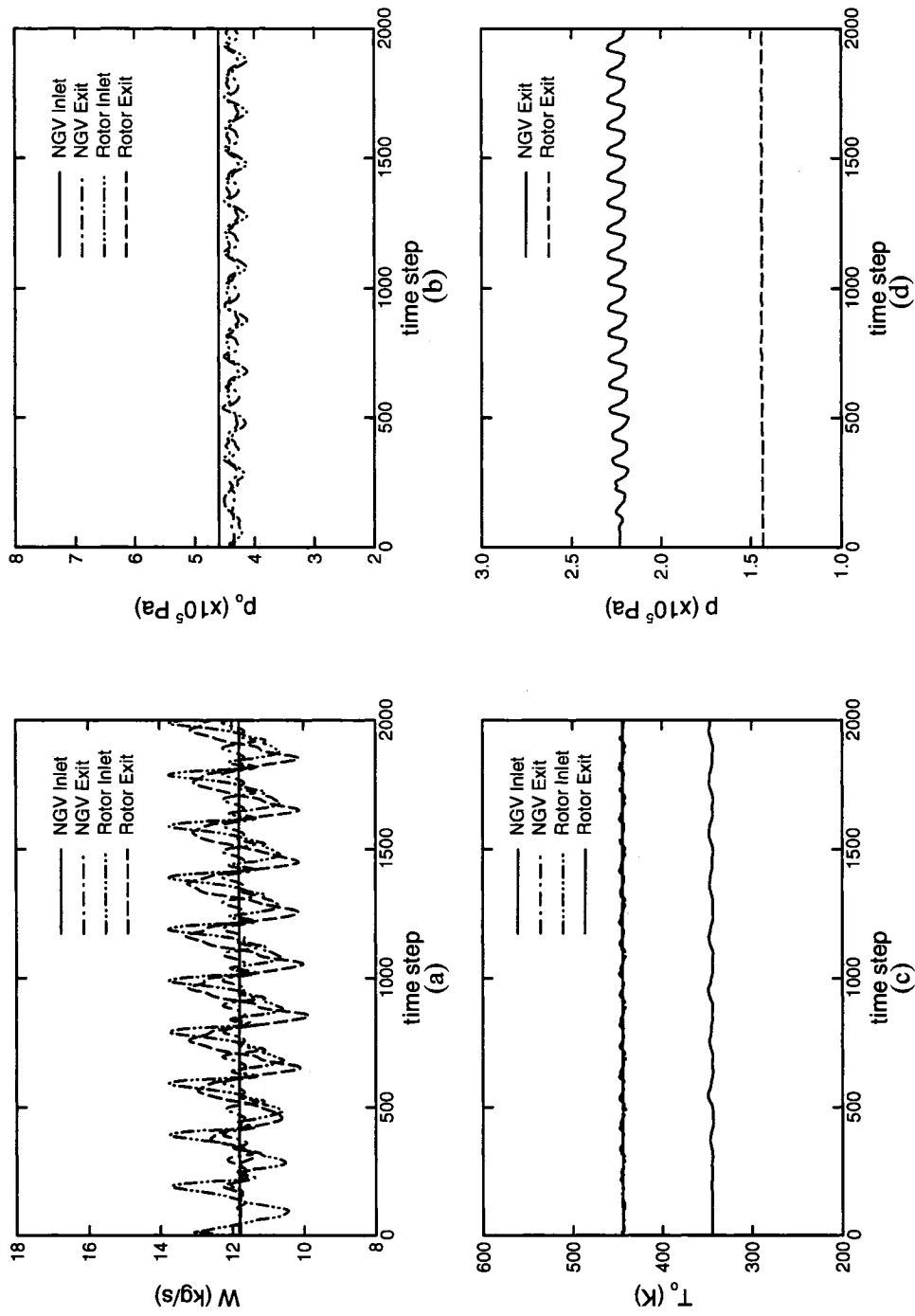
Figure 5.15 Convergence of the a) mass flow rate, b) stagnation pressure, c) stagnation temperature, and d) static pressure for the unsteady simulation of Case 7.

123

5.2 Baseline Case

Relative y-velocity profiles obtained at $x/C_x = 48\%$, along the camber line, and at different times in the tip clearance region are compared with that obtained in the time-averaged solution in Figure 5.16. It can be seen that the time-averaged profile provides a good approximation of the time-dependent solution as it falls between the solution at $t^* = 0.25$ and $t^* = 0.75$. However, the time-averaged solution fails to capture the high velocity obtained at $t^* = 0.25$ and $t^* = 0.50$ in the upper portion of the tip clearance region. The ability to capture these high velocities is important for predicting the high heat transfer rates on the shroud, thus time-dependent solutions should be used for studying flow and heat transfer mechanisms in the tip clearance region.

Figure 5.17 shows the static pressure contours in the tip clearance region at approximately $x/C_x = 48\%$ and along the camber line of the blade tip for the baseline case. At $t^* = 0.25$ and $t^* = 0.50$, the pressure inside separation bubble is lower than that at later times, indicating that the velocity inside the bubble is higher. The effect of the shroud relative motion combined with the presence of the cross-flow also accounts for the development of higher pressures at the suction side near the shroud from $t^* = 0.25$ to $t^* = 0.75$. The flow in this region is moving opposite to the leakage flow, moving from suction side to pressure side. The leakage flow, on the other hand, moves from the pressure side to suction side, and so the interaction between the two flows at the suction
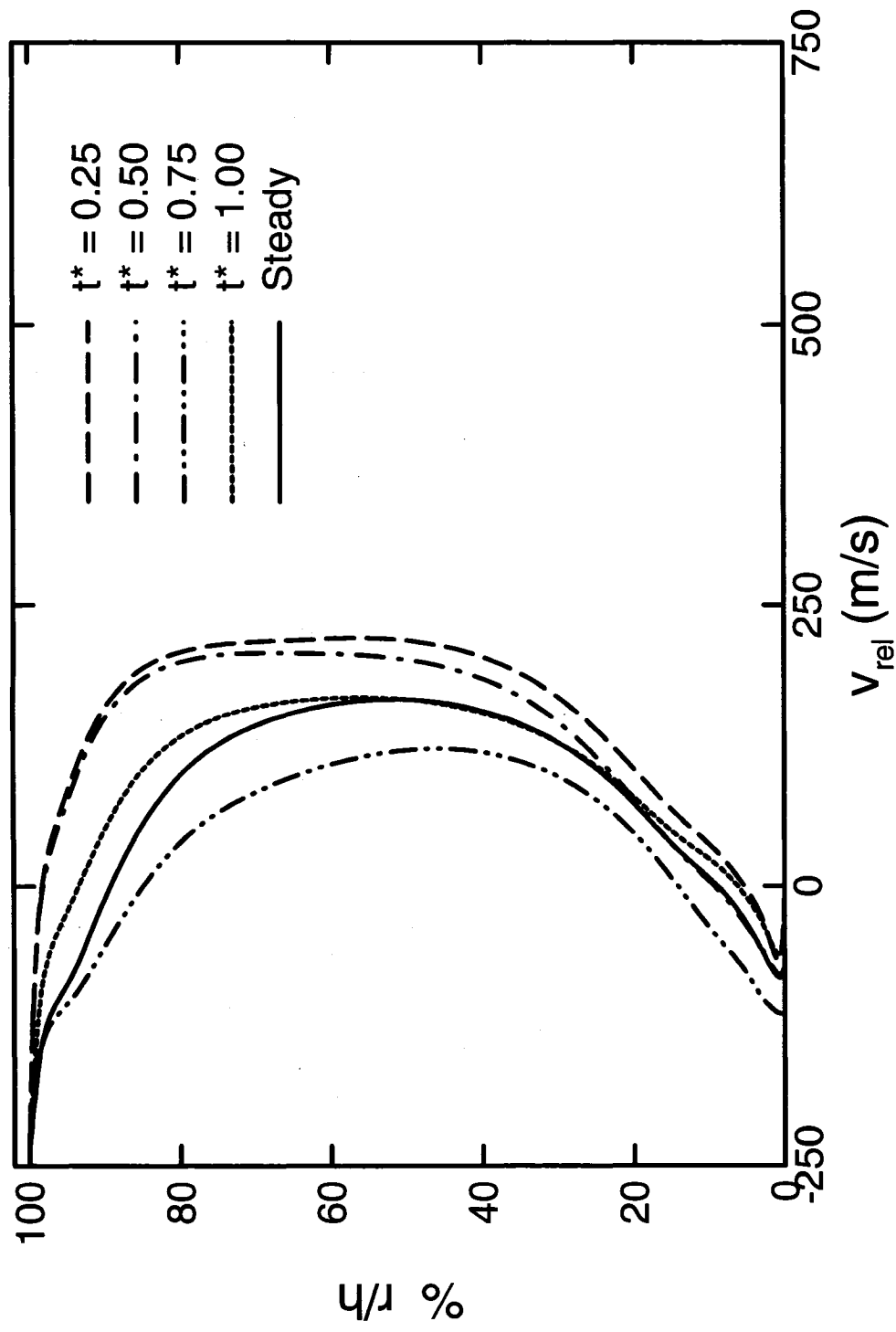
Figure 5.16 Comparison of the relative y-velocity profiles at $x/C_x = 48\%$, along the camber line, and at different times with that obtained with the time-averaged solution.
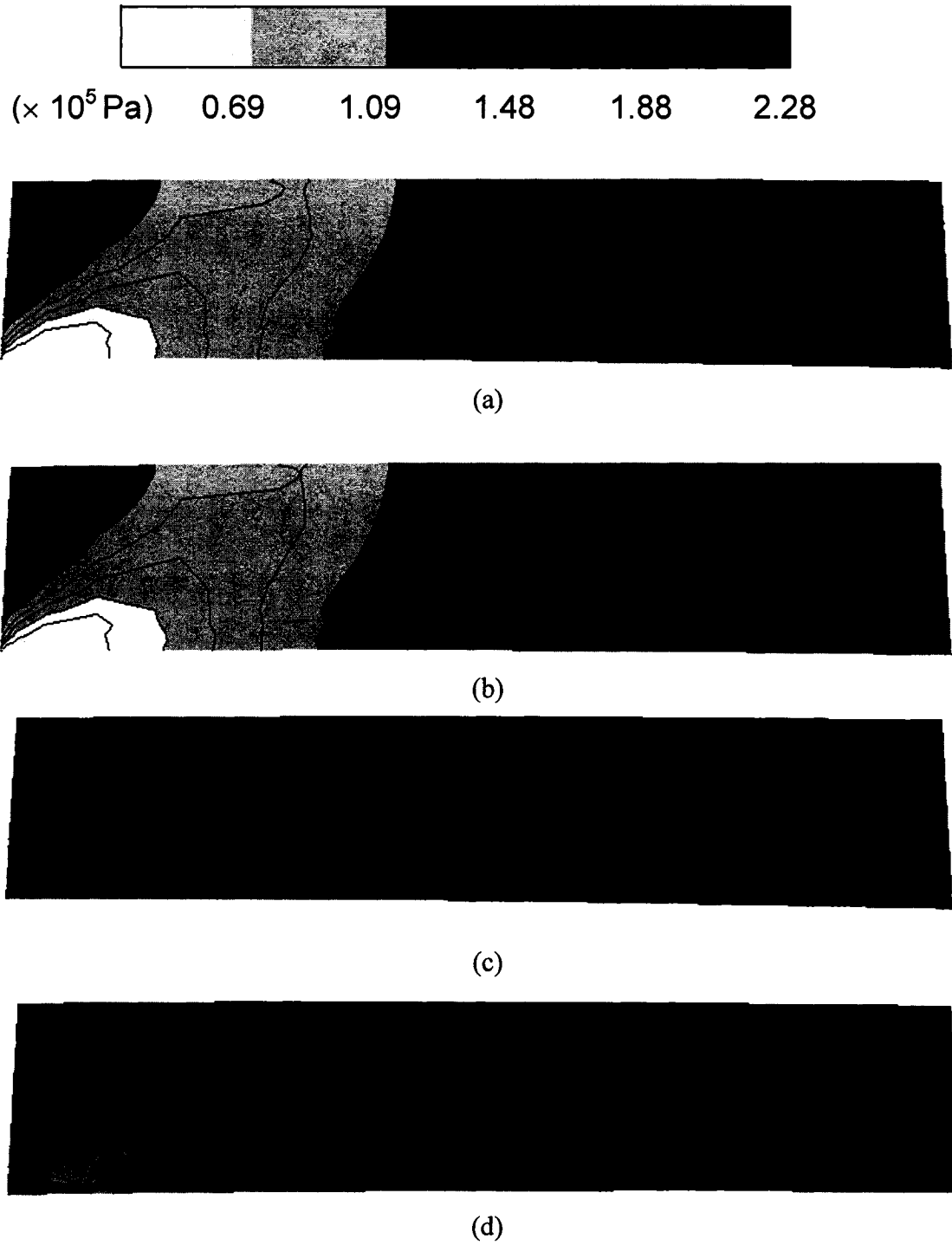
Figure 5.17 Static pressure contours in the tip clearance region for the baseline case at x/C_x = 48%, on the camber line of the blade tip, and at different times: a) $t^* = 0.25$, b) $t^* = 0.50$, c) $t^* = 0.75$, and d) $t^* = 1.00$.

generates a high-pressure region. At $t^* = 0.75$, the interaction of the opposing flow from the suction side with the leakage flow has now moved closer to the pressure side. The opposing flow is dominating near the shroud, while the leakage flow dominates near the blade tip. As a result, a lower pressure region at the suction side develops since flow is entering through the suction side at the shroud, while it is leaving near the blade tip.

Finally, at $t^* = 1.00$, it was observed that the opposing flow originating from the suction side begins to dissipate. Since the effect of the shroud relative motion remains the same, this means that the cross flow has dissipated. This is due to the fact that at this moment, the adjacent blade sees only vane passage flow and not the accelerated flow from the vane trailing edge. As a result, the effect of cross flow is reduced since the pressure gradient in the adjacent blade passage is reduced. Finally, at all times, a small low-pressure region was observed at the suction side of the blade tip, and this was attributed to the re-circulation caused by the downward moving leakage flow interacting with the flow passing over the suction side of the blade.

Figure 5.18 shows the static pressure contours just below the shroud for the baseline case. At all times, the re-circulation zone at the trailing edge of the airfoil was observed, and is the result of the leakage flow interaction with the cross flow at the suction side of the blade tip. At $t^* = 0.25$, a low-pressure region was observed in Figure 5.11a in the tip clearance region at the pressure side of the blade, which shows the separation bubble development as the leakage flow enters the tip clearance region. As time progresses, a high-pressure region begins to develop and grow at the suction side near the leading

Figure 5.18 Static pressure contours below the shroud for the baseline case at different times: a) $t^* = 0.25$, b) $t^* = 0.50$, c) $t^* = 0.75$, and d) $t^* = 1.00$.

edge, and this is due to the cross-flow in the passage interacting with the leakage flow leaving the tip clearance region. At $t^* = 0.75$, a small re-circulation zone was observed at the leading edge and at the suction side. At this time, the pressure is very high at the inlet of the shroud since the NGV passage is now upstream of the blade, allowing most of the flow leaving the vane to enter the rotor passage. As a result, the leakage flow leaving the tip clearance region at the leading edge is obstructed by this high-pressure flow at the inlet causing the re-circulation zone to form. In the rotor passage, high pressure-regions just below the pressure side of the blade were observed at all times. However, its size and location vary due to the passing of the vane just upstream of the rotor. From $t^* = 0.25$ to $t^* = 0.50$, the high-pressure region grows and extends towards the inlet of the rotor. This is due to the fact that the vane passage starting to pass by the blade. As mentioned above, $t^* = 0.75$ the vane passage is upstream of the blade at this time, thus the high-pressure region is largest since the high-pressure flow is entering the rotor from the NGV. At $t^* = 1.00$, the vane begins to pass over the rotor passage and so the accelerating flow from the vane airfoil is entering the rotor passage, thus generating low-pressure at the inlet of the rotor. This low-pressure region continues to grow as seen from Figure 5.18a, until the vane passage passes over once again.

The static temperature contours just below the shroud for the baseline case are shown in Figure 5.19. The static temperature is high at the inlet of the rotor and decreases in the axial direction as the flow accelerates through the rotor due to energy conservation. Now, high heat transfer rates to the shroud are the result of high adiabatic wall
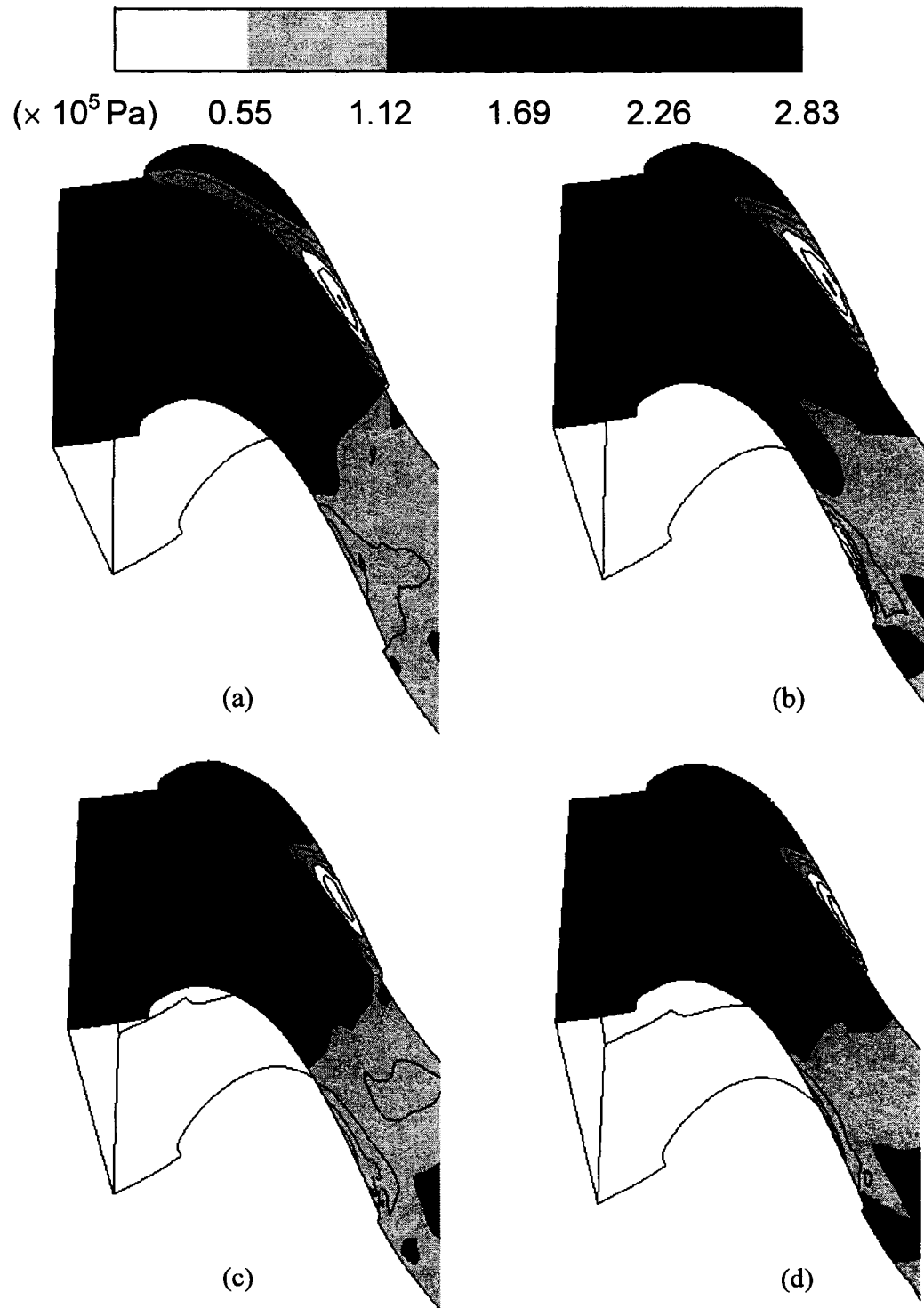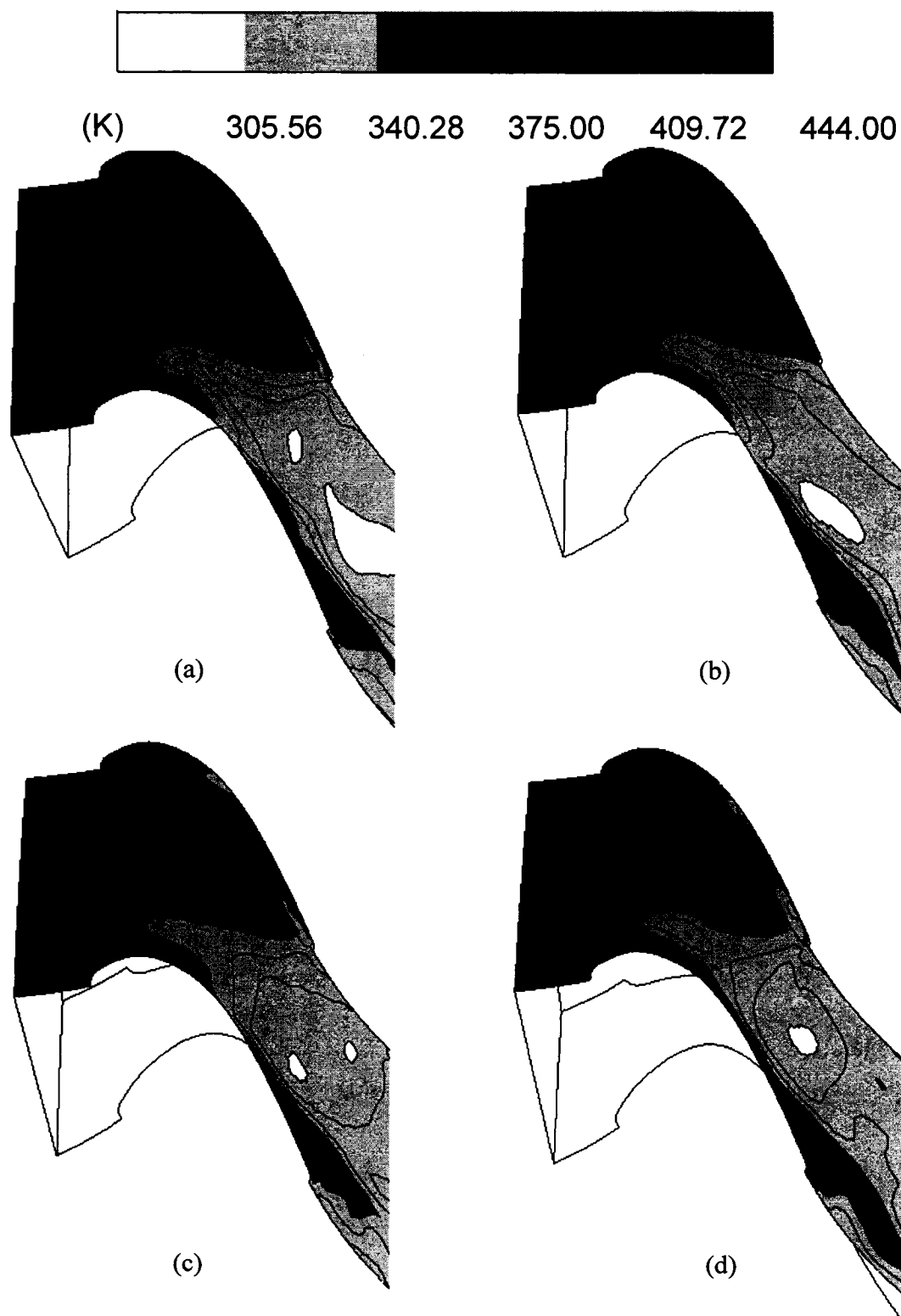
Figure 5.19 Static temperature contours below the shroud for the baseline case at different times: a) $t^* = 0.25$, b) $t^* = 0.50$, c) $t^* = 0.75$, and d) $t^* = 1.00$.

temperatures. The static temperature shown here can be considered the adiabatic wall temperature since the data is recorded so close to the shroud. Thus, it can be seen that high heat transfer rates will occur in the tip clearance region near the leading edge of the blade, and this has been observed in previous studies, including Chana and Jones (2003). The region of high temperature in the tip clearance is largest at $t^* = 0.25$ since there is very little leakage flow resisting the flow near the shroud. At $t^* = 0.50$, the high-temperature region near the leading edge begins to decrease as the leakage flow begins to accelerate through the tip clearance region, attaining its smallest size at $t^* = 0.75$. At $t^* = 1.00$, the high temperature region starts to grow again due to the dissipation of the leakage flow.

5.3 Parametric Study

5.3.1 Effect of Tip Clearance Height

The contours for Case 1 ($h = 0.6$ mm), presented in Figure 5.20, show that the separation bubble is much smaller in the circumferential direction due to the fact that only half the mass flow is entering the tip clearance region since the tip clearance height is half that used in the baseline case. However, the pressure distribution remains similar to that of the baseline case, with a relatively high separation bubble and small re-circulation region occurring at the suction side blade tip occurring at all times. This re-circulation zone was attributed to the downward moving leakage flow interacting with the flow passing over the suction side of the blade.

131
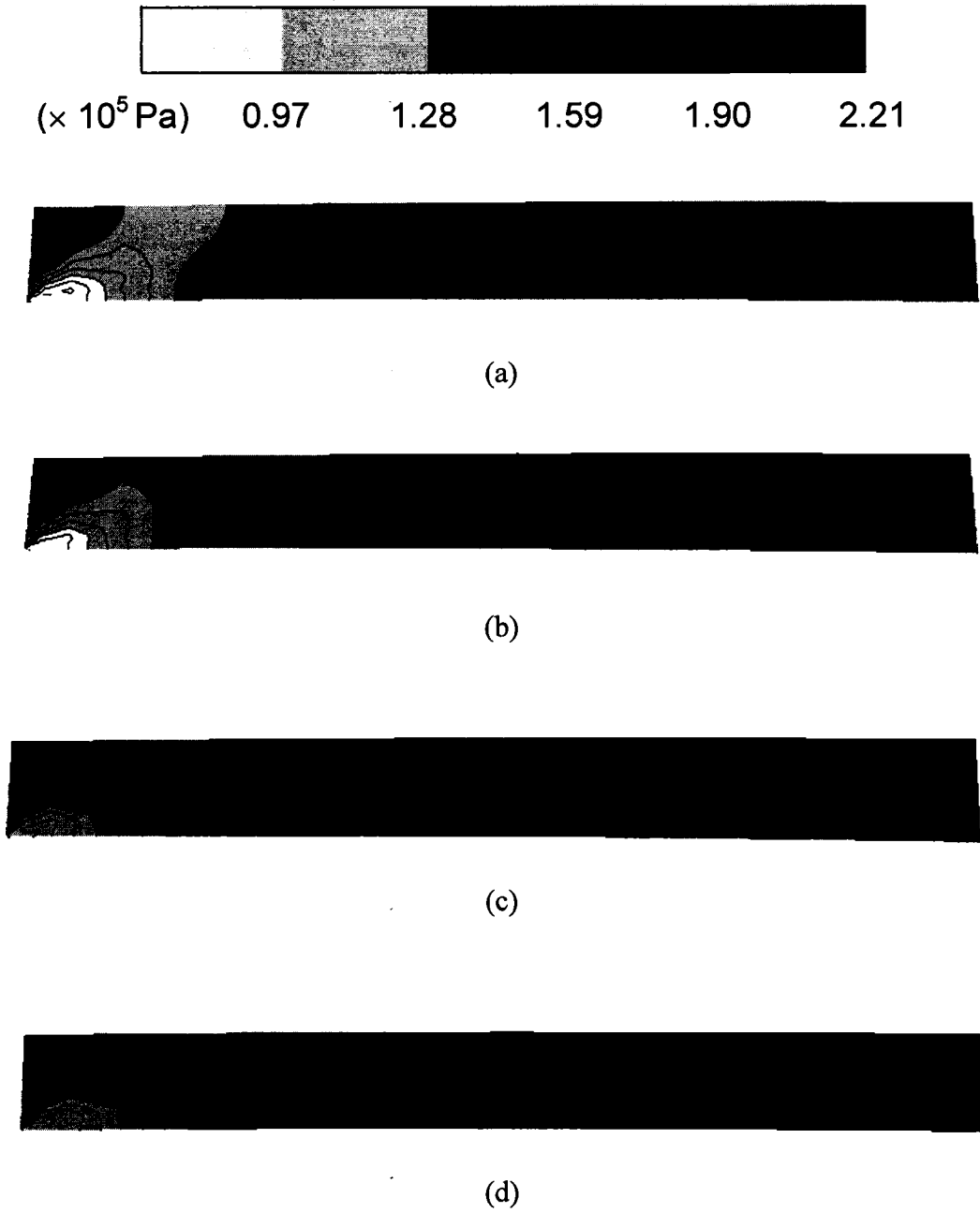
Figure 5.20 Static pressure contours in the tip clearance region with $h = 0.6$ mm at $x/C_x =$ 48%, on the camber line of the blade tip, and at different times: a) $t^* = 0.25$, b) $t^* = 0.50$, c) $t^* = 0.75$, and d) $t^* = 1.00$.

Figure 5.21 shows the relative y-velocity contours in the tip clearance region with a height of 2 mm. It can be seen that the separation bubble spans nearly the entire span of the tip clearance region from the pressure side to the suction side at all times. Since the tip clearance is large, the leakage flow is able to dominate a larger portion of the tip clearance region. Thus, the leakage flow moves more horizontally, and is only directed downward by the opposing flow near the suction side, instead of near the pressure side as in other cases. Also, more mass flow enters the tip clearance region since the height is larger. At $t^* = 0.25$, it can be seen that the leakage flow dominates a very large portion of the tip clearance region, thus a very long separation bubble develops near the blade tip.

At $t^* = 0.50$, the opposing flow slows down the leakage flow near the suction side, and forces the leakage flow to move downwards, thus shortening the separation bubble. As time progresses, the leakage flow becomes dominant once again, since the larger tip clearance allows more mass flow to enter, as mentioned before.

Comparison with the baseline case of the mass flux entering the pressure side of the tip clearance region, at midspan, is shown in Figure 5.22. As expected, less mass flow enters the tip clearance region for the smaller tip clearance case, while more mass flow enters for the larger tip clearance case. From Figure 5.22, it can be seen that all times, the same amount of mass flow is entering the pressure side at all locations for tip clearances. It is also interesting to note that the re-circulation at the trailing edge for both tip clearances occurs at $x/C_x = 82\%$. At this location, mass flow is leaving the pressure side as indicated by the negative flow rates from here to the trailing edge. This shows that at the midspan

133
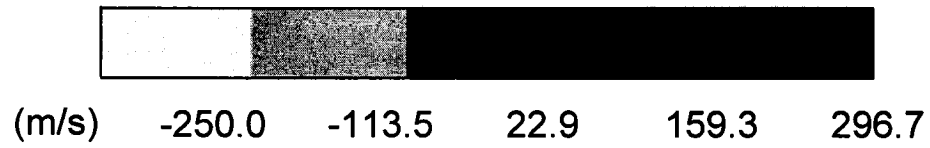
Figure 5.21 Relative y-velocity contours in the tip clearance region with $h = 2.0$ mm at $x/C_x = 48\%$, on the camber line of the blade tip, and at different times: a) $t^* = 0.25$, b) $t^* = 0.50$, c) $t^* = 0.75$, and d) $t^* = 1.00$.

Figure 5.22 Comparison of the mass flow rate entering the pressure side of the blade at different tip clearance heights at the midspan of the tip clearance region, and at times: a) $t^* = 0.25$, b) $t^* = 0.50$, c) $t^* = 0.75$, and d) $t^* = 1.00$.

135

the development of the re-circulation zone does not depend on the tip clearance height, which makes sense since the flow conditions outside the tip clearance region have not been modified. The secondary cross flow originating from the adjacent blade passage remains the same, and interacts with the leakage flow from the smaller tip clearance region in the same manner as in the baseline case.

The mass flow rates leaving the tip clearance region through the suction side for Case 1, Case 2, and the baseline cases are shown in Figure 5.23. Negative flow rates indicate flow leaving the suction side. At all times, there is very little flow leaving the suction side between 29% x/C_x and 36% x/C_x. In fact, at $t^* = 1.00$, the mass flow rates between 29% x/C_x and 36% x/C_x are positive, indicating back flow into the tip clearance region. This can be explained by the fact that the thickness of the airfoil is greatest within this region. Since less mass flow enters the tip clearance region, the leakage flow has less inertia to overcome the shroud boundary layer flow where the airfoil thickness is largest. The leakage flow instead deviates towards paths of least resistance where the airfoil thicknesses are smaller, which explains why more leakage flow leaves the suction side upstream and downstream this region.

Figure 5.24 shows the relative y-velocity profiles along the camber line at different axial positions in the tip clearance region at $t^* = 1.00$. Near the leading edge, the y-velocity profiles are similar with maximum velocities of approximately 250 m/s since the leakage flow sees the same pressure drop before entering the tip clearance region. Near the

136
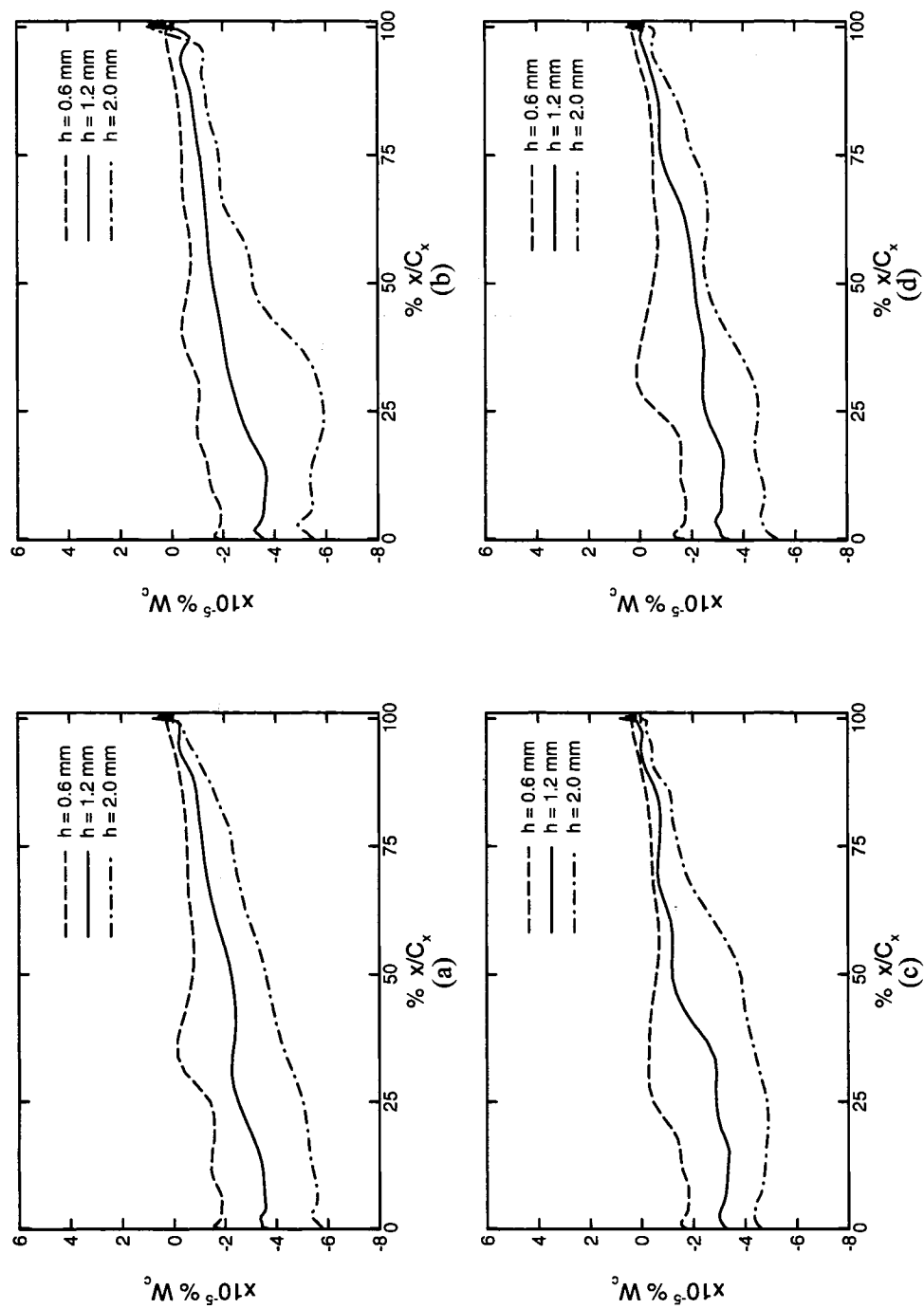
Figure 5.23 Comparison of the mass flow rate entering the suction side of the blade at different tip clearance heights at the midspan of the tip clearance region, and at times: a) $t^* = 0.25$, b) $t^* = 0.50$, c) $t^* = 0.75$, and d) $t^* = 1.00$.

137
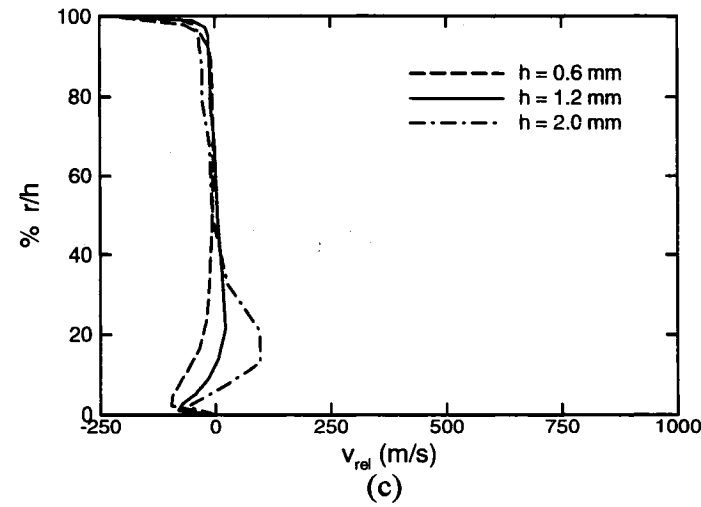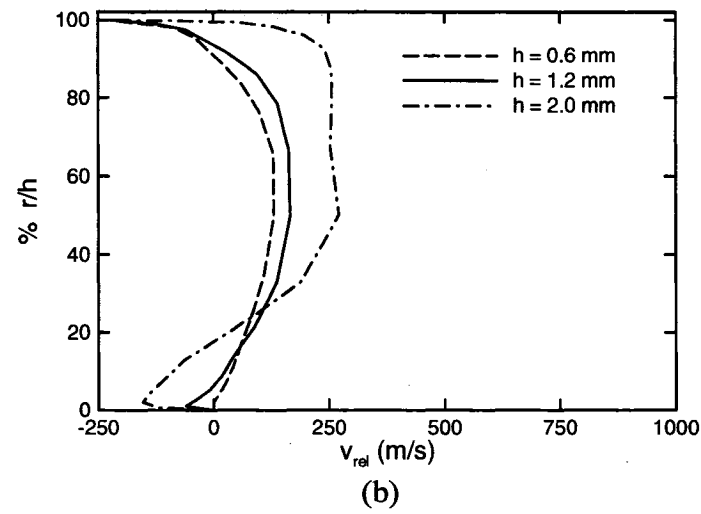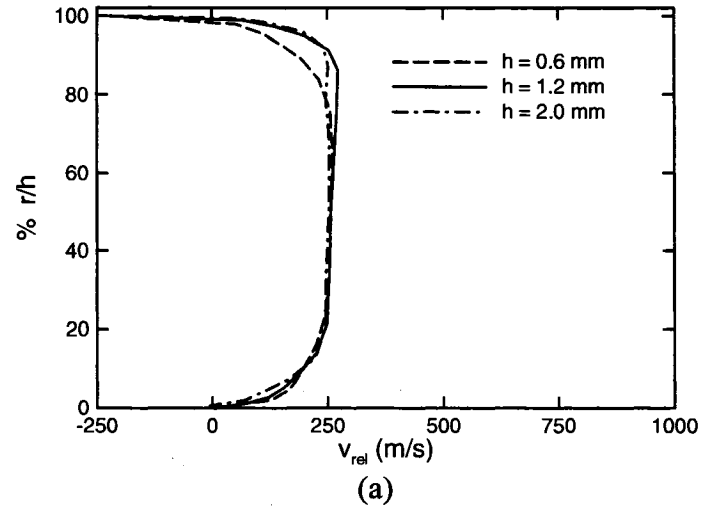
Figure 5.24 Relative y-velocity profiles along the camber line for different heights at $t^* =$ 1.00 at a) $x/C_x = 5\%$, b) $x/C_x = 48\%$, and c) $x/C_x = 95\%$.

shroud at r/h = 66%, the boundary layer is less steep for the smaller tip clearance case since the separation bubble stretches higher in the tip clearance region. Thus, the leakage flow is slower in the upper portion as the leakage flow has to negotiate over the separation bubble for the smaller tip clearance case (Case 1). At x/C_x = 48%, it can be seen that the leakage flow velocity is higher for the large tip clearance case (Case 2) in the upper portion of the tip gap, as mentioned before. Similarly, the velocity inside the separation bubble is larger for Case 2. It is important to note that at the trailing edge, the pressure side and suction side nearly coincide with each other since the airfoil thickest is smallest. In Figure 5.24c, it can be seen that the velocity is nearly zero as the leakage flow decelerates as it encounters the opposing flow from the suction side. Small re-circulation was observed near the blade tip for the baseline case and Case 1 due to the interaction of the radially-downward leakage flow with the opposing flow from the suction side. On the other hand, in Case 2, the velocity is positive (moving from the pressure side to suction side) from r/h = 4% to 44 %, which represents the high velocity inside the separation bubble, which spans from the pressure side to the suction side.

5.3.2 Effect of Inlet Turbulence Intensity

In Figure 5.25, the pressure contours in the tip clearance region for Case 3 (I = 0.5%) are shown, and the trend is very similar to that of the baseline case with a relatively large separation bubble and small re-circulation zones at the suction side blade tip. The static pressures are slightly lower, however, indicating higher velocities in the tip clearance region. Since the flow turbulence is lower in this case, there will be less random motion of the fluid particles inside the axially-moving bulk flow. As a result, there will be more

139
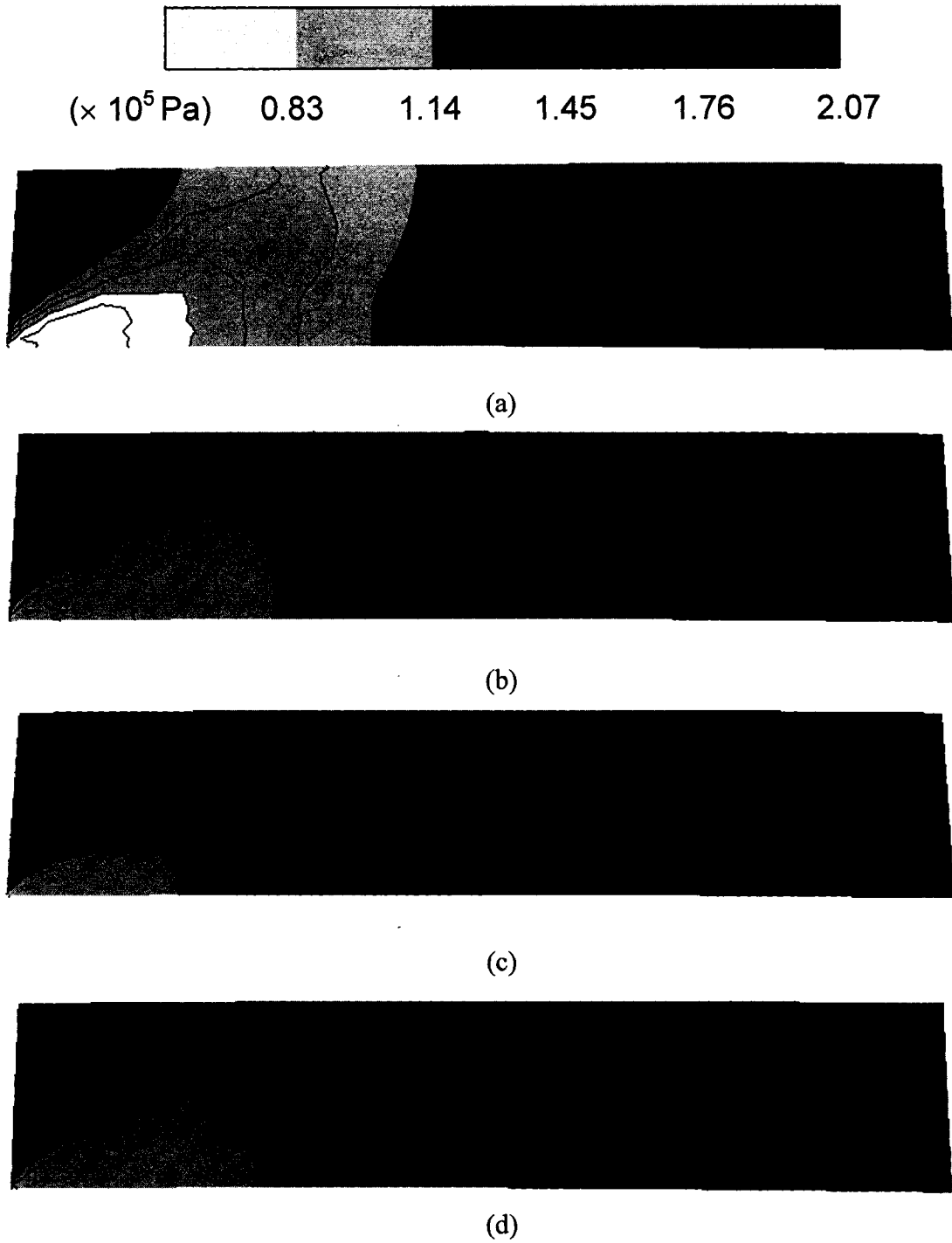
Figure 5.25 Static pressure contours in the tip clearance region with $I = 0.5\%$ at $x/C_x =$ 48%, on the camber line of the blade tip, and at different times: a) $t^* = 0.25$, b) $t^* = 0.50$, c) $t^* = 0.75$, and d) $t^* = 1.00$.
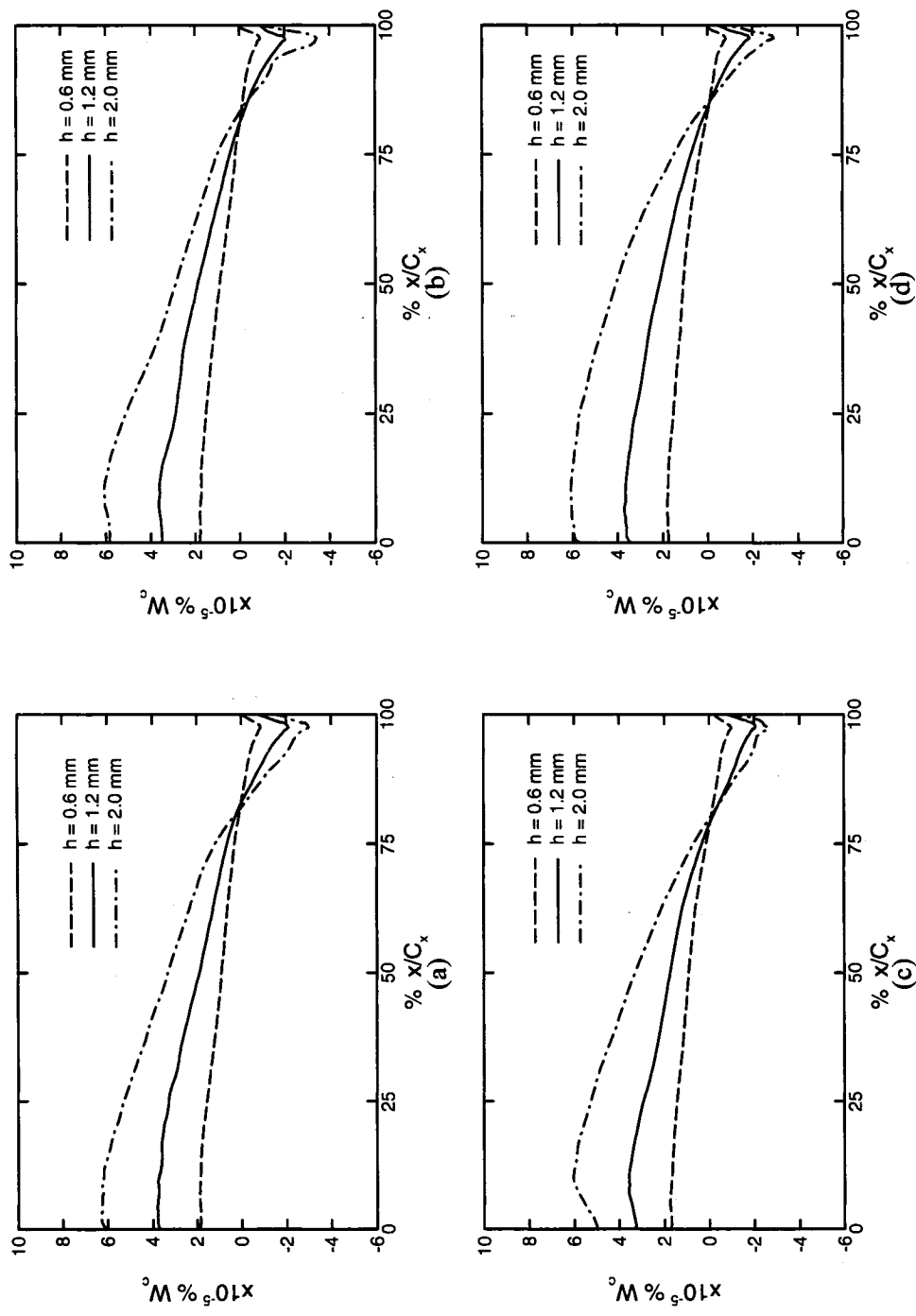
axial flow entering the tip clearance region. Figure 5.26 shows the profile of the relative

x-velocity component at $x/C_x = 48\%$ and on the camber line. At $t^* = 0.25$, $t^* = 0.75$,

and $t^* = 1.00$, it can be seen that the relative x-velocity component for Case 3 is indeed

greater than that for the baseline case. The maximum difference occurs at $t^* = 0.75$,

where the velocity at the midspan is 214 m/s for the baseline case and 256 m/s for Case 3.

Figure 5.27 shows the relative Mach number distribution along the camber line in the tip

clearance region at midspan. In general, the Mach number distributions for both cases

follow the same trend, whereby the Mach number increases to peak values at

approximately 82% x/C_x, and then abruptly decreases at the trailing edge. This is due to

the presence of the re-circulation region caused by the leakage flow interaction with the

cross-flow from the adjacent blade passage. Thus, the peak Mach number signifies the

middle of the recirculation region. Some differences were observed in Mach number

distributions at $t^* = 0.25$. From the leading edge to midchord, it can be seen that the

Mach number in Case 3 decreases while the flow increases to sonic values for the

baseline case at $t^* = 0.25$. This may be due to the flow having less random motion, and

so more fluid particles from the bulk flow will make contact with the leading edge of the

blade, thus decelerating the flow as it approaches the rotor. At $t^* = 0.75$ and $t^* = 1.00$,
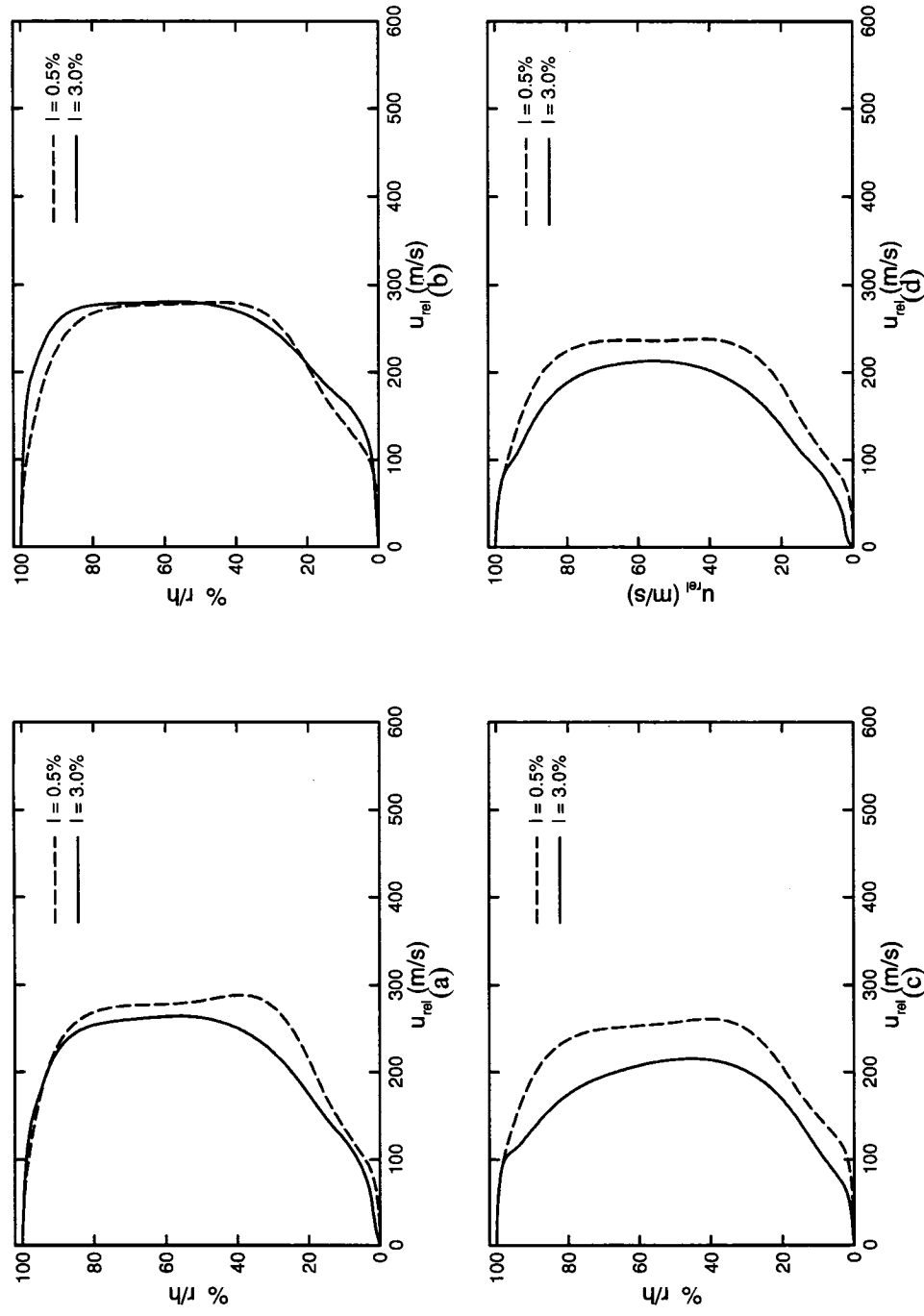
Figure 5.26 Comparison of the relative x-velocity profiles at different inlet turbulence intensities at approximately $x/C_x = 48\%$, on the camber line of the blade tip, and at times: a) $t^* = 0.25$, b) $t^* = 0.50$, c) $t^* = 0.75$, and d) $t^* = 1.00$.

142

Figure 5.27 Comparison of the variation of the relative Mach number with axial distance at inlet turbulence intensities at the midspan of the tip clearance region, on the camber line of the blade tip, and at times: a) $t^* = 0.25$, b) $t^* = 0.50$, c) $t^* = 0.75$, and d) $t^* = 1.00$.

143

the Mach number for Case 3 is greater and this is attributed to the larger axial velocity components described before.

Figure 5.28 shows the relative y-velocity profiles at different axial locations at $t^* = 1.00$. Near the leading edge, the velocity near the blade tip are nearly identical, while at higher turbulence intensity, the velocity is slightly higher. This is due to the fact that the kinetic energy is slightly higher for Case 3, since the fluid particles have more random motion. At $x/C_x = 48\%$, the velocity is nearly identical from the midspan to the shroud, while the most significant differences occur in the lower portion of the tip clearance region. At this location, the airfoil thickness is large, thus the separation bubble size is largest at this location. Since Case 3 has higher kinetic energy, the velocity inside the separation bubble will be slightly higher, as can be seen in Figure 5.28b. This trend is also observed near the trailing edge. The y-velocity is lower near the trailing edge, since the flow is moving mainly in the radial direction.

5.3.3 Effect of Inlet Stagnation Temperature

For Cases 4 and 5, the inlet stagnation temperatures are higher, and generate a smaller separation bubbles at the pressure side, as shown in Figures 5.29 and Figure 5.30. Since the stagnation temperatures are higher, the fluid contains more kinetic energy and so the velocity will be significantly larger. Since the fluid has more energy, the flow will reduce the size of the separation bubble. The added energy in the flow allows the leakage flow to also overcome the opposing cross flow at the suction side, thus there is no re-

Figure 5.28 Relative y-velocity profiles along the camber line for different turbulence

intensities at $t^* = 1.00$ at a) $x/C_x = 5\%$, b) $x/C_x = 48\%$, and c) $x/C_x = 95\%$.

Figure 5.29 Static pressure contours in the tip clearance region with $T_o = 600\,K$ at $x/C_x =$ 48%, on the camber line of the blade tip, and at different times: a) $t^* = 0.25$, b) $t^* = 0.50$, c) $t^* = 0.75$, and d) $t^* = 1.00$.

146

Figure 5.30 Static pressure contours in the tip clearance region with T_o = 800 K at x/C_x = 48%, on the camber line of the blade tip, and at different times: a) t^* = 0.25, b) t^* = 0.50, c) t^* = 0.75, and d) t^* = 1.00.

circulation at the suction side.

Figure 5.31 shows the static temperature distribution on the camber line at the midspan of the tip clearance region. At $t^* = 0.25$, the temperature decreases near the leading edge for Cases 4 and 5, while it increases for the baseline case. This is due to the fact that the flow entering the tip clearance region, near the leading edge, has a higher velocity since the kinetic energy of the fluid is higher. This can be seen in the Mach number distribution on the camber line at the midspan of the tip clearance region, as shown in Figure 5.32a. In addition, from Figure 5.31, it was observed that the temperature decreases to a minimum value near the trailing edge at approximately 82% x/C_x for both cases, and this minimum value indicates the center of the recirculation region. Thus, it was concluded that the location of the re-circulation zone is independent of the inlet stagnation temperature.

In Figure 5.32, it can be seen that near the trailing edge, the Mach number distributions follow the same trends for all cases. In addition, the magnitudes of the Mach numbers are comparable indicating once again that the development of the re-circulation zone at the trailing edge is independent of the inlet stagnation temperature. At all times, however, the Mach numbers are higher for Cases 4 and 5 from the leading edge until the beginning of the recirculation zone. This is due to the fact that the flow has higher kinetic energy in Cases 4 and 5.
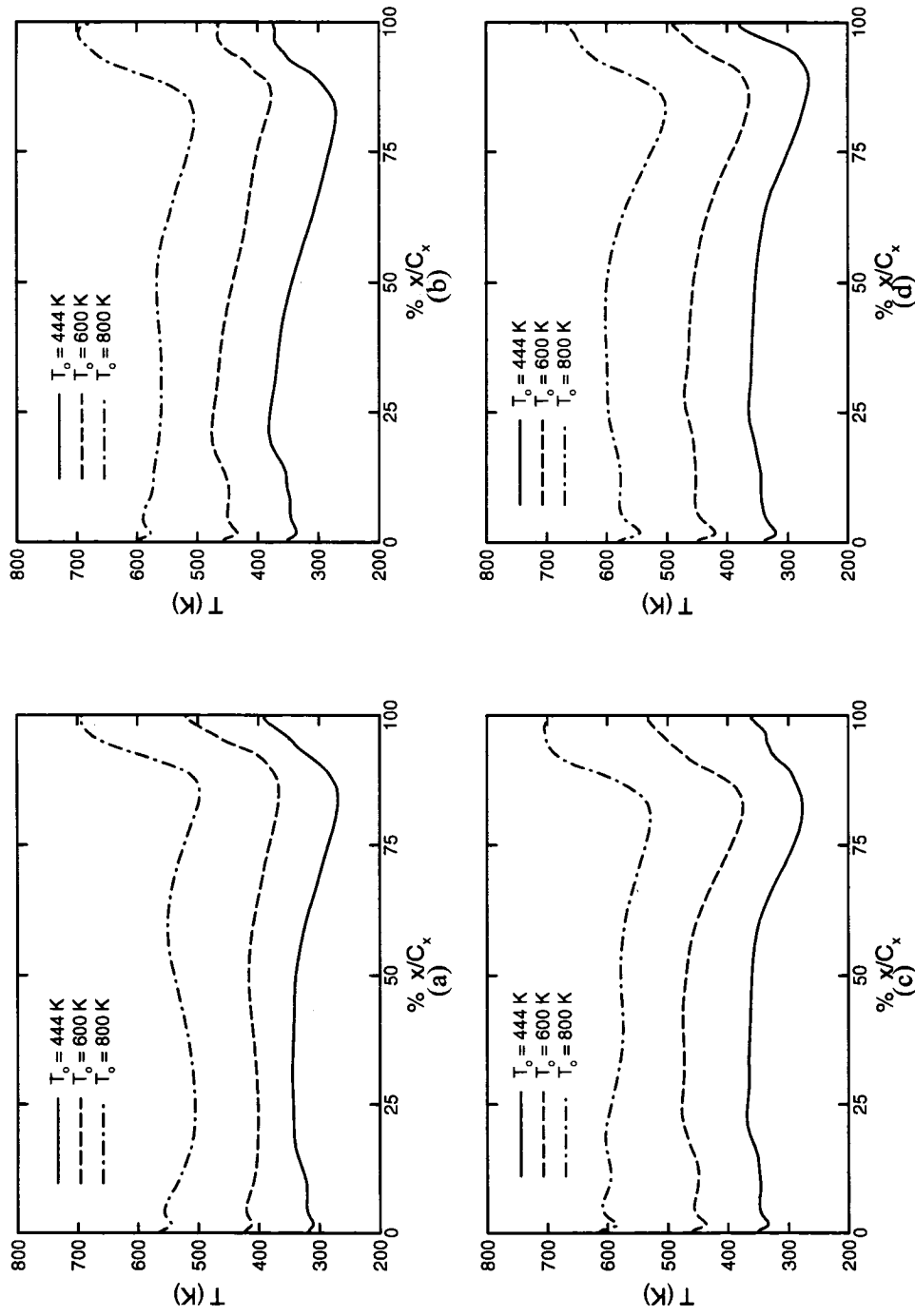
Figure 5.31 Comparison of the variation of the temperature with axial distance at different inlet stagnation temperatures at the midspan of the tip clearance region, on the camber line of the blade tip, and at times: a) $t^* = 0.25$, b) $t^* = 0.50$, c) $t^* = 0.75$, and d) $t^* = 1.00$.
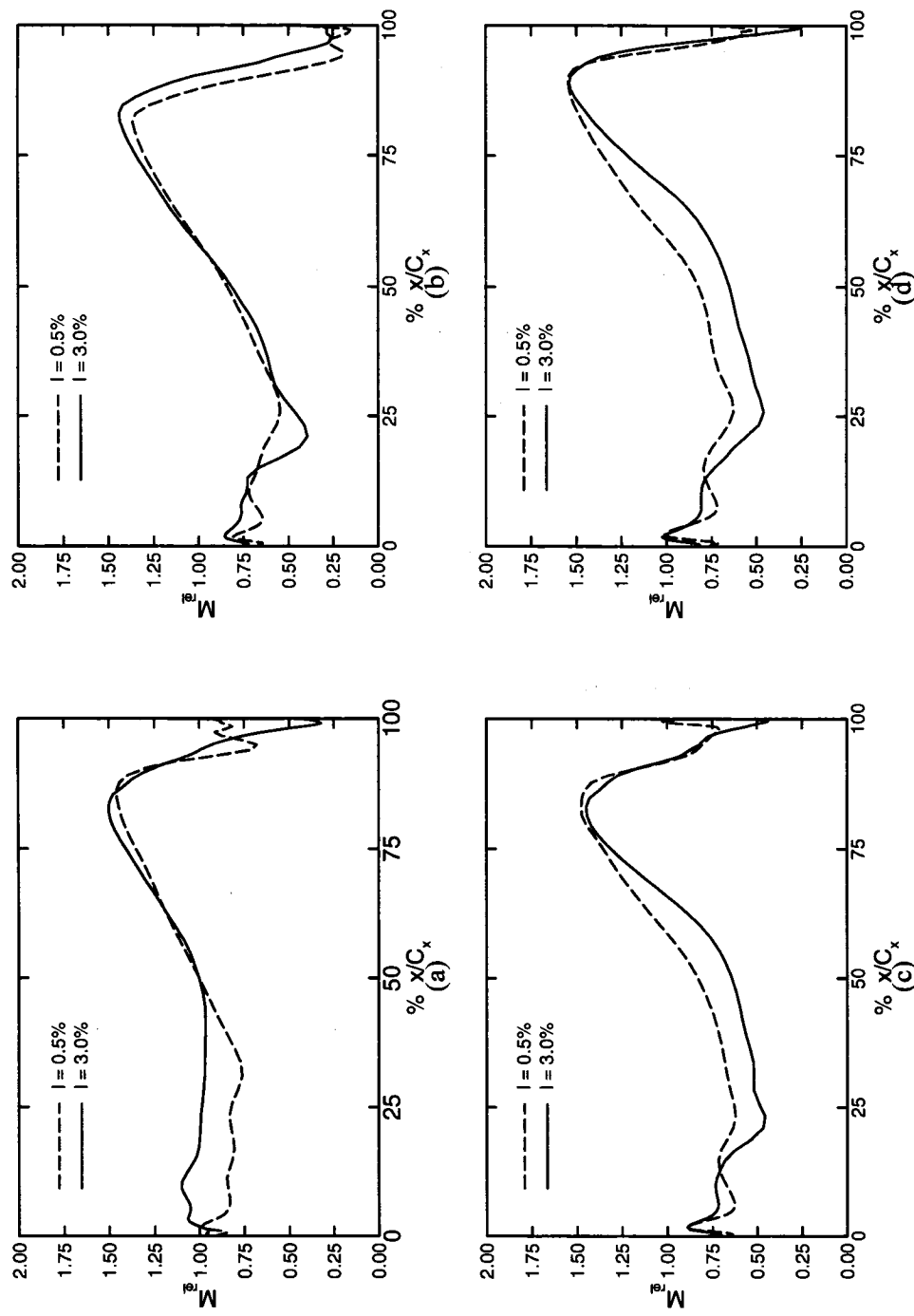
149
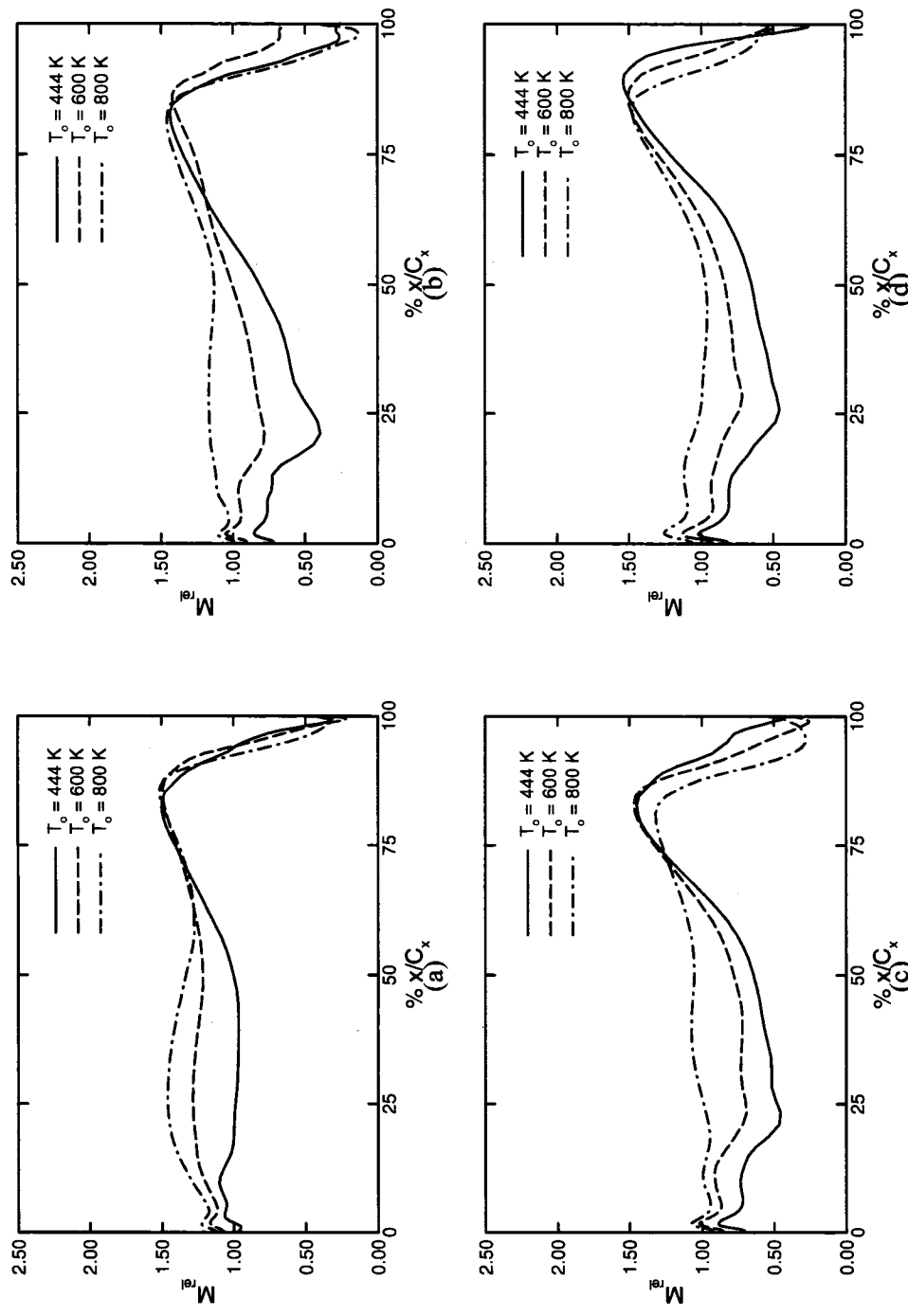
Figure 5.32 Comparison of the variation of the relative Mach number with axial distance at the midspan of the tip clearance region, at different inlet stagnation temperature, and at times: a) $t^* = 0.25$, b) $t^* = 0.50$, c) $t^* = 0.75$, and d) $t^* = 1.00$.

150

The relative y-velocity profiles at different axial positions and at $t^* = 1.00$ are compared in Figure 5.33. Near the leading edge, the velocity profiles are similar for all cases, where higher stagnation temperatures generate higher velocities since the flow has higher kinetic energy. At $x/C_x = 48\%$, in the baseline case, the opposing flow originating from the suction side is completely dominant from r/h = 93% to the shroud, which can be observed from the negative values of the y-velocity in Figure 5.32b. This is due to the larger separation bubble that is generated in the baseline case, since the stagnation temperature is lowest. The y-velocity decreases as the leakage flow negotiates around the separation bubble. Near the trailing edge, the y-velocity is nearly zero for the baseline case, since the flow is moving in the radial direction due to the larger separation bubble. Also, near the blade tip, the opposing flow is dominant since the kinetic energy of the opposing flow is also higher.

5.3.4 Effect of Rotor Angular Velocity

Figure 5.34 show the pressure contours for the lower rotor angular velocity case (Case 6), while Figure 5.35 shows those for the higher velocity case (Case 7). In Figure 5.34, the separation bubble is smaller when compared to the baseline case, and no re-circulation at the suction side was observed. Since the rotor angular velocity is lower, this means that in the rotating reference frame, the shroud wall is moving at a lower velocity. As a result, the effect of the shroud relative motion is reduced thereby generating less resistance to the leakage flow as it enters the gap at $t^* = 0.25$. Thus, the leakage flow quickly overcomes the growth of the separation bubble since there is little resistance near the
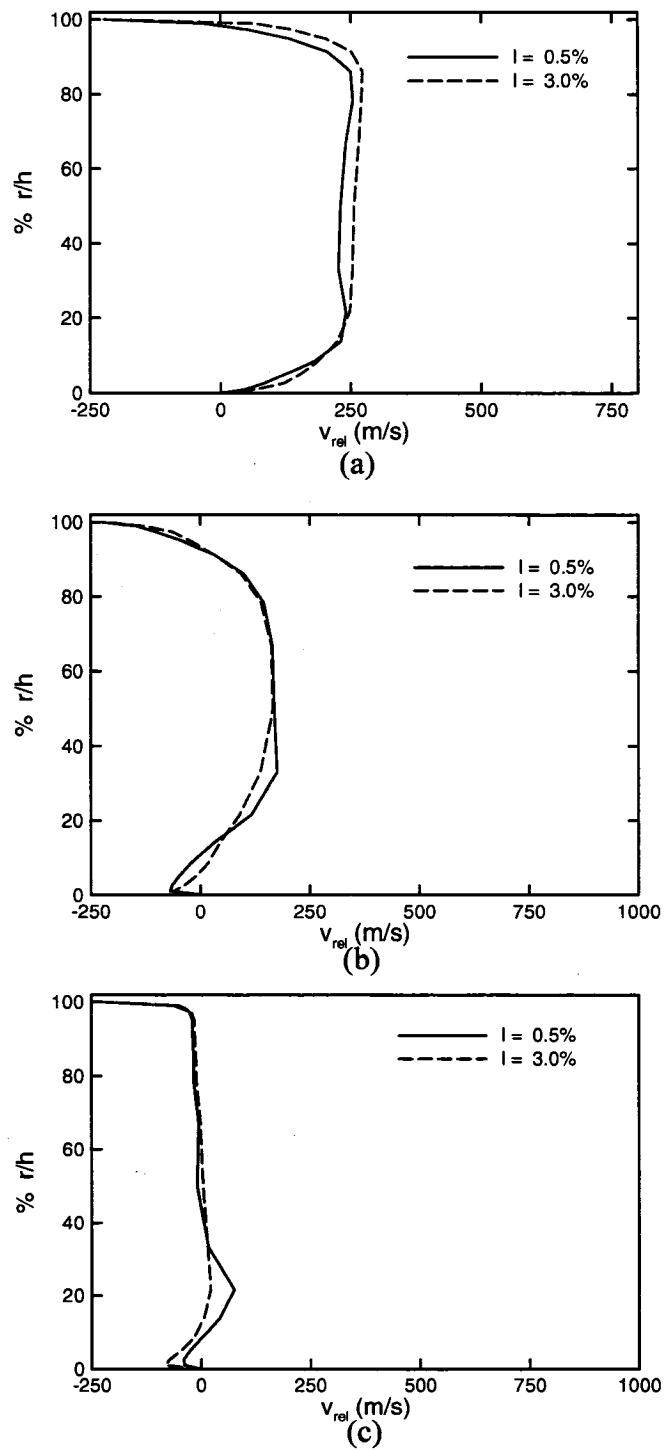
Figure 5.33 Relative y-velocity profiles along the camber line for different stagnation temperatures at $t^* = 1.00$ at a) $x/C_x = 5\%$, b) $x/C_x = 48\%$, and c) $x/C_x = 95\%$.
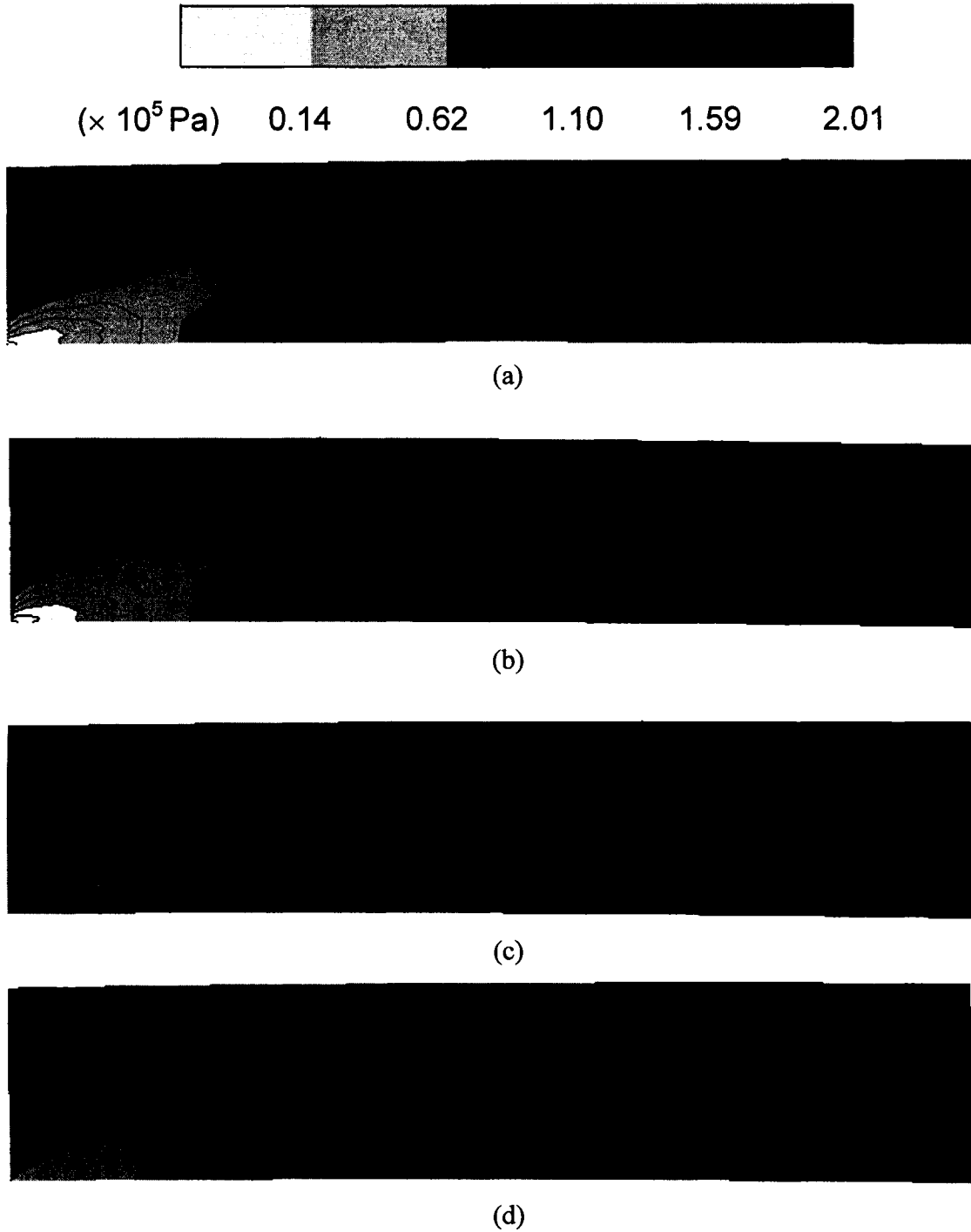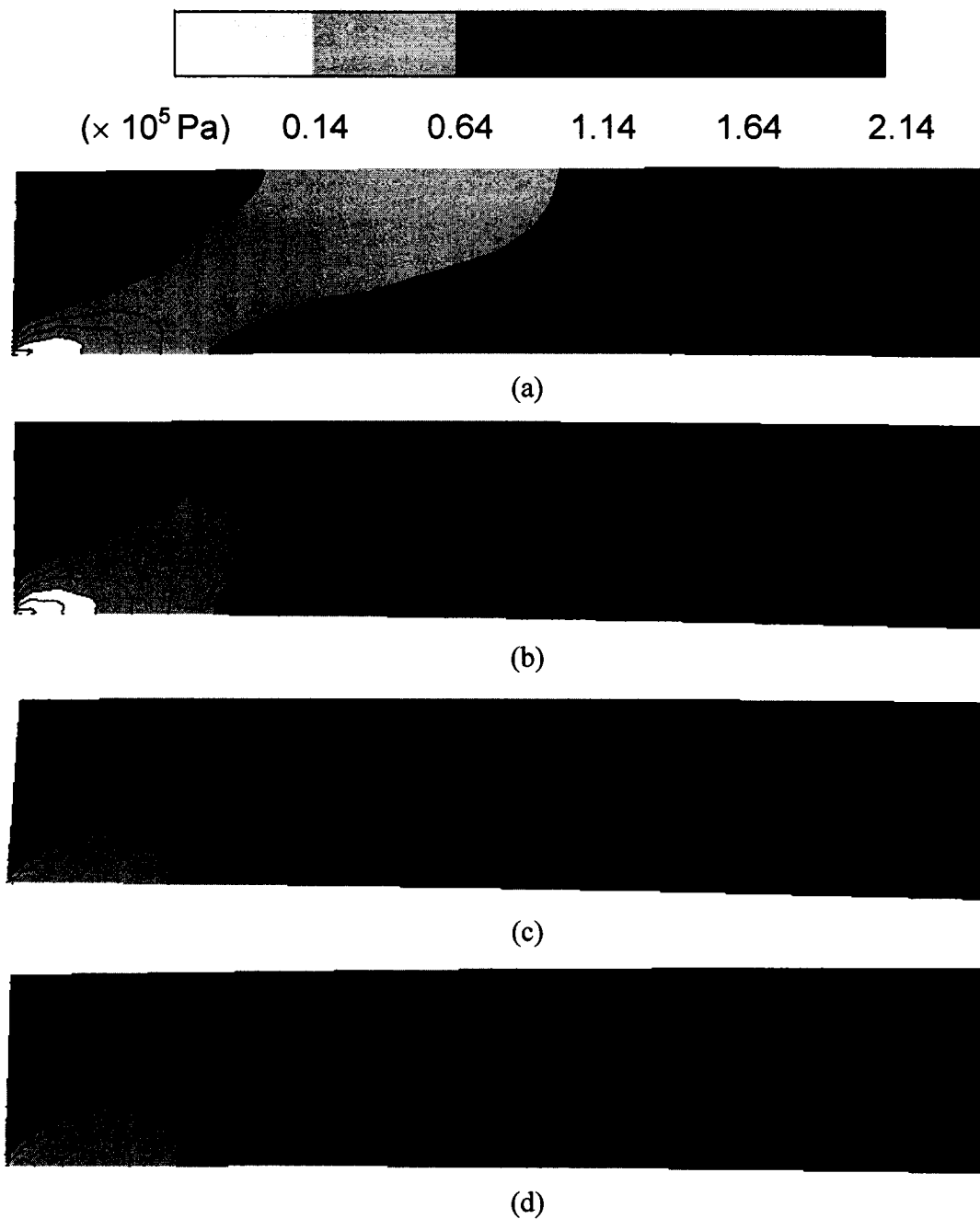
Figure 5.34 Static pressure contours in the tip clearance region with $\Omega = 7500$ rpm at $x/C_x = 48\%$, on the camber line of the blade tip, and at different times: a) $t^* = 0.25$, b) $t^* = 0.50$, c) $t^* = 0.75$, and d) $t^* = 1.00$.
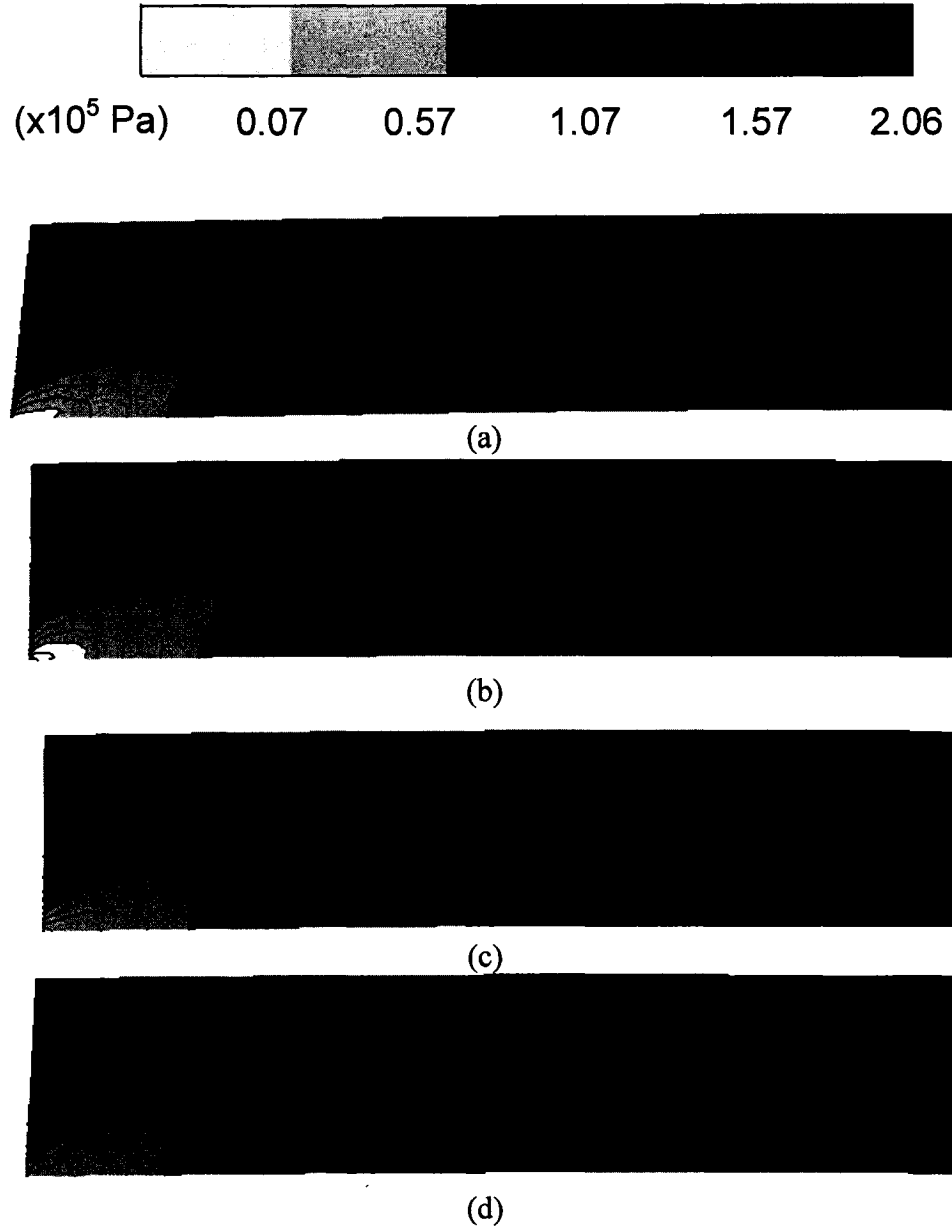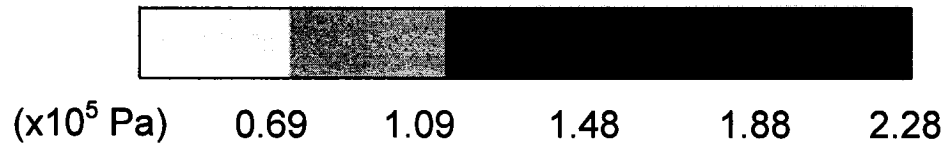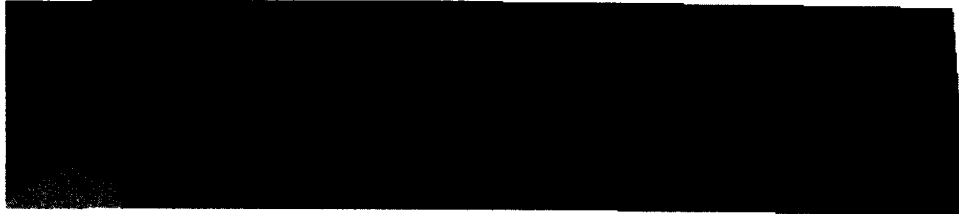
Figure 5.35 Static pressure contours in the tip clearance region with $\Omega = 11\,500$ rpm at $x/C_x = 48\%$, on the camber line of the blade tip, and at different times: a) $t^* = 0.25$, b) $t^* = 0.50$, c) $t^* = 0.75$, and d) $t^* = 1.00$.

154

shroud. In addition, the mass flow entering the tip clearance region will be greater since more flow will be allowed to enter, as shown in Figure 5.36, since the separation bubble is smaller and there is less resistance from the shroud relative motion. From Figure 5.36 it can also be seen that the re-circulation region occurs at nearly the same location at approximately $x/C_x = 82\%$.

In Figure 5.35, a large separation bubble was observed at higher rotor angular velocities, which is the result of the faster moving shroud creating more opposition for the leakage flow. Consequently, re-circulation regions at the suction side near the blade tip are observed since the leakage flow has a radially downward motion since it must negotiate over the large separation bubble. At time progresses, it was observed that the velocity decreases above the separation bubble due to the higher relative velocity of the shroud opposing the leakage flow. In addition, as expected, the mass flow is less for the higher rotor angular velocity case, as can be seen from Figure 5.36.

Figure 5.37 shows the relative y-velocity profiles at $x/C_x = 48\%$ and on the camber line in the tip clearance region for Case 6 and the baseline case. At $t^* = 0.25$, $t^* = 0.75$, and $t^* = 1.00$, the leakage flow velocity in the circumferential direction is greater for Case 6 as expected since the shroud relative motion is lower than that in the baseline case. At
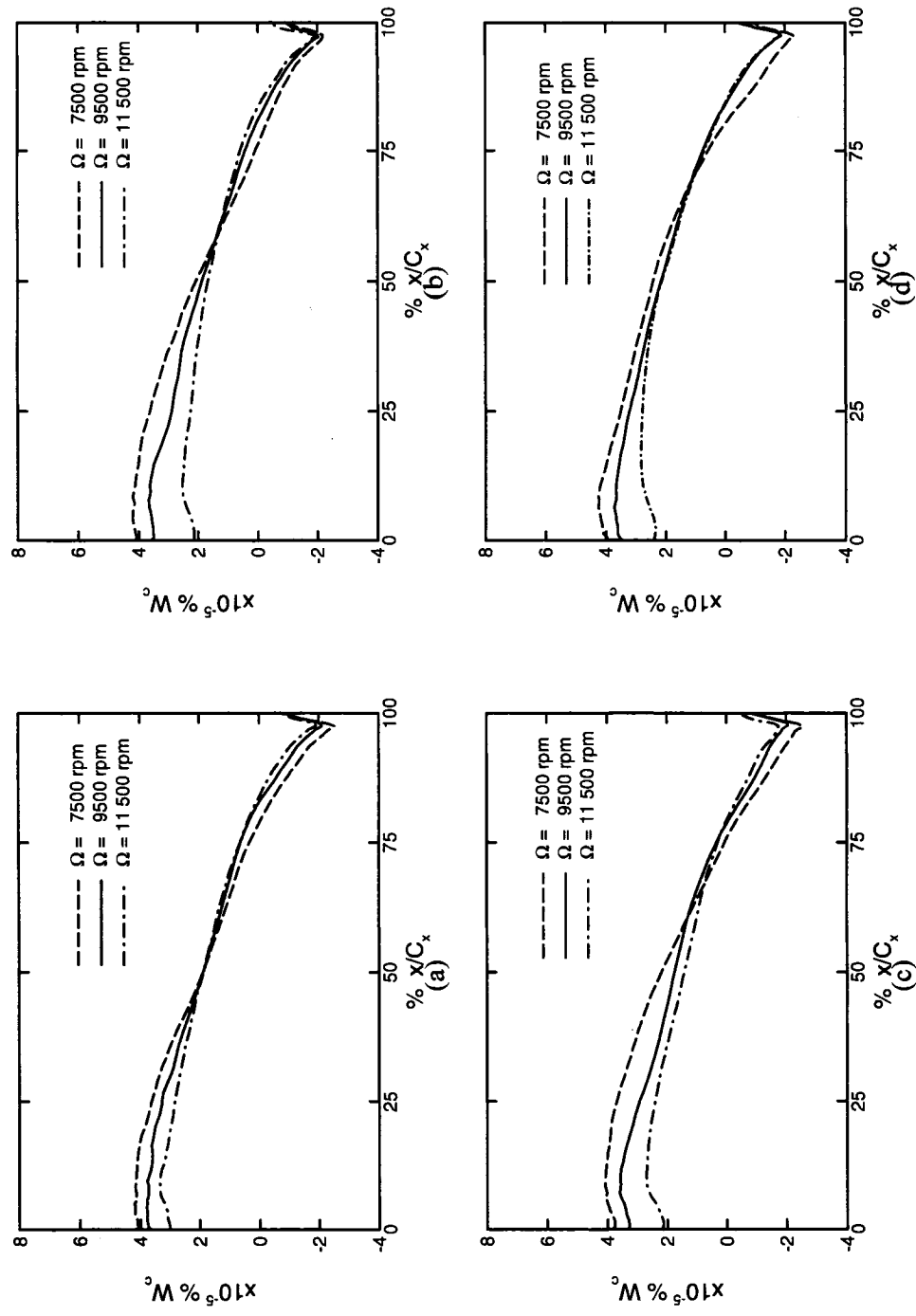
Figure 5.36 Comparison of the mass flow rate entering the pressure side of the blade at different rotor angular velocities at the midspan of the tip clearance region, and at times: a) $t^* = 0.25$, b) $t^* = 0.50$, c) $t^* = 0.75$, and d) $t^* = 1.00$.

156
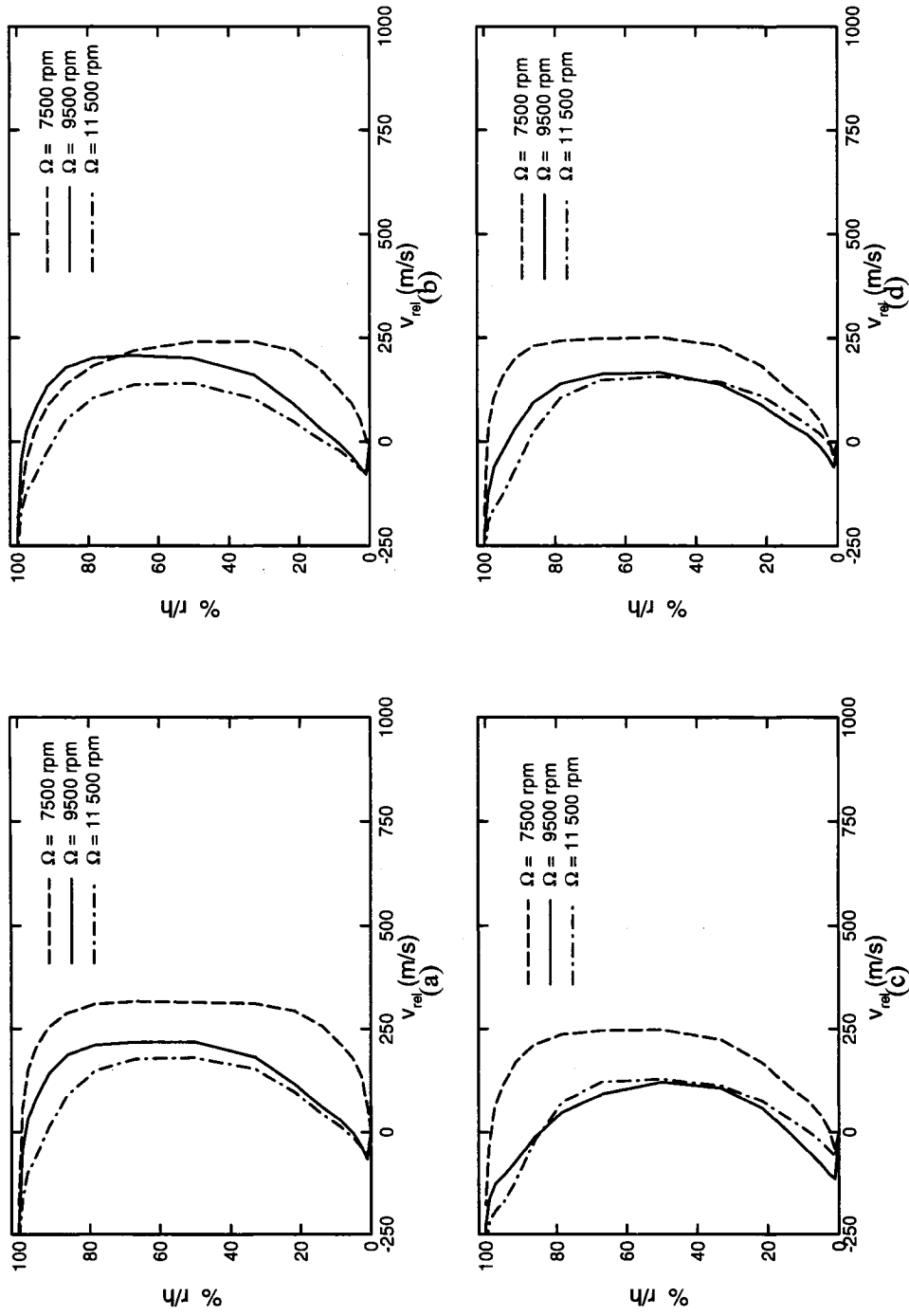
Figure 5.37 Comparison of the relative *y*-velocity profiles at different rotor angular velocities at approximately $x/C_x = 48\%$, on the camber line of the blade tip, and at times: a) $t^* = 0.25$, b) $t^* = 0.50$, c) $t^* = 0.75$, and d) $t^* = 1.00$.

157

$t^* = 0.50$, however, the leakage flow velocity near the shroud decreases due to the high-pressure region located on the suction side near the shroud, shown in Figure 5.34b. Since the leakage flow reaches the suction side sooner, the interaction with the opposing cross flow happens at an earlier time, thus generating the high-pressure region at $t^* = 0.50$ instead of $t^* = 0.75$ for the baseline case. For the higher rotor angular velocity case (Case 7), it was observed that the y-velocity profiles are nearly identical at all times. The y-velocity is lower than that of the baseline case near the shroud due to the higher relative motion of the shroud opposing the leakage flow.

Figure 5.38 shows the y-velocity profiles at different axial locations at $t^* = 1.00$. Near the leading edge, the velocity is lower due to the high velocity of the shroud, which opposes the leakage flow. At $x/C_x = 48\%$, the y-velocity has increased slightly for Case 7 in the midspan region as the leakage flow becomes dominant. For the lower rotor angular velocity case, however, the y-velocity is higher since the separation bubble is much smaller. Thus, most of the leakage flow is moving towards the suction side instead of being re-circulated inside the separation bubble. Near the trailing edge, the effect of the opposing flow is greater for the lower rotor angular velocity case since the opposing flow from the suction side is not obstructed by a large separation bubble.

5.4 Trials of Heat Transfer Calculations

Initially, attempts were made to simulate the work of Chana and Jones (2003) using the commercial CFD package called FLUENT in order to obtain heat transfer calculations on
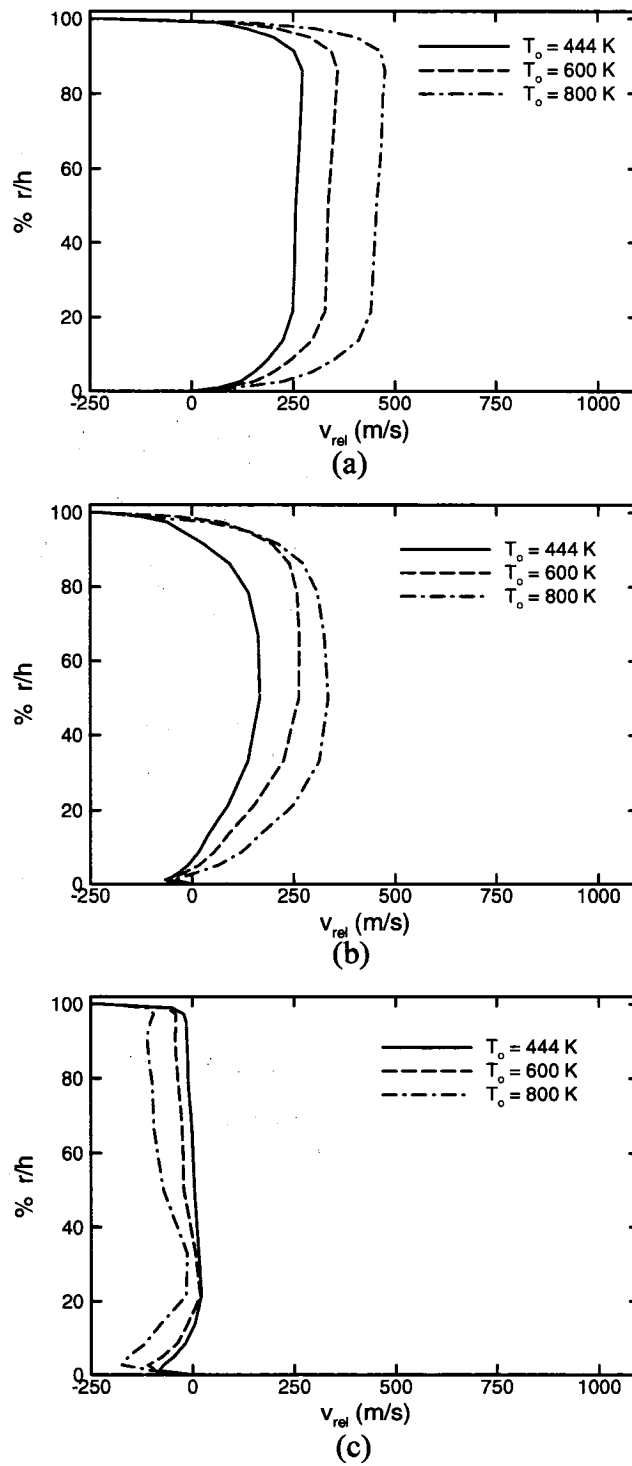
158
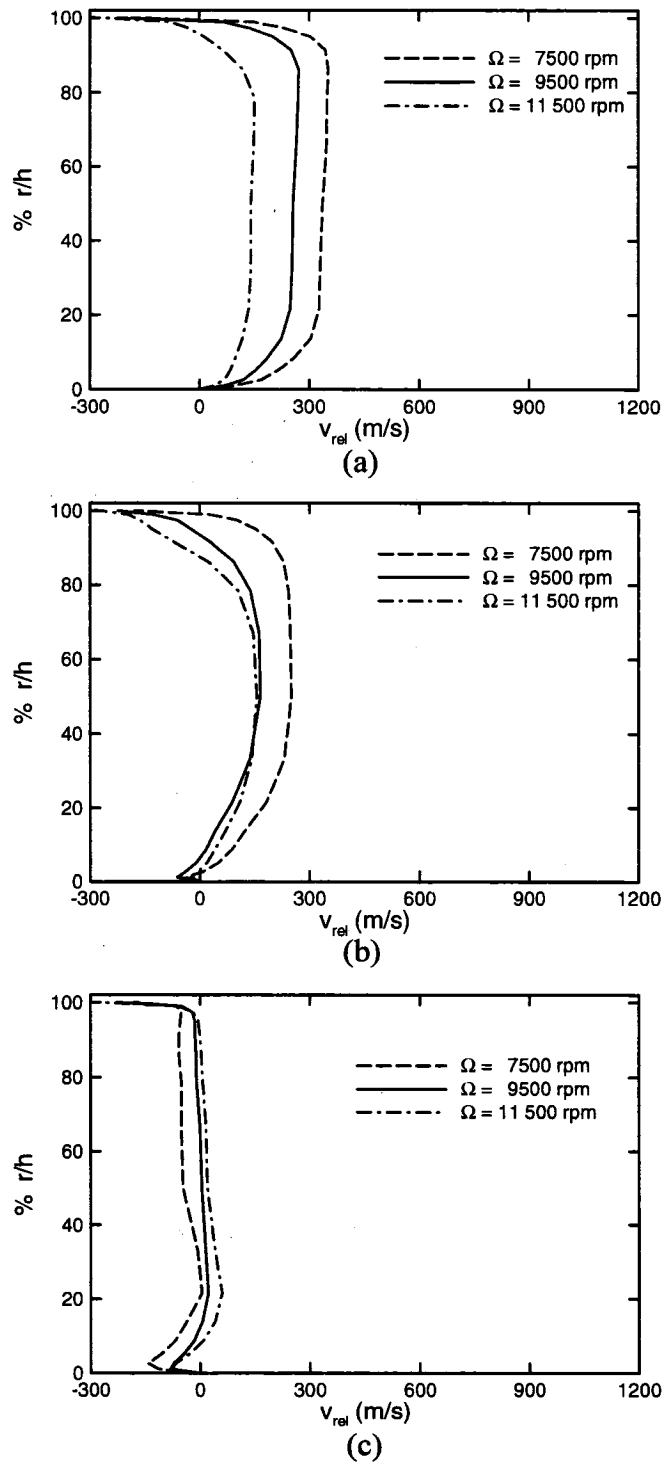
Figure 5.38 Relative y-velocity profiles along the camber line for different rotor angular velocities at $t^* = 1.00$ at a) $x/C_x = 5\%$, b) $x/C_x = 48\%$, and c) $x/C_x = 95\%$.

the shroud. Since the experimental data was obtained over a very short period of time (500 ms), constant temperature boundary conditions were assumed on all the walls of the turbine stage. A constant wall temperature of $T_w = 288\,\text{K}$ was chosen since, as reported by Chana and Jones, the inlet flow temperature was initially at this temperature before it was increased to 444 K.

Originally the grids were generated using FLUENT's prepocessor Gambit, using the Turbo Options feature included in the package. However, it proved too difficult to control the distribution of the nodes for the unstructured mesh, and the meshing procedure would often fail due to the high skewness of the elements. In addition, applying the boundary layers on the walls was nearly impossible since it was too computationally demanding for the software. If, by chance, a grid was generated, the results from the FLUENT simulations were very unrealistic with stagnation pressure increasing across the rotor to values that were 3 order of magnitudes higher than input values. As a result, Gambit was abandoned and the software called ICEMCFD was used instead for mesh generation, as described in Chapter 3.

Time-averaged results for the simulation of Chana and Jones's (2003) work were obtained by performing a mixing plane simulation as well as a frozen rotor simulation. For the mixing plane simulation, 1 vane and 1 blade were simulated, while for the frozen rotor, 1 vane and 2 blades were simulated. The mixing plane simulation took approximately five days to attain 1500 iterations using a single processor, while the

160

frozen rotor case took about seven days to reach the same number of iterations using eight processors. For the mixing plane simulation, 40 interpolation points were used in the radial direction to determine the circumferentially-averaged flow data at the mixing plane. The frozen rotor simulation allows flow data to freely cross between the NGV domain and the rotor domain through a grid interface, and was used as the initial condition for the unsteady case.

The purpose of performing the mixing plane simulation was to obtain an appropriate set up for the frozen rotor simulation. Parameters such as the Courant number and the under relaxation factors had to be adjusted in order to obtain convergence, and once appropriate values were determined, they were subsequently inputted in the frozen rotor simulation. The frozen rotor solution was then used as the initial solution for the unsteady simulations. Here, a Courant number of 1 was utilized along with five multigrid levels for faster convergence. Under relaxation factors of 0.2, 0.2, 0.8, and 0.8 were used for the turbulence kinetic energy, specific dissipation rate, turbulent viscosity, and solid respectively. In addition, second order upwind schemes were used for discretizing the flow, turbulent kinetic energy, and specific dissipation rate.

Due to the large size of the mesh consisting of 1 vane and 2 blade, approximately 3×10^6 cells, FLUENT's parallel solver was used for the unsteady cases, in which eight computer processors, all connected through a local network in the university, were used. The computers used were a combination of three Dell Precision 370 Workstations, three

Dell Precision 380 Workstations, and one PIV computer with dual processors. The fastest processors were 3.80 GHz, while the slowest were 3.60 GHz.

As mentioned before, it is important for the physical convergence parameters to attain time-periodic behavior before time-accurate results can be recorded. If the initial steady solution is not suitable, the unsteady simulations may need to run for as many as 10 or 20 vane passing periods before time-periodicity can achieved. Thus, if computer resources are limited, days or even weeks may pass before results become usable. In fact, since an implicit time discretization scheme was used in the present study, the number of inner iterations for each time step was set at 10 in order to speed up the process. However, the computational time was still very large and one unsteady case took about two weeks to attain time-periodicity, even though a parallel version of FLUENT with eight processors was used in the present study. Thus, taking into account mixing plane and frozen rotor simulations, one month was required to attain appropriate unsteady results.

In simulating Chana and Jones's (2003) study, an appropriate time step size needed to be chosen. In the rotor reference frame, the flow repeats itself according to the time required for a vane to pass at a fixed location. At the beginning, a time step size equal to $\Theta/200 = 1 \times 10^{-6}$ seconds was used. However, after two weeks of running the unsteady case (flow time $= 0.0009$ s), it was found that time periodicity was far from being attained. As a result, a new time step size of $\Theta/40 = 5.2631 \times 10^{-6}$ seconds was used in order to reach time periodicity more quickly. Figure 5.39 shows the time signal of the

mass flow rate at the rotor exit. It should be noted that FLUENT records the mass flow rate for one vane pitch, and that negative values indicate flow leaving the surface. For a time step size of 1×10^{-6} seconds, the changes of the mass flow rates with time occurs sooner than for a time step size that is five times larger, with an offset of approximately. 0.0001 s or 0.1 ms. This difference was considered acceptable, and since the time offset is also small, it was concluded that a time step size of 5.2631×10^{-6} seconds was appropriate. It can be seen that at the mass flow rates at the rotor exit still has not attained time periodic behavior after a flow time of 0.0009 seconds.

A second-order time discretization scheme was initially used in the unsteady case with $\Delta t = 5.2631 \times 10^{-6}$ seconds. However, after a week of running the unsteady case with a time step size of 5.2631×10^{-6} seconds (320 time steps), it was decided that a first-order time discretization scheme would shorten the time required to attain time periodicity. Thus, after 320 time steps, the time scheme was switched to a first-order one, as shown in Figure 5.40, and time periodicity was achieved after a flow time of 0.0025 seconds. However, there is a noticeable problem with the time periodicity of the curve, whereby the period of the signal equals 4×10^{-4} seconds, which is twice the expected value. A solution to this problem could not be found, and it was even suggested by a FLUENT support engineer that this might be due to a bug in the FLUENT software. Thus, for the present study, the use of FLUENT for heat transfer calculations was abandoned.
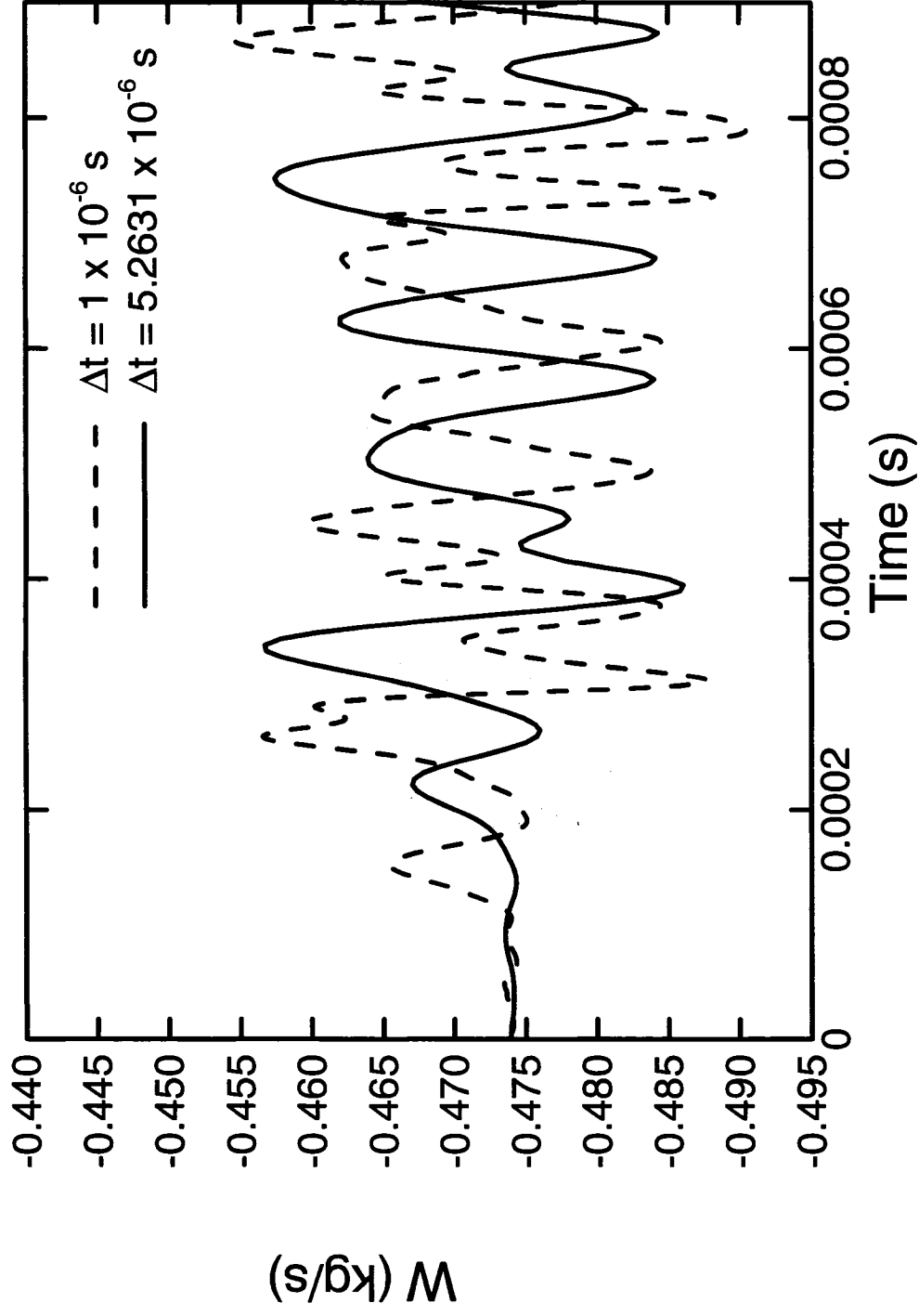
Figure 5.39 Mass flow rate time signal at the NGV exit for different time steps for the unsteady FLUENT simulation.

164
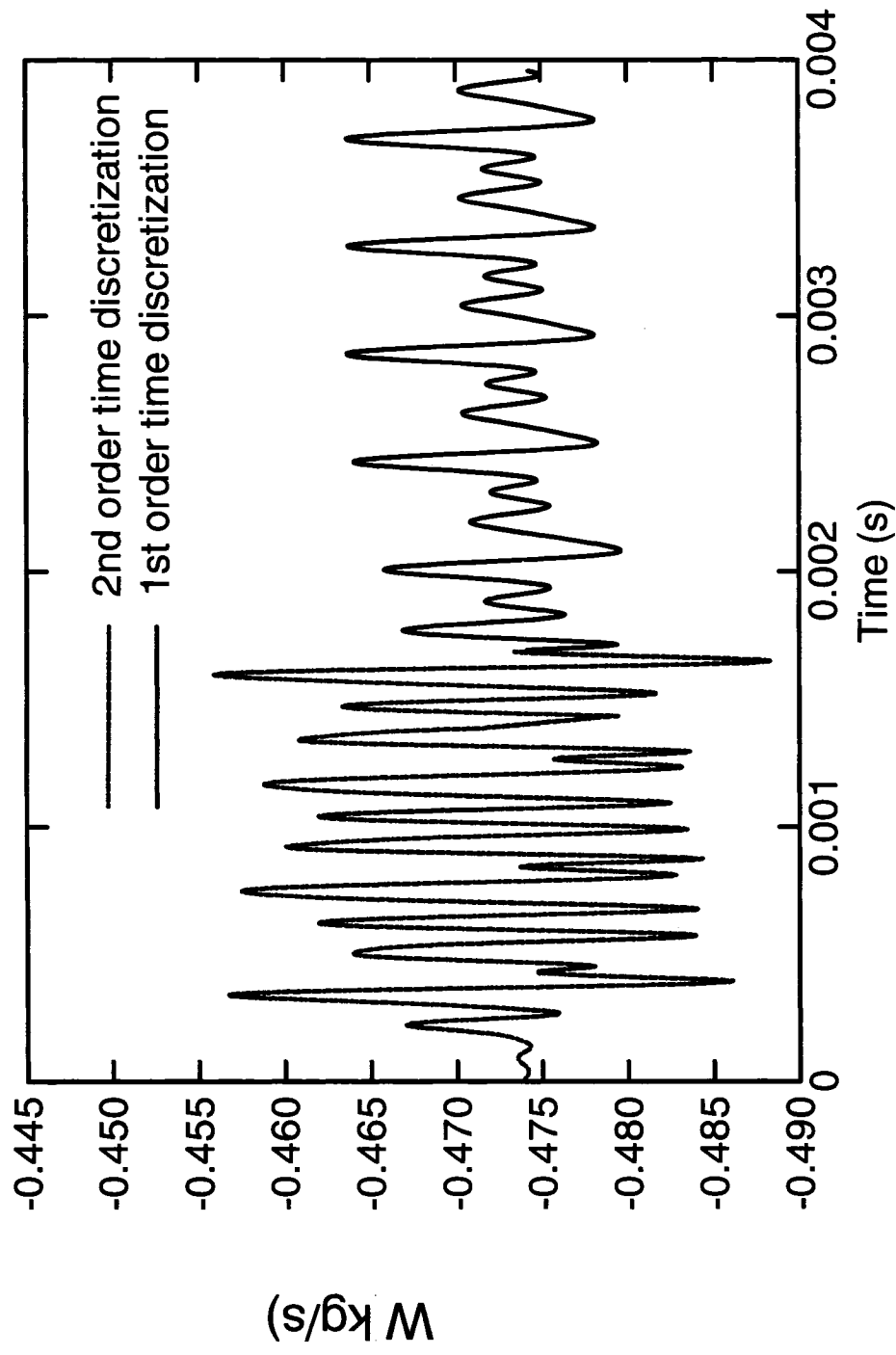
Figure 5.40 Mass flow rate time signal at the rotor exit obtained with different time discretization schemes for $\Delta t = 5.2631 \times 10^{-6}$ seconds for the FLUENT simulation.

Chapter 6

Conclusions and Future Directions

6.1 Conclusions

In the present study, time-averaged and time-accurate simulations were performed to numerically study the tip leakage flow behaviour inside an existing gas turbine facility. More particularly, the time-accurate simulations were used in a parametric investigation to study the effect of the tip clearance height, the inlet turbulence intensity, the inlet stagnation temperature, and the rotor angular velocity on the tip leakage flow. To the best of the author's knowledge, time-accurate simulations have not been performed in order to study the effects of flow parameters on the aerodynamics in the tip clearance region.

A commercial CFD software package was used in an attempt to obtain heat transfer calculations on the shroud. At first, the pre-processor that was included with the CFD package was used to generate the meshes of the computational domains. However, the grids were not adequate and yielded unrealistic results, with the stagnation pressure increasing across the rotor by three orders of magnitude. As an alternative, the software called ICEMCFD was used instead to generate meshes. Even with an improved mesh, a single time-accurate simulation required nearly a month before time-periodic behaviour was observed. In addition, the time signal of the various parameters repeated themselves after an interval twice that of the expected time period. Unfortunately, no solution was

166

found for this problem, and so an in-house industrial CFD code was used in the present study tip leakage flow aerodynamics.

Both time-averaged and time-accurate solutions were obtained for each case. Results from the time-averaged simulation of the baseline case showed leakage flow entering the tip clearance region at the pressure side of the blade, causing the development of a separation bubble at this location. The separation bubble develops due to the sudden change in curvature as the leakage flow moves upwards to negotiate the airfoil as it enters the tip clearance region. Now, near the pressure side of tip clearance region and near the blade tip on the suction side the leakage flow is dominant, while opposing flows entering through the suction side dominate near the shroud and at the suction side. This opposing flow is the combined effect of the shroud relative motion and the cross-flow originating for the adjacent blade passage on the suction side. As a result, the circumferential and radial velocity profiles show regions of zero velocity in the tip clearance region.

The static pressure and adiabatic wall temperature on the shroud were also obtained from the time-averaged solution. Another small re-circulation region was observed above the rotor passage and was attributed to the blade passage cross flow interacting with the high-pressure region found at the suction side of the blade. This high-pressure region is caused by the combined effect of the cross flow with the shroud boundary layer flow interacting with the tip leakage flow inside the tip clearance region. In addition, the adiabatic wall temperature decreases from the leading edge to the trailing edge, in the tip

clearance region, indicating the effect of the turbine expansion process and the extraction of kinetic energy from the fluid. High adiabatic wall temperatures were found at the leading edge of the blade tip, which indicates that high heat transfer rates will occur in this region. These high temperatures were attributed to the flow deceleration that occurs as the flow from the vane strikes the blade tip leading edge.

For the time-accurate solutions, it was found that the separation bubble is always present near the pressure side of the blade tip at all times, and that it size varies with flow conditions. For smaller tip clearance heights, the mass flow rate entering the tip clearance region is lower due to the smaller area, which results in a smaller separation bubble. At higher stagnation temperatures, the separation bubble size is also reduced due to the flow's higher kinetic energy, which allows the leakage flow to dominate over the bubble growth. Also, at lower angular velocities, the effect of the shroud relative motion is reduced, and so more leakage flow is allowed to enter thereby suppressing the growth of the separation bubble.

The combined effects of the opposing cross flow from the adjacent blade passage and the shroud relative motion dominates the leakage flow from the midspan to the shroud in the tip clearance. As time progresses, the opposing flow moves closer to the pressure side of the tip clearance region. Near the pressure side of the blade tip, the leakage flow dominates, and so the opposing flow changes direction generating a large re-circulation region from approximately $x/C_x = 82\%$ to the trailing edge for all cases. It was

therefore concluded that the development of this re-circulation region does not depend on flow conditions but rather the airfoil geometry, in particular where the airfoil thickness is smallest. The size of the re-circulation region does, however, vary with time as the effect of the cross-flow dissipates slightly during each vane passing period.

In addition, small re-circulation zones at the suction side and at the blade tip, similar to those found in the baseline case, were observed at smaller tip clearance heights and at lower turbulence intensities. These are due to the relative size of the separation bubble with tip clearance height. For these cases, the separation bubble occupies nearly half the tip clearance region. As a result, the leakage flow will have a higher downward radial velocity as it negotiates around the separation bubble and the opposing flow near the shroud. At the suction side, small re-circulation zones develop at the blade tip suction side as the downward moving flow interacts meets the flow passing over the suction side of the blade. It was observed that its size remains the same at all times.

6.2 Future Directions

Gas turbine designers are very interested in the heat transfer characteristics of the shroud. Results from CFD simulations are desirable since experimental methods are quite complex for data acquisition in the tip clearance region. In the present study, no heat transfer was considered in the simulations since it was not possible to obtain heat transfer calculations on the shroud using Nistar. It was also not possible to obtain reliable heat transfer results with commercial CFD software, as mentioned above. In reality, all modes

of heat transfer (i.e. conduction, convection, and radiation) are present in gas turbine engines. Therefore, CFD codes and commercial packages should be modified so that they are able to provide reliable calculations for shroud heat transfer, by implementing all the modes of heat transfer in the simulations. In the mean time, the data provided in the present study could be extended to a heat transfer study of the shroud through the use of known heat transfer correlations. The aerodynamic data provided here could be inputted into heat transfer correlations in order to obtain heat transfer coefficients inside the tip clearance region.

Nistar has shown that it is able to generate reliable results for tip leakage aerodynamics, and could be used in future studies of existing gas turbine engines. Constant pressure and temperature profiles were applied at the inlet of the nozzle guide vane, while a linear pressure profile was applied at the outlet of the computational domain. The actual pressure profiles from Chana and Jones (2003) were unknown, and so were assumed as described above. Chana and Jones (2003) do however provide data with a constant inlet temperature profile, since their test facility was not equipped with a combustor. In actual gas turbine engines, these profiles vary significantly in the radial direction due to the combustion process which occurs upstream of the nozzle guide vane. Thus, more realistic profiles, typically found in actual gas turbine engines, should be applied at the inlets and outlets of future computational domains.

Cooling flows should also be included in future simulations. Shrouds are usually cooled by the impingement of the flow, while blades are cooled externally through film cooling.

170

In the present study, cooling flows were not included since Chana and Jones (2003) did not mention their presence. These cooling flows will affect the wall temperatures of both the blade and shroud, and so will have a significant effect on the heat transfer in the tip leakage region. Nistar is able to implement cooling flows leaving the airfoil surface, but not those impinging on the shroud. Commercial software and pre-processors have the advantage of being able to model complex geometries that include impingement or film cooling holes. Thus, commercial CFD software packages could be used for modeling tip leakage flows combined with additional cooling flows, as long as they are able to obtain correct time-periodic results.

Also, commercial CFD packages are able to model complex blade tip geometries found in modern gas turbines, which are characterized by a groove that follows the blade tip camber line. Flat blade tips were used in the present study since Nistar does not typically create grooved blade tips during the mesh generation. The purpose of the groove is to reduce the amount of leakage flow, and thus the amount of heat transfer on the blade tip and on the shroud. Therefore, in order to accurately model an actual gas turbine engine, it is important to include all features of the blade tip since it will have an effect on the flow and heat transfer mechanisms in the tip clearance region.

References

Acharya, S., Yang, H., Prakash, C., and Bunker, R., "Numerical Study of Flow and Heat Transfer on a Blade Tip With Different Leakage Reduction Strategies", American Society of Mechanical Engineers, International Gas Turbine Institute, Turbo Expo (Publication) IGTI, vol. 5 A, pp. 471-480, 2003.

Allen, H. W., and Kofskey, M. G., "Visualization Study of Secondary Flows in Turbine Rotor Tip Regions", NACA Technical Note 3519, 1955.

Ameri, A. A., and Steinthorsson, E., "Analysis of Gas Turbine Rotor Blade Tip and Shroud Heat Transfer", American Society of Mechanical Engineers (Paper), 96-GT-189, 8 pages, 1996.

Ameri, A. A., Steinthorsson, E., and Rigby, D. L., "Effect of Squealer Tip on Rotor Heat Transfer and Efficiency", Journal of Turbomachinery, vol. 120, pp. 753-759, 1998.

Azad, G. S., Han, J.-C., Teng, S., and Boyle, R. J., "Heat Transfer and Pressure Distributions on a Gas Turbine Blade Tip", American Society of Mechanical Engineers (Paper), 2000-GT-194, 8 pages, 2000.

Azad, G. S., Han, J.–C., Bunker, R. S., and Lee, C. P., "Effect of Squealer Geometry

Arrangement on a Gas Turbine Blade Tip Heat Transfer", Journal of Heat Transfer, vol. 124, pp. 452-459, 2002.

Bindon, J. P., "Measurement and Formation of Tip Clearance Loss", Journal of Turbomachinery, vol. 111, pp. 257-263, 1989.

Booth, T. C., Dodge, P. R., and Hepworth, H. K., "Rotor-Tip Leakage: Part I – Basic Methodology", Journal for Engineering for Power, vol. 104, pp. 154-161, 1982.

Bunker, R. S., "A Review of Turbine Blade Tip Heat Transfer", Heat Transfer in Gas Turbine Systems, Annals of the New York Academy of Sciences, vol. 934, pp. 64-79, 2001.

Burmeister, L. C., Convective Heat Transfer, 2nd Edition, John Wiley & Sons: New York, N. Y., 1993.

Camci, C., Dey, D., and Kavurmacioglu, L., "Aerodynamics of Tip Leakage Flows Near Partial Squealer Rims in an Axial Flow Turbine Stage", Journal of Turbomachinery, vol. 127, pp. 14-24, 2005.

Chana, K. S., and Jones, T. V., "An Investigation on Turbine Tip and Shroud Heat Transfer", Journal of Turbomachinery, vol. 125, pp. 513-520, 2003.

Cho, H. H., Rhee, D. H., and Choi, J. H., "Heat/Mass Transfer Characteristics on Turbine Shroud with Blade Tip Clearance", Heat Transfer Gas Turbine Systems, Annals of the N. Y. Academy of Sciences, vol. 934, pp. 281-288, 2001.

Davis, R. L., Shang, T., Buteau, J., and Ni, R. H., "Prediction of 3-D Unsteady Flow in Multi-Stage Turbomachinery Using an Implicit Dual Time-Step Approach", AIAA Paper, No. 96-2565, 1996.

Dey, D., *Aerodynamic Tip Desensitization in Axial Flow Turbines*, Ph.D. Thesis, Pennsylvania State University, Department of Aerospace Engineering, 2001.

Dunn, M. G., Rae, W. J., and Holt, J. L., "Measurement and Analyses of Heat Flux Data in a Turbine Stage: Part I – Description of Experimental Apparatus and Data Analysis; Part II – Discussion of Results and Comparison with Predictions", Journal of Engineering for Gas Turbines and Power, vol. 106, pp. 229-240, 1984.

Dunn, M. G., "Convective Heat Transfer and Aerodynamics in Axial Flow Turbines", Journal of Turbomachinery, vol. 123, pp. 637-686, 2001.

Eckert, E. R. G., "Analogies to Heat Transfer Processes", Measurements in Heat Transfer, pp. 397-423, 1976.

FLUENT 6.2 User's Guide, Fluent Incorporated, Lebanon, NH, Chapters 9-12, 2005.

Ghaly, W., *Fluid Mechanics*, Lecture Notes, 2004.

Green, B. R., Barter, J. W., Haldeman, C. W., and Dunn, Michael, G., "Averaged and Time-Dependent Aerodynamics of a High Pressure Turbine Blade Tip Cavity and Stationary Shroud: Comparison of Computational and Experimental Results", Journal of Turbomachinery, vol. 127, pp. 736-746, 2005.

Guenette, G. R., Epstein, A. H., Norton, R. J. G., and Yuzhang, C., "Time Resolved Measurements of a Turbine Rotor Stationary Tip Casing Pressure and Heat Transfer Field", AIAA Paper, AIAA-85-1220, 9 pages, 1985.

Han, J.-C., Dutta, S., and Ekkad, S., *Gas Turbine Heat Transfer and Cooling Technology*, Taylor and Francis: New York, N. Y., 2000.

Haldeman, C. W., and Dunn, M. G., "Heat Transfer Measurements and Predictions for the Vane and Blade of a Rotating High-Pressure Turbine Stage", Journal of Turbomachinery, vol. 126, pp. 101-109, 2004.

Hassanvand, M., Tao, W. S., Tai, F. G., Qi, W. Z, "Unsteady simulation and Investigation of Tip Leakage Flow Based on Dissipation Function", Proceedings of the ASME Turbo Expo 2004, vol. 5 A, pp. 973-982, 2004.

Huang, P., Bradshaw, P., and Coakley, T., "Skin Friction and Velocity Profile Family for Compressible Turbulent Boundary Layers", AIAA Journal, vol. 31, pp. 1600-1604, 1993.

John, J. E. A., *Gas Dynamics*, 2nd Edition, Newton, MA: Allyn and Bacon, 1984.

Jayatilleke, C. L. V., "The Influence of Prandtl Number and Surface Roughness on the Resistance of the Laminar Sublayer to Momentum and Heat Transfer", Prog. Heat Mass Transfer, vol. 1, pp. 193-321, 1969.

Jin, P., and Goldstein, R. J., "Local Mass/Heat Transfer on Turbine Blade Near-Tip Surfaces", Journal of Turbomachinery, vol. 125, pp. 521-528, 2003.

Kumada, M., Iwata, S., Obata, M., and Watanable, O., "Tip Clearance Effect on Heat Transfer and Leakage Flows in the Shroud-Wall Surface", Journal of Turbomachinery, vol. 116, pp. 39-45, 1994.

Kader, B., "Temperature and Concentration Profiles in Fully Turbulent Boundary Layers", International Journal of Heat and Mass Transfer, vol. 24, pp. 1541-1544, 1981.

Kwak, J. S., and Han, J. C., "Heat Transfer Coefficient on a Gas Turbine Blade Tip and Near Tip Regions", AIAA-2002-3012, 2002.

Kwak, J. S., and Han, J.-C., "Heat Transfer Coefficients on the Squealer Tip and Near Squealer Tip Regions of a Gas Turbine Blade", Journal of Heat Transfer, vol. 125, pp. 669-677, 2003.

Kwak, J. S., Ahn, J., Han, J.-C., Lee, C. P., Bunker, R. S., Boyle, R., and Gaugler, R., "Heat Transfer Coefficients on the Squealer Tip and Near-Tip Regions of a Gas Turbine Blade with Single or Double Squealer", Journal of Turbomachinery, vol. 125, pp. 778-787, 2003.

Lampart, P., Yershov, S., Rusanov, A., and Szymaniak, M., "Tip Leakage/Main Flow Interactions in Multi-Stage HP turbines with Short-Height Blading", Proceedings of the ASME Turbo Expo 2004, vol. 5 B, pp. 1359-1367, 2004.

Launder, B. E., and Spalding, D. B., *Lectures in Mathematical Models of Turbulence*, London, England: Academic Press, 1972.

Marini, R., Senior Aerodynamicist, Pratt and Whitney Canada, personal correspondence, December 2005.

McCarter, A. A., Xiao, X., Lakshminarayana, B., "Tip Clearance Effects in a Turbine Rotor: Part II – Velocity Field and Flow Physics", Journal of Turbomachinery, vol. 123, pp. 305-313, 2001.

Menter, F.R., "Two-Equation Eddy-Viscosity Turbulence Models for Engineering Applications", AIAA Journal, vol. 32, pp.1598-1605, 1994.

Metzger, D. E., Dunn, M. G., and Hah, C., "Turbine Tip and Shroud Heat Transfer", Journal of Turbomachinery, vol. 113, pp. 502-507, 1991.

Moore, J., Moore, J. G., Henry, G. S., and Chaudhry, U., "Flow and Heat Transfer in Turbine Tip Gaps", Journal of Turbomachinery, vol. 111, pp. 301-309, 1989.

Moustapha, H., *Turbomachinery and Propulsion*, Lecture Notes, 2005.

Mumic, F., Eriksson, D., and Sunden, B., "On Prediction of Tip Leakage Flow and Heat Transfer in Gas Turbines", Proceedings of the ASME Turbo Expo 2004, vol. 5, pp. 1521-1531, 2004.

Ni, R. H., "A Multiple-Grid Scheme for Solving the Euler Equations", AIAA Journal, vol. 20, pp. 1565-1571, 1982.

Ni, R. H., and Bogoian, J. C., "Prediction of 3D-Multistage Turbine Flow Field Using a Multiple-Grid Euler Solver", AIAA Paper No. 89-0203, 1989.

Nikolos, I. K., Douvikas, D. I., and Papailiou, K. D., "Theoretical Modeling of Relative Wall Motion Effects in Tip Leakage Flow", American Society of Mechanical Engineers (Paper), 95-GT-88, 12pp, 1995.

178

Palafox, P., Oldfield, M. L. G., LaGraff, J. E., and Jones, T. V., "PIV Maps of Tip Leakage and Secondary Flow Fields on a Low Speed Turbine Blade Cascade with Moving Endwall", Proceedings of the ASME Turbo Expo 2005, vol. 6 A, pp. 465-476, 2005.

Polanka, M., D., Hoying, D. A., Meininger, M., and MacArthur, C. D., "Turbine Tip and Shroud Heat Transfer and Loading – Part A: Parameter Effects Including Reynolds Number, Pressure ratio, and Gas-to-Metal Temperature Ratio", Journal of Turbomachinery, vol. 125, pp. 97-106, 2003a.

Polanka, M. D., Clark, J. P., White, A. L., Meininger, M., and Praisner, T. J., "Turbine Tip and Shroud Heat Transfer and Loading – Part B: Comparisons Between Prediction and Experiment Including Unsteady Effects", American Society of Mechanical Engineers, International Gas Turbine Institute, Turbo Expo (Publication) IGTI, vol. 5 A, pp. 691-702, 2003b.

Radomsky, R. W., and Thole, K. A., "High Free-Stream Turbulence Effects on Endwall Heat Transfer For a Gas Turbine Stator Vane", Journal of Turbomachninery, vol. 122, pp. 699-708, 2000.

Rhee, D.-H., and Cho, H. H., "Local Heat/Mass Transfer Characteristics on a Rotating Blade with Flat Tip in a Low Speed Annular Cascade: Part 2 – Tip and Shroud",

Proceedings of the ASME Turbo Expo 2005, vol. 3 A, pp. 639-651, 2005.

Ristic, D., Lakshminarayana, B., and Chu, S., "Three-Dimensional Flow Field Downstream of an Axial Flow Turbine Rotor", AIAA paper 98-3572, presented at 34th AIAA/ASME/SAE/ASEE Joint Propulsion Conference and Exhibit, Cleveland, Ohio, 1998.

Sjolander, S. A., and Cao, D., "Measurements of the Flow in an Idealized Turbine Tip Gap", Journal of Turbomachinery, vol. 117, pp. 578-584, 1995.

Tallman, J., and Lakshminarayana, B., "Numerical Simulation of Tip Leakage Flows in Axial Flow Turbines, With Emphasis on Flow Physics: Part I – Effect of Tip Clearance Height", Journal of Turbomachinery, vol. 123, pp. 314-323, 2001a.

Tallman, J., and Lakshminarayana, B., "Numerical Simulation of Tip Leakage Flows in Axial Flow Turbines, With Emphasis on Flow Physics: Part II – Effect of Outer Casing Relative Motion", Journal of Turbomachinery, vol. 123, pp. 324-333, 2001b.

Thorpe, S. J., Yoshino, S., Ainsworth, R. W., and Harvey, N. W., "An Investigation of the Heat Transfer and Static Pressure on the Over-Tip Casing Wall of an Axial Turbine Operating at Engine Representative Flow Conditions, Part I: Time-Mean Results, Part II: Time-Resolved Results", International Journal of Heat and Fluid Flow, vol. 25, pp. 933-960, 2004.

Wadia, A. R., and Booth, T. C., "Rotor-Tip Leakage: Part II – Design Optimization Through Viscous Analysis and Experiment", Journal of Engineering for Power, vol. 104, pp. 162-169, 1982.

Wallin, S., Notes for: Applied Computational Fluid Dynamics (5C1213), http://www2.mech.kth.se/~stefanw/AppliedCFD/notes.pdf, current January 15, 2006.

White, F. M., *Viscous Fluid Flow*, 2nd Edition, New York, NY: McGraw Hill, 1991.

White, F., and Christoph, G., "A Simple New Analysis of Compressible Turbulent Skin Friction Under Arbitrary Conditions", Technical Report AFFDL-TR-70-133, February 1971.

Wilcox, D. C., *Turbulence Modeling for CFD*, La Canada, CA: DCW Industries, 1998.

Willinger, R., and Haselbacher, H., "Axial Turbine Tip-Leakage Losses at Off-Design Incidiences", Proceedings of the ASME Turbo Expo 2004, vol. 5 B, pp. 993-1002, 2004.

Wikipedia, The Free Encyclopedia, "Image: Turbine Fan Operation (lpb).png", http://en.wikipedia.org/wiki/Image:Turbofan_operation_%28lbp%29.png, (current February 14, 2006).

Wolfstein, M., "The Velocity and Temperature Distribution of One-Dimensional Flow with Turbulence Augmentation and Pressure Gradient", International Journal of Heat and Mass Transfer, vol. 12, pp. 301-318, 1969.

Xiao, X., McCarter, A. A., and Lakshminarayana, B., "Tip Clearance Effects in a Turbine Rotor: Part 1 – Pressure Field and Loss", Journal of Turbomachinery, vol. 123, pp. 296-304, 2001.

Yang, H., Acharya, S., Ekkad, S. V., Prakash, C., and Bunker, R., "Flow and Heat Transfer Predictions for a Flat-Tip Turbine Blade", American Society of Mechanical Engineers, International Gas Turbine Institute, Turbo Expo (Publication) IGTI, vol. 3 A, pp. 271-283, 2002a.

Yamamoto, A., "Endwall Flow/Loss Mechanisms in a Linear Turbine Cascade with Blade Tip Clearance", Journal of Turbomachinery, vol. 111, pp. 264-275, 1989.

Yamamoto, A., Matsunuma, T., Ikeuchi, K., and Outa, E., "Unsteady Endwall/Tip-Clearance Flows and Losses Due to Turbine Rotor-Stator Interaction", American Society of Mechanical Engineers (Paper), 94-GT-461, pp. 1-10, 1994.

Yang, H., Acharya, S., Ekkad, S. V., Prakash, C., and Bunker, R., "Numerical Simulation of Flow and Heat Transfer Past a Turbine Blade with a Squealer-Tip", American Society of Mechanical Engineers, International Gas Turbine Institute, Turbo Expo (Publication)

IGTI, vol. 3 A, pp. 295-307, 2002b.

Yaras, M., Yingkang, Z., and Sjolander, S. A., "Flow Field in the Tip gap of a Planar Cascade of Turbine Blades", Journal of Turbomachinery, vol. 111, pp. 276-283, 1989.

Appendix

A.1. Definition of Blending Functions

The blending functions are represented by F_1 and F_2. The first blending function, F_1, is defined as

$$F_1 = \tanh\left(\Phi_1^4\right), \tag{A.1}$$

where

$$\Phi_1 = \min\left[\max\left(\frac{\sqrt{k}}{0.09\omega y}, \frac{500\mu}{\rho y^2 \omega}\right), \frac{4\rho k}{\sigma_{\omega,2} D_\omega^+ y^2}\right], \tag{A.2}$$

and

$$D_\omega^+ = \max\left[2\rho \frac{1}{\sigma_{\omega,2}} \frac{1}{\omega} \frac{\partial k}{\partial x_j} \frac{\partial \omega}{\partial x_j}, 10^{-10}\right]. \tag{A.3}$$

Here, y represents the distance to the next surface, and D_ω^+ is the positive portion of the cross diffusion term defined later.

The second blending function, F_2, is given by

$$F_2 = \tanh\left(\Phi_2^4\right), \tag{A.4}$$

where

$$\Phi_2 = \max\left[2\frac{\sqrt{k}}{0.09\omega y}, \frac{500\mu}{\rho y^2 \omega}\right]. \tag{A.5}$$

The production of turbulent kinetic energy $\widetilde{G}_k$ is given by

$$\widetilde{G}_k = \min\left(G_k, 10\rho\beta^* k\omega\right) \tag{A.6}$$

184

where G_k is given by $G_k = -\rho \overline{u_i' u_j'} \dfrac{\partial u_j}{\partial x_i}$ and, β^* is given by $\beta^* = \beta_i^* \left[1 + \zeta^* F(M_t)\right]$

with $\zeta^* = 1.5$, $R_\beta = 8$, and $\beta_\infty^* = 0.09$.

The production of the specific dissipation rate is obtained from

$$G_\omega = \frac{\alpha}{\nu_t} G_k, \qquad (A.7)$$

where α is given by $\alpha = \dfrac{\alpha_\infty}{\alpha^*} \left(\dfrac{\alpha_0 + \mathrm{Re}_t / R_\omega}{1 + \mathrm{Re}_t / R_\omega} \right)$, with with $R_\omega = 2.95$, $\alpha_\infty = 0.52$, and

$\alpha_o = \dfrac{1}{9}$. However, the definition of α_∞ differs from that in the standard k-ω model. In

the SST k-ω model, this term is given by

$$\alpha_\infty = F_1 \alpha_{\infty,1} + (1 - F_1) \alpha_{\infty,2}, \qquad (A.8)$$

where

$$\alpha_{\infty,1} = \frac{\beta_{i,1}}{\beta_\infty^*} - \frac{\kappa^2}{\sigma_{\omega,1} \sqrt{\beta_\infty^*}} \qquad (A.9)$$

and

$$\alpha_{\infty,2} = \frac{\beta_{i,2}}{\beta_\infty^*} - \frac{\kappa^2}{\sigma_{\omega,2} \sqrt{\beta_\infty^*}}. \qquad (A.10)$$

Here, $\kappa = 0.41$, $\beta_{i,1} = 0.075$, and $\beta_{i,2} = 0.0828$. The blending function F_1 is given by

Equation A.1.

The definition of the dissipation of k, Y_k, is identical to that for the standard k-ω model. In the SST k-ω model, however, the term f_{β^*} is constant and equal to 1. Thus, Y_k is given by

$$Y_k = \rho \beta^* k \omega, \qquad (A.11)$$

where β^* is given by

$$\beta^* = \beta_i^* \left[1 + \zeta^* F(M_t) \right] \qquad (A.12)$$

where

$$\beta_i^* = \beta_\infty^* \left(\frac{4/15 + \left(Re_t / R_\beta \right)^4}{1 + \left(Re_t / R_\beta \right)^4} \right) \qquad (A.13)$$

with $\zeta^* = 1.5$, $R_\beta = 8$, and $\beta_\infty^* = 0.09$.

Similarly, the dissipation of ω, Y_ω, is the defined in the same manner as that for standard k-ω model, with differences in the definitions of f_β and β_i. In the SST k-ω model, f_β is a constant and is equal to 1. Thus, Y_ω becomes

$$Y_\omega = \rho \beta \omega^2, \qquad (A.14)$$

where β is given by

$$\beta = \beta_i \left[1 - \frac{\beta_i^*}{\beta_i} \zeta^* F(M_t) \right] \qquad (A.15)$$

with β_i being defined as

186

$$\beta_i = F_1\beta_{i,1} + (1 - F_1)\beta_{i,2} \qquad (A.16)$$

with $\beta_{i,1} = 0.075$ and $\beta_{i,2} = 0.0828$. The blending function F_1 is given by Equation A.4.

Also, the compressibility function, $F(M_t)$ is defined as

$$F(M_t) = \begin{cases} 0 & M_t \le M_{t0} \\ M_t^2 - M_{t0}^2 & M_t > M_{t0} \end{cases} \qquad (A.17)$$

where

$$M_t^2 \equiv \frac{2k}{c^2} \qquad (A.18)$$

with $M_{t0} = 0.25$ and c being the speed of sound given by $c = \sqrt{\gamma RT}$.

The additional term in the ω transport equation, D_ω, is called the cross-diffusion term, and is the result of blending the standard k-ε and the standard k-ω models together. The cross-diffusion term is defined as

$$D_\omega = 2(1 - F_1)\rho\sigma_{\omega,2} \frac{1}{\omega} \frac{\partial k}{\partial x_j} \frac{\partial \omega}{\partial x_j}, \qquad (A.19)$$

where F_1 is the blending function given in Equation A.1 and $\sigma_{\omega,2} = 1.168$.

It is important to note that all constants presented for the SST k-ω model are identical to those used in the standard k-ω model unless specified otherwise.